Cold Atom Interferometry

for gravity field model survey: a Mars science case

Andrea Iannone

Technische Universiteit Delft

TU Delft

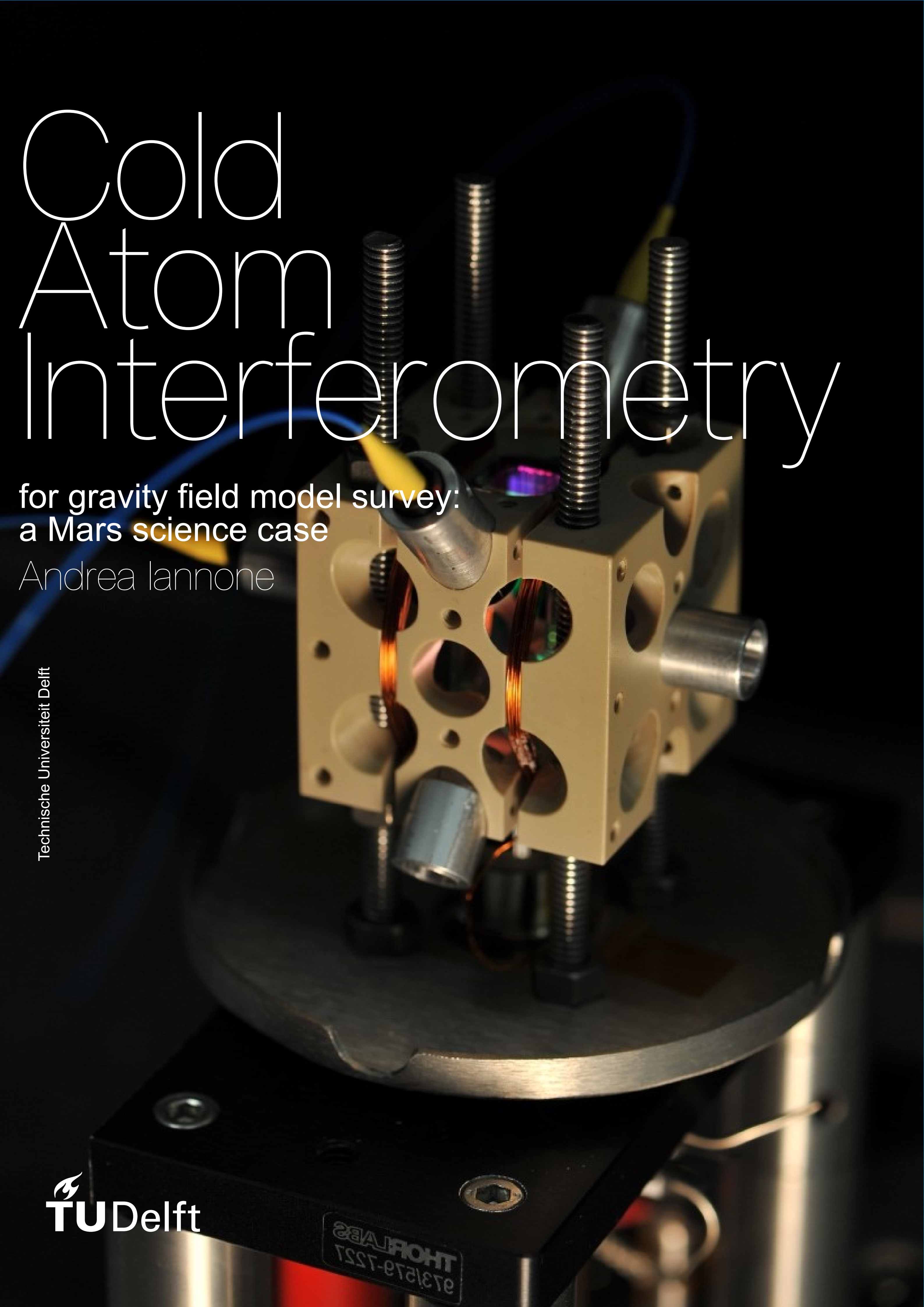

Cold Atom Interferometry

for gravity field model survey: a Mars science case

by

Andrea Iannone

to obtain the degree of Master of Science
at the Delft University of Technology,
to be defended publicly on Thursday November 24, 2022 at 2:00 PM.

Student number:	4567706	
Project duration:	April 1, 2021 – November 24, 2022	
Thesis committee:	Dr. ir. E. Moij,	TU Delft, Committee chair
	Dr. ir. D. Dirkx,	TU Delft, supervisor
	Dr. ir. C. Siemes,	TU Delft, supervisor
	Dr. S. Speretta,	TU Delft, external examiner
	Dr. O. Carraz,	RHEA for ESA, additional examiner

Cover page credits:
https://www.nist.gov/programs-projects/compact-cold-atom-instruments ,
accessed on 03/07/2020.

TU Delft

Preface

This work embodies the final seal of my student life in Delft. 6 years of a full range of emotions and exceptional experiences, that I will carry along for the rest of my life. During these years I have been dealing with a hideous disease, which has made my life very difficult, but Delft and all the people that I have met helped me push through and enjoy my life, nonetheless. Due to my condition, my achievements count twice as much to me. Therefore, there is a number of people I am deeply grateful to.

First and foremost, I would like to express my gratitude to Christian and Dominic, the best supervisors I could have ever asked for. Obviously, thank you for your extraordinary guidance, but even more for your support and understanding, especially during my hospitalizations. You have been very patient and encouraging, always available with constructive feedback. I never stopped learning a great deal from you, from both a personal and academic viewpoint. Moreover, thanks for having made my MSc thesis journey fun and amusing. I would also like to thank Olivier for having guided me through the wonders of Cold Atom Interferometry and having made the internship at ESA ESTEC an exciting stepping stone for my thesis.

I want to express my appreciation to the people who made my everyday life amazing and enjoyable: thank you, Maria, for being always by my side and acting like my bigger sister; Jonas, for making me laugh and cooking pumpkin soup for me; Miriam for being always there for me despite the distance; Eleonora, Aurora, Linda, Sara, Angela and Simona for all the good times spent together since I was a little kid; Camilla for sharing the positive and bad moments together for all these years; Fabrizia for being always close to me even though being apart.

Additionally, I would have not made it this far have I not had the support from my psychiatrist, Eleonora, who saved my life ever since I entered the clinic. The same goes for the rest of the doctors who have followed me through this complicated journey.

My deepest gratitude goes to my father, Enzo, and his wife, Elisabetta, who are patiently helping me fight this monster and become who I am today. I am also very thankful to my grandparents, Cipriano and Silvana, who have always held me up and given me the utmost love, no matter what. I thank you all for having made my studies in Delft a dream come true. Finally, I am grateful to my sisters, Ileana and Nicole, for always having my back.

Finally, I dedicate my work to you, mamma Sonia, who are my most beautiful guardian angel and who hopefully would be proud of me.

Andrea Iannone
Delft, October 2022

Abstract

As the American, European, and Chinese aerospace industries are furthering the technological readiness level of Cold Atom Interferometry (CAI) for space-borne quantum sensing of gravity, refined numerical simulations must validate their maximum capabilities for future planetary gravity reconnaissance missions. To this purpose, TU Delft, in collaboration with ESA ESTEC, has promoted a combined MSc literature review, thesis and internship project aiming to investigate the competitiveness of CAI against the backdrop of the standard gravity field model recovery techniques. The ultimate goal is to understand CAI's contribution to the resolution of the Solar System planets' gravity field models.

Thus, the work presented henceforth encompasses the essence of my MSc thesis, whose aim is to assess the potential of CAI gradiometry in enhancing the spatial and temporal resolution of the current gravity field models of Mars.

Competitive with classic inertial sensors, quantum gradiometers based on CAI are exceptional new devices, which hold the promise to measure inertial forces with an unprecedented level sensitivity (≈mE/$\sqrt{\text{Hz}}$). Mechanical effects of light pulses are exploited to spatially separate and recombine the wavepackets of cooled atoms, which, thus, interfere; by engineering 3D specific instrument configurations, from the interferometer phase shift all elements of the gravity gradient tensor could be traced back, as well as the full spacecraft angular velocity vector. This performance is enhanced by the high common-mode rejection of noise, due to the differential nature of gradiometers' measurements. Furthermore, in space, the microgravity environment prolongs the atoms' interrogation time, improving the interferometer sensitivity. On top of this, CAI's spectral behaviour features a very low flat white noise over the entire frequency range. Another advantage of these sensors is the absence of moving parts, making them drift-free and yielding no need for instrument re-calibration, fundamental for deep-space payloads.

In the current hectic scenario of exploration campaigns to Mars, the latter is deemed an excellent case study for a CAI-based gradiometry mission as refined gravity field models are required to further our understanding of the Red Planet. To this end, missions must be designed to sustain continuous monitoring of the target body and uniform global sampling, ensured by selecting an appropriate orbit (low and polar).

Both analytic and numerical covariance analysis approaches are adopted to retrieve the Spherical Harmonics (SH) coefficients' error spectra, for several CAI-based mission concepts with different orbit geometries. Compared to the latest gravity field model of Mars (MRO120F), with a maximum SH degree of 120, the treated missions can achieve degree strengths up to 390 for the static gravity field. At degree 120, the maximum SNR is about 10^3 with the most sensitive instruments. Exploiting these exceptional results, several scientific objectives can be addressed, regarding the crust and lithosphere structure, the planetary thermal evolution, the magmatism and diverse geological features, such as impact basins and quasi-circular depressions.

Contents

Nomenclature

Abbreviations

1ey 1 Terrestrial Year

1my 1 Martian Year

BEC Bose-Einstein Condensate

CAI Cold-Atom Interferometry

CAL Cold Atom Laboratory

CoM Center of Mass

COTS Commercial off-the-shelf

DFCS Drag-Free Control System

DSN Deep Space Network

EA Electrostatic Accelerometer

EGG Electrostatic Gravity Gradiometer

Estrack ESA's Tracking station network

FE Formal Errors

GG Gravity Gradient

GMM-3 Goddard Mars Model-3

GOCE Gravity Field and Steady-State Ocean Circulation Explorer

GRACE Gravity Recovery and Climate Experiment

GRAIL Gravity Recovery and Interior Laboratory

GTE Global Truncation Error

ll-SST low-to-low Satellite-to-Satellite Tracking

LNOF Local North Oriented (reference) Frame

LSA Least-Square Adjustment

LTE Local Truncation Error

MEP Mars Exploration Program

MGS Mars Global Surveyor

MOT Magneto-Optic Trap

MRO Mars Reconnaissance Orbiter

MRO120F Mars Reconnaisance Orbiter gravity field model of maximum degree 120, version F

MZ Mach-Zehnder (interferometer)

NAIF NASA's Navigation and Ancillary Information Facility

ODY Mars Odyssey

PSD Power Spectral Density

PSO Primary Science Orbit (MRO)

QCD Quasi-Circular Depression

QPN Quantum Projection Noise

RMS Root Mean Square

RS Radio Science

RSW Radial, Along-, Cross-track reference frame

SGG Satellite Gravity Gradiometry

SH Spherical Harmonics

SNR Signal-to-Noise ratio

SWAP Size, Weight And Power

TRL Technology Readiness Level

Tudat TU Delft Astrodynamics Tool

vGK van Gelderen and Koop solution

Constants

G Gravitational constant (6.674310^{-11} m^3 kg^{-1} s^{-2})

k_p Kaula scale factor (for Mars $13 \cdot 10^{-5}$)

g_0 Reference gravity (9.80665 m/s^2)

Greek symbols

ϵ Measurement error

γ Gravity potential (gravitational+centrifugal)

λ Spatial resolution

Ω Angular rate

Φ CAI phase shift

σ Formal error/ sensitivity

σ_l^2	Signal degree (l) variance
τ	Laser pulse duration
θ_M	Tilted mirror angle
v	Linear velocity

Latin symbols

$\boldsymbol{T}$	Gravitational gradient tensor
a	Linear acceleration
C_{lm}, S_{lm}	SH coefficients of (degree,order)=(l, m)
f	Observation frequency
k_{lm}	Love number of (degree,order)=(l, m)
l, m	Spherical harmonic degree, order
n	Number of photon recoil or mean motion
U	Gravitational potential
$\mathbf{k}_{\text{eff}}$	Effective wave vector
P_{lm}	Legendre function of (degree,order)=(l, m)
A	Design matrix
W	Weight matrix
x	Unknown parameters' vector
z	Observations' vector
C	Interferometer constrast or Covariance matrix
D	CAI baseline length
h	Orbital altitude
I	Satellite inclination
I_{sp}	Specific impulse
L	Maximum spherical harmonics degree
M	Planetary mass
N	Number of measurements or Normal matrix
N_1,N_2	Number of atoms in a cloud
P	Interferometer transition probability
R	Planetary radius
Rb	Rubidium
T	Interrogation time

Units

E	Eötvös $(10^{-9}$ s$^{-2})$
K	Kelvin

1 Introduction

High-resolution gravitational data is very valuable to retrieve information on the formation, the interior structure, and the geologic evolution of a planet (Mazarico et al. [18]). As a result of Newton's law of gravitation, the gravitational acceleration of a planet, as sensed from its exterior, is the reflection of the mass distribution in its interior. As a matter of fact, when gravitational data is merged with topographic data and reasonable geologic models, geophysical and dynamic parameters can be constrained such that dedicated gravity missions are not only relevant for planetary geodesy but also for astronomy, tectonics, hydrology and many other branches of space sciences. In fact, parameters such as crustal and elastic thickness, and crustal or mantle densities are key information to address questions concerning planetary differentiation, crust formation, thermal evolution, and magmatic processes (Schubert [25]).

Gravity field signatures vary in terms of spatial and temporal scales according to the phenomenon they refer to. Large spatial scale processes (tens of thousands of kilometres) involve mantle convection, ocean (if any) and atmosphere circulation, whilst resolutions of about 500 km or shorter distances are required to sense lithospheric features, ice-sheet flow, mass-balance and alike.

The most advanced techniques currently employed to recover gravitational field models of planets entail the acquisition of radio-tracking data, the measurements of range and range rate between co-orbiting spacecraft, the collection of altimeter evidence and the construction of terrain models from stereo imagery (Wieczorek [36]). In 2009, the European Space Agency (ESA) successfully launched the Gravity Field and Steady-State Ocean Circulation Explorer (GOCE) mission (Floberghagen et al. [6]), which paved the way for more accurate gravity measurements, based on sensing the gravity gradients of a planet by means of space-borne gravity gradiometers (Zheng et al. [40]).

A disruptive technology for ultra-accurate measurements of gravito-inertial forces is Cold-Atom Interferometry (CAI) (Dubetsky and Kasevich [5]). Albeit the wave nature of matter has been discovered in 1924 by de Broglie, the first experiment with light-pulse atom interferometer has been conducted in 1992 by S. Chu's group at Stanford, along with consequent advancement in laser cooling and manipulation of atoms (Yu et al. [39]). In fact, CAI-based sensors, which can be engineered as gradiometers, leverage the wave-like nature of the atoms, evident at low temperatures. As waves, they can interfere (Carraz et al. [3]), whilst the particle-like mass characteristic permits a high sensitivity to gravity (Yu et al. [39]). According to the underlying physical principles, namely the conservation of momentum between the light field and the atoms, counter-propagating laser beams interrogate the wavepackets of cooled atoms, which are spatially separated and then recombined, yielding interference. If engineering complex 3D instrument configurations, from the interferometer phase shift, all elements of the gravity gradient tensor can be traced back, via the absolute measurement of gravity changes across the gradiometer's baseline. On top of this, the differential nature of the measurements yields the common-mode rejection of spurious accelerations (Li et al. [17]).

Cold atom interferometers have already been successfully implemented as quantum inertial sensors in many industrial on-ground applications, outperforming the existing devices in terms of sensitivity (Tino and Kasevich [33]). In space, this gain is further enhanced (Carraz et al. [4]), insofar as the microgravity environment prolongs the atoms' interrogation times (Yu et al. [38]), which directly improves the instrument's sensitivity. By relying on atoms, whose inertial properties remain stable over time, the measurement sequence profits from inherent stability and repeatability (Geiger et al. [8]). Moreover, CAI-based gradiometers offer absolute measurements and are free of moving mechanical parts. Thus, they do not require instrument re-calibration, making them ideal for space applications. On top of this, these gradiometers possess a rather low ($\sim$ mE[1]) and spectrally white noise, except for very high frequencies, not relevant for gravity reconnaissance from space (Carraz et al. [4], Trimeche et al. [34]).

To investigate the potential and competitiveness of CAI for the improvement of planetary gravity field models, the Delft University of Technology and the Future Missions and Instruments division of the European Space Agency (ESA) have jointly promoted a research project, comprising a literature survey, an internship and an MSc thesis. The theory of gravity field and the state-of-the-art recovery techniques (mostly radio science and gradiometry), along with the underlying principles of CAI, have been reviewed in Iannone [12], whereby the terrestrial planets were identified as potential targets for promising CAI-based gradiometry missions. Thus, the internship assignment focused on the (semi-)analytical study of the respective test cases, as detailed in Iannone [13]. From these first-order investigations, the inadequacy of such a mission concept to Mercury arose, due to its harsh environment at very low altitudes, which are required for a dedicated gravity mission. Nevertheless, promising solutions were identified for Mars and Venus. The preliminary nature of these analyses demanded refined simulations to certify the expected enhancement of the respective gravity field models, in terms of accuracy and resolution.

Due to the limited time allocated to this assignment, the investigation is pursued for only one target body; eventually, the methodology can be adapted and generalized for the other scenario. Leveraging the considerable exploration heritage and the extensive literature available on Mars, the latter was selected. Therefore, existing mission concepts can be exploited as baselines for realistic simulations. The current gravity field models serve as a benchmark for validation and feature the results to be expectedly outperformed by CAI gradiometers.

Thus, the work presented henceforth encompasses the essence of my MSc thesis, whose aim is to assess the potential of CAI gradiometry in enhancing the spatial and temporal resolution of the current gravity field models of Mars. Thence, the definition of the research (sub-)questions hereby follows.

1.1. Research Questions

As discussed hitherto, the original aim of the overall project was to assess the potential of CAI-based gradiometry for planetary gravity field recovery. The internship assignment was functional to narrow down the list of possible targets to Venus and Mars. Within the time constraint of a thesis project, only one body can be selected as a test case. Mars was deemed the best choice in light of the consolidated industry and academic experiences that can back up and validate the research. Thus, the main question to be answered is:

”To what extent can a state-of-the-art CAI gradiometer, installed as the scientific payload of a dedicated gravity mission to Mars, enhance the mission scientific return and improve the resolution of the most recent - as of 2022 - models of the Martian (static and time-varying) gravity field?”

To respond to this question and efficiently structure the research effort, it is useful to set lower-level queries that can be addressed in itinere and that, altogether, would furnish the complete answer to the main question. Thus:

- What are the best CAI gradiometer configurations that can be realistically selected as potential payload candidates?
- Amongst the existing missions to Mars, which one is the most suitable as a baseline for a potential gradiometry mission to Mars?
- What are the possible orbit geometry modifications that would maximize the CAI mission scientific return?
- What are the spherical harmonic degree and order, as well as the spatial resolution and the accuracy of the static and time-varying gravity field model of Mars, achievable by exploiting the selected instruments and missions?
- What are the scientific objectives that can be potentially addressed by these results?

[1]The E, or E$\ddot{o}$tv$\ddot{o}$s, denotes a unit of 10^{-9} s^{-2}, an acceleration normalized by the gradiometric arm length (Li et al. [17]).

1.2. Report Outline

According to the project plan, by scrutinizing the history of Martian orbiters, a suitable mission design was chosen as a baseline. Possible variations to the orbit geometry could be comparatively examined to optimize the mission's scientific return. Thus, the most suitable CAI configurations were selected and numerical simulations were set up via the TU Delft Astrodynamics Toolbox (Tudat) to evaluate the performance of a dedicated CAI gradiometry mission. Via simulations, the scientific return of the missions was evaluated and compared to available models. All of this is discussed in the form of a journal paper (chapter 2).

The rest of the report comprises the answers to the respective research (sub-)questions in chapter 3, together with recommendations for future works. Furthermore, validation strategies are presented in Appendix A, whilst pointing and positioning errors are explored in Appendix B. Finally, the instrument dynamical range is investigated in Appendix C.

2 Journal Paper

The core methodology and results of the present thesis work has been written in the form of a journal paper, according to the standard template. It follows in this chapter.

Cold Atom Interferometry for gravity field model survey: a Mars science case

A. Iannone[1]

[1]Delft University of Technology, Kluyverweg 1, 2629HS Delft, The Netherlands

November 10, 2022

ABSTRACT

The time has matured for a communion between space science and quantum technological platforms for both academic and commercial prospects. Gradiometers based on Cold Atom Interferometry (CAI) feature a very low and spectrally white noise for all frequencies except very high ones. These are drift-free devices and do not require instrument recalibration, making them suitable for deep-space missions. This is due to the intrinsic long-term stability of atomic transitions and the absence of moving parts. On top of this, placing these instruments in microgravity naturally prolongs the free evolution time of atoms since these are in free fall together with the apparatus, enhancing the interferometer's contrast. Furthermore, leveraging the differential nature of gradiometry measurements, spurious accelerations and environmental vibrations are removed in common-mode rejection. CAI relies on the wave-like nature of the atoms, evident at low temperatures, and the conservation of momentum between the light pulses and the wavepackets of cooled atoms, which interfere. In this work, single-axis CAI-based gradiometers are exploited as scientific payload to retrieve the radial component of the gravity gradient tensor (U_{zz} in a RSW reference frame) with hitherto unachievable sensitivity ($\approx mE/\sqrt{\text{Hz}}$). In light of the current high interest towards the exploration of Mars, the Red Planet is deemed an excellent putative target of a CAI-based gradiometry mission, for refined gravity field model are quintessential to further our knowledge of the most accessible planet in the solar system. For this purpose, appropriate orbits must be opted for to guarantee continuous and homogeneous monitoring of the planetary surface, as well as global sampling.
The return of the selected missions, with several orbit geometries and CAI sensors configurations, is analysed via analytical and numerical covariance studies, which enable the investigation of the Spherical Harmonics (SH) coefficients' error spectra. The latest gravity field model of Mars, MRO120F, has a maximum SH degree of 120, with a spatial resolution of 105 and 120 km in correspondence of the south pole and north pole, respectively. The missions treated in this work can achieve degree strengths ranging between 130 up to 390 for the static gravity field survey. The most accurate spatial resolutions are below 60 km over the entire surface. For degree 120, the Signal-To-Noise ratio (SNR) is about 10^3 with the most sensitive instrument available (3.5 mE/$\sqrt{\text{Hz}}$). With these disrupting results, various scientific objectives can be pursued, regarding the planetary crust and lithosphere, its thermal evolution, the magmatism and several geological features, such as impact basins and quasi-circular depressions.

Key words. Cold Atom Interferometry, Gravity gradiometry, Mars exploration, Gravity field model, Space geodesy

e-mail: `a.iannone@tudelft.nl`

1. Introduction and Investigation Objectives

The space environment provides the means to advance the employment of disruptive quantum technological platforms for both academic and commercial purposes. In this "decade of geopotential" (Xu et al. (2007a)), due to the recent fast-paced technological progress, the hybridization of space science and quantum sensing captivates a growing attention for planetary gravity field recovery (Belenchia et al. (2022)).

There are various techniques of space-borne measurements of a planet's gravity field; three relevant ones are explored below. Historically, the most common method is Doppler tracking via NASA's Deep Space Network (DSN) and ESA's tracking station network (Estrack): it consists in measuring the change in orbiters' range (range rate) as they fly over mass anomalies, namely accumulations or deficits (as in Lemoine et al. (2001),Mazarico et al. (2014a)). The spacecraft is tracked at about 8 GHz (X-band) or ∼ 32 GHz (Ka-band) (Asmar et al. (2013)) with an average precision of 0.1 mm/s (in ideal conditions 20/30 μm/s[1]) at 60 s integration time (Li et al. (2016)).

The second method entails the observation of the change in range of two identical spacecraft following each other while flying over the planetary surface. The U.S. and German Gravity Recovery and Climate Experiment (GRACE) (Tapley et al. (2004)), and the NASA's Gravity Recovery and Interior Laboratory (GRAIL) (Asmar et al. (2013)) missions paved the way for satellite-to-satellite tracking with highly sensitive microwave sensing systems, to study the Earth and Moon gravity fields, respectively. The former produced data that helped map the static, and, most importantly, the time-varying gravity anomalies of the Earth (Li et al. (2016)). On the other hand, GRAIL's aim - with a precision of 0.05 - 0.07 μm/s resolved in 2-5 s integration time (Lemoine et al. (2014)) - was to constrain the Lunar internal structure and to map both the crust and lithosphere (Zuber et al. (2014)).

The final method implies the use of onboard gradiometers, whereby satellite gradiometry encompasses a differential observation technique in very low orbits, overcoming the problem of gravity field signatures' attenuation with altitude (Rum-

[1] Personal correspondence with Dr. ir. D. Dirkx.

mel et al. (2002)). In fact, the inertial accelerations measured by pairs of accelerometers are subtracted from each other and divided by the baseline of the gradiometric arm, yielding the survey of gravity gradients. Given the differential nature of the measurements, non-gravitational accelerations, as well as environmental vibrations, are common to both the interferometers and subtracted from each other, hence removed in common-mode rejection. Space-borne gradiometers were used for the first time on board the ESA's Gravity Field and Steady-State Ocean Circulation Explorer (GOCE), launched in 2009, to map the gravity field of the Earth with an unprecedented precision of 10^{-3} E/ $\sqrt{\text{Hz}}$[2] in the high-frequency spectrum (about 100 times more accurate than any other measurements done by accelerometers in space, such as by SuperSTAR on GRACE (Touboul (2003);Floberghagen et al. (2011))). The Electrostatic Gravity Gradiometers (EGG) were installed in a diamond configuration (Baur et al. (2007)), comprising a set of three orthogonal pairs of accelerometers mounted on an ultra-stable support structure, operating in the medium-to-short wavelength band (Floberghagen et al. (2011)). EGG measurements were supplemented by the onboard GPS receiver, exploited for high-low satellite-to-satellite tracking. 20 years of ocean radar altimetry supported the GOCE data to elaborate a mean dynamic ocean topography model, to study the terrestrial ocean circulation and transport, as well as the lithosphere and the mantle (Belenchia et al. (2022)). Notwithstanding, GOCE EGG showed significant noise at low frequencies (below 10^{-1} Hz (Carraz et al. (2015))) and suffered from difficult-to-control thermal drift. This factor limits the gravity recovery in deep space, where the instruments cannot be recalibrated (Abrykosov et al. (2019)). Cold Atom Interferometry (CAI) technique is hereby suggested, as also in Müller et al. (2020), to tackle this problem.

In this regard, the present work addresses the thrilling possibility to explore the scientific and technological development of CAI, which furnishes sensors that are amongst the most sensitive devices for gravity survey. Gravity gradiometers based on CAI technology are up to 3 orders of magnitude more sensitive to gravity gradients than the EGG at low frequencies (Carraz et al. (2015)). The working principle is based on the interference of cold atom clouds to sense their reactivity to inertial forces. Although the numerous ongoing studies of space-borne prototypes (Carraz et al. (2014);Douch et al. (2017);Trimeche et al. (2019)), these devices do not have a flight heritage in space, yet. Exploiting the coherent property of quantum matter waves, CAI gradiometers have been under development for the past 3 decades, leading to experiments that have demonstrated unambiguous space readiness (Belenchia et al. (2022)). Amongst these, there are the interference experiments on board sounding rockets (Becker et al. (2018)) and the observation of Bose–Einstein Condensation (BEC) on the International Space Station (Aveline et al. (2020)).

Cold atom interferometers have a compact setup, with no moving parts, and are exceptionally accurate instruments due to the inherent long-term stability of the atom transitions. This implies no need for instrument re-calibration, required for EGG. Using these instruments in space naturally prolongs the free evolution time of atoms since these are drag-free with respect to the apparatus, in free fall together with it (Tino et al. (2013)). In free fall, trapping the atoms, slowing them down and keeping them in coherent states is naturally easier. Another advantage of CAI in microgravity is that multi-component gradient measurements can be performed, whilst on Earth only the vertical component can be sensed (Yu et al. (2002)). Moreover, the noise Power Spectral Density (PSD) is flat for all frequency measurements, which are performed with very good repeatability (Xu et al. (2007b)).

In the frame of this work, CAI-based gradiometers are explored as the scientific payload of a set of missions to Mars, aimed at surveying the planet's gravity field in order to improve the accuracy of the current models thereof. Humanity has always been captivated by the "*blood-like hue*[3]" of Mars. The latter has been under the spotlight ever since the successful launch of the first Mars probe, Mariner 4 (Branigan (1965)), in 1964. The main reason is that Mars embodies the most accessible planet in the solar system and presents Earth-like features, being a terrestrial planet. It possesses a thin atmosphere, a varying climate, a complex geology and water. Over the years, a considerable amount of missions have been launched to improve our understanding of the planet's structure and environment, exploring the existence of present or past habitable conditions (Genova (2020)). Several rovers, landers and orbiters permitted to further our knowledge of Mars, spanning from its deep interior up to the atmosphere.

In the current fast-paced exploration environment of Mars, a CAI-based gradiometry mission would allow to address various scientific objectives. To this end, gravity data must be paired with gravity-from-topography studies, as suggested by Antonio Genova in Genova (2020). The latest topography map has a resolution of 1x2 km^2 at the equator. On the other hand, over 16 years of gravity missions to Mars led to gravity maps with a maximum spatial resolution of 105 and 120 km at the southern and northern poles, respectively. Therefore, the gravity models are limiting and improved ones are necessary.

The latest and most accurate gravity field solution is labeled MRO120F[4] (Konopliv et al. (2020)), retrieved by analysing over 16-year (~1.5 solar cycles) of tracking data from three NASA's spacecraft, jointly: Mars Global Surveyor (MGS), Mars Odyssey (ODY), and Mars Reconnaissance Orbiter (MRO) (Genova et al. (2016)). The gravity field comprises the full spherical harmonics up to degree and order 120 and describes an unprecedented correlation between gravity and topography harmonic expansions at high degrees (Konopliv et al. (2016);Tenzer et al. (2015)). Such high-resolution measurements led to a detailed global map of the Martian crustal thickness, under the assumption of a solid planet (Konopliv et al. (2011)). The radio science data covering over a solar cycle permitted to monitor the seasonal variations of the Martian gravity field, especially due to the CO_2 cycle, and to analyse the inter-annual mass exchange between the polar caps (Genova et al. (2015)). Time-variable solutions for the zonal harmonics, at annual, semi-annual and tri-annual frequencies, have also been estimated (Genova et al. (2016)).

A dedicated gravity gradiometry mission to Mars would enhance our knowledge of the planet's crust and lithosphere (Neumann et al. (2004);Belleguic et al. (2005);Goossens et al. (2017)), the thermal evolution (from the thickness and density gradients), the magmatism phenomena (Goossens et al. (2017)), the nature of impact basins and craters, polar volatiles and planetary deformation (Frey et al. (2002)). Leveraging these premises, gradiometry (and altimetry) data can be exploited to answer the following scientific questions:

[2] 1 E (Eötvös) equals 10^{-9} s^{-2}, a unit of acceleration divided by distance (baseline) used with reference to gravity gradients.

[3] From https://www.nationalgeographic.com/science/article/mars-exploration-article, accessed on 13/03/2021.

[4] All the data regarding the MRO120F is available in `https://pds-geosciences.wustl.edu/`(accessed on 28/07/2022).

- What are the crustal density and thickness of Mars on a regional and local scale (Neumann et al. (2004);Goossens et al. (2017))?
- How does the crustal structure correlate with the hemispheric dichotomy (southern highlands, northern lowlands)(Genova (2020);Frey et al. (2002);Smith et al. (2001))?
- What is the local sub-crustal stress of Mars? What are the major stress field features? What is the geological origin of these (Eshagh and Tenzer (2015))?
- What is the crustal porosity? Does it play a role in the determination of the crustal density (Goossens et al. (2017))?
- What are the mass excesses layered in proximity of the major basins and in the polar caps (Smith et al. (2001))?
- How does the elastic thickness flex under the studied loads (Smith et al. (2001))?

The present paper is organized as follows. In section 2, the CAI working principle is discussed together with the instrument sensitivity. Then, four configurations for this work are individuated. On the other hand, the selection of mission orbits is provided in section 3, whereby, firstly, a baseline mission is chosen and, subsequently, the dynamical model for other orbital geometries is outlined. For the selected orbits, some aspects of the mission design are also discussed. In section 4, the methodology sported for this assignment is presented, comprising analytical and numerical covariance analyses. The numerical simulations performed in this work have been carried out on the Tudat (TU Delft Astrodynamics Toolbox[5]) platform, developed by the Astrodynamics and Space mission department of TU Delft. The resulting Spherical Harmonics (SH) error spectra are investigated and the gravity field determination quality is compared against the current Doppler-based solutions. The obtained results are presented and discussed in section 5. Finally, the main conclusions are drawn in section 6.

2. Cold Atom Interferometry

Even though the dual nature of atoms has been known for almost a century, matter waves have not been exploited until proper techniques to cool, trap and manipulate atom ensembles and beams were developed, which have now led to the advancements of the (light-pulse) Atom Interferometry (AI) field. In fact, the wave-like nature of the atoms allows the correspondent matter waves to interfere (Carraz et al. (2014)), whilst the particle-like mass characteristic permits a high sensitivity to gravity (Yu et al. (2002)).

In this section, the working principle of CAI is described, together with the basics of quantum measurement of the gravity-gradient tensor's components. Finally, the devices' sensitivity is discussed, followed by the instrument selection for the present work.

2.1. Working Principle

Substantially, the Cold Atom Interferometry (CAI) works on the principle that, when a resonant travelling wave excites a set of atoms in free fall, momentum is conserved between the light field and the atoms: thus, these receive a momentum impulse and coherent superpositions of their states with different momenta are created (Peters et al. (2003)). As originally predicted by Einstein, at a temperature such that the de Broglie wavelength is similar to the mean distance between particles, the atomic macroscopic population is altogether in the lowest energy quantum mechanical state and behaves as one wavefunction (Anderson et al. (1995)). In these conditions, the dual nature of atoms is macroscopically evident, making wavefunction interference, thence interferometry, possible. At even lower temperatures, the atom ensemble manifests evidence of Bose-Einstein Condensation (BEC). Condensates have a small extent and slow expansion which curtail wave-front distortions and curvature, a major source of systematic errors (Abend (2017)). A BEC is, thus, required for enhanced instrument sensitivity, yet the physics package complexity augments significantly. As a matter of fact, a CAI instrument comprises a physics package, a laser system and an electronics unit, whose interfaces are described in Figure 1.

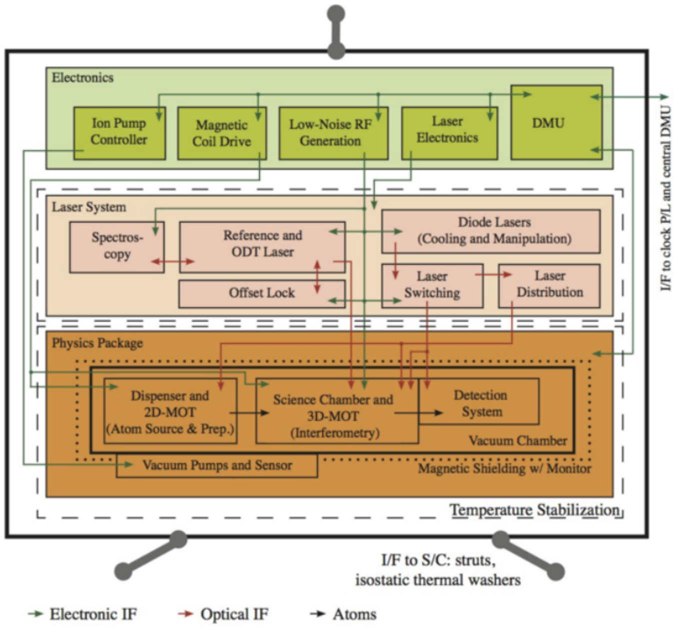

Fig. 1. Block diagram of a space-borne cold atom interferometer (Tino et al. (2013)), with the interfaces of the physics package (orange), electronics unit (green) and laser system (light pink).

In detail, there are different processes for the atoms preparation: as suggested in Geiger et al. (2020), the ensemble of atoms involved is primarily extracted from a low-pressure background vapour reservoir or a 2D Magneto-Optic Trap (MOT) flux and subsequently loaded in a 3D Magneto-Optic Trap. Here, 10^8 atoms can be collected in about 100 ms and pre-cooled with several laser-cooling mechanisms to temperatures between μK to nK.

In analogy with optical interferometry, successive coherent atomic beam-splitting and -recombining processes separated by a certain interrogation time lead to free-fall paths interference (Stern et al. (2009)). This work focuses on the light-pulse interferometry with cold-atoms Raman transitions. This specific type is chosen over many others, such as Ramsey-Bordé (Cadoret et al. (2009)), because Raman transitions allow large velocity transfer to the atoms, of the order of cm/s, which ensures high interferometer sensitivity. It also permits to properly control the diffraction process, required for accuracy; at the same time, a fair level of system complexity is kept.

[5] Documentation available on https://tudat-space.readthedocs.io

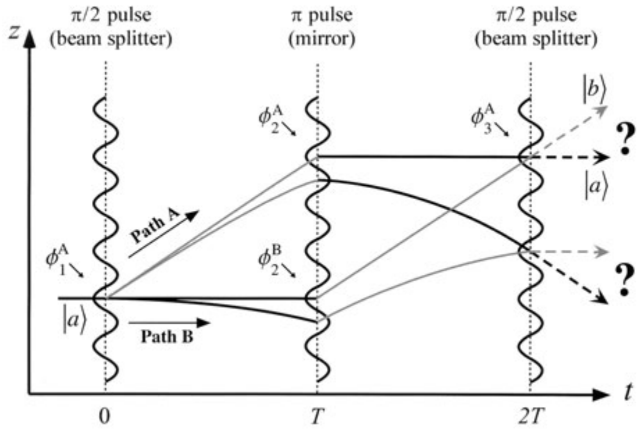

Fig. 2. Basic March-Zehnder type atom interferometer (Peters et al. (2003)). The lines in the scheme represent the classical-mechanics trajectories starting from a space-time point with a specific wave packet. The curved lines show the effect of experienced acceleration: without it, the straight lines indicate no relative phase shift results (Yu et al. (2002)). Mind that the pulses are usually parallel to the direction of the acceleration.

In the simplest case, depicted in Figure 2, the atom interferometry procedure can be modelled onto the concept of an optical three-grating - splitter, mirror and recombiner - Mach-Zehnder (MZ) interferometer (more on the optical counterpart in Almeida et al. (2019)). The entire process can be summarized as the closed loop of a laser-cooled atoms sample undergoing a sequence of three two-photon stimulated Raman transitions. These have duration, respectively, of τ, 2τ, τ. For $\tau = \pi/2$, the three Raman pulses have a sequence of $\pi/2, \pi, \pi/2$. The first one splits the incoming sample of atoms with state $|a\rangle$, creating a superposition of atoms in two hyperfine ground states $|a_{\text{path A}}\rangle$ and $|a_{\text{path B}}\rangle$. Only the excited population experiences a photon recoil kick and travels at a different velocity along Path A in Figure 2 (Gauguet et al. (2008)). The π Raman pulse, as a mirror, redirects the two populations which eventually interfere with the last $\pi/2$ pulse, a splitter with the opposite functionality: it re-directs (a portion of) the atoms in each cloud from one hyperfine state to the other, finally closing the interferometer loop (Yu et al. (2002)). During the entire process, an ultra-stable oscillator furnishes a reference for the laser beams and a mirror that reflects them serves as the reference frame. Once the clouds are recombined at the interferometer output ports, the respective interferometry fringes are measured by monitoring the population of the two hyperfine states (N1 and N2 respectively) in the recombined atom ensemble: their fluorescence, depending on the number of atoms in each cloud, is captured (Figure 3 (a) and (b) for top and bottom output ports, respectively) in a dedicated detection zone with a camera or photomultiplier tube (Sansò and Migliaccio (2020); Geiger et al. (2020)). The (probability of the) total number of atoms in either of the states can be retrieved, as shown in Figure 3 (c) and (d).

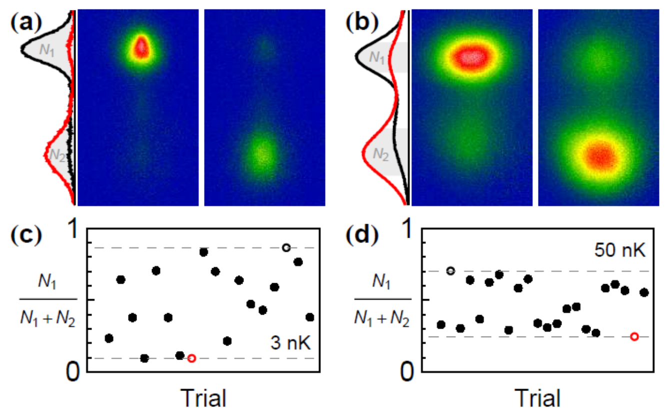

Fig. 3. Images captured at the interferometer output ports for two settings: temperature of 3 nK (left), resulting in C=80%, and 50 nK (right), with C=48 %. Each pair of images (a) and (b), with respective top and bottom fringes, is represented by open circles in the associated phase-scan scatter plots for different trials, (c) and (d). The black and red solid lines represent the atomic density integrated horizontally for the two images in (a) and (b). Taken from (Dickerson et al. (2013)).

With this observation, given the superposition principle, the interferometer transition probability P can be inferred. It depends on the interferometer phase Φ with which it oscillates sinusoidally:

$$P(\Phi) = \frac{N_1}{N_1 + N_2} = P_0[1 + C\cos(\Phi)]. \tag{1}$$

In the equation above, P_0 indicates the mean - usually 0.5 - and C is the interferometric contrast. The latter is a measure of the fraction of the total number of atoms that are manipulated by the beam splitter (Abend (2017)) and that contribute visibly to the interferometric signal (fringes). Ideally, in absence of external accelerations, as indicated by the straight lines in Figure 2, the intrinsic symmetry yields a null interferometer phase. In presence of external accelerations, the atoms fall repeatedly, as shown by the curved lines in the aforementioned figure. For free-falling atoms, the interferometer phase shift is generally given by linear and angular acceleration (Coriolis) components (Geiger et al. (2020)):

$$\Phi = -\boldsymbol{k}_{\text{eff}} \cdot \boldsymbol{a}T^2 + \boldsymbol{k}_{\text{eff}} \cdot (2\boldsymbol{\Omega} \times \boldsymbol{v})T^2. \tag{2}$$

In this formula, $\boldsymbol{k}_{\text{eff}}$ is the effective wavevector, $\boldsymbol{a}$ the linear acceleration experienced by the atom clouds relative to the mirror, $\boldsymbol{\Omega}$ and $\boldsymbol{v}$ the angular and linear velocities, respectively, and T the interrogation time, namely the time between two pulses (Figure 2). Routinely, $\boldsymbol{\Omega}$ is separately measured by means of complementary instruments, such as gyroscopes, or even by engineering special configurations with more than one atom interferometer, equivalent to both a gradiometer and gyroscope; thus, it is kept null by compensation. All of this allows to simplify the former equation:

$$\Phi = \boldsymbol{k}_{\text{eff}} \cdot \boldsymbol{a}T^2 = \boldsymbol{k}_{\text{eff}} \cdot (\boldsymbol{a}_M + \boldsymbol{a}_g)T^2, \tag{3}$$

where $\boldsymbol{a}_M$ denotes the acceleration experienced by the inertial reference frame (M stands for "mirror"), the same acting on the spacecraft Center of Mass (CoM), whilst $\boldsymbol{a}_g$ indicates the acceleration experienced by the center of the atom cloud, namely the acceleration of the satellite CoM together with the gravity gradient between satellite CoM and atom cloud (Yu et al. (2002); Xu et al. (2007b)).

According to Equation 3, the instrument described thus far, namely a one-arm single-axis interferometer, can be used as an onboard accelerometer. From Equation 3, it is evident that the sensitivity of the measurements, relying on Φ, scales quadratically with the interrogation time, T. Therefore, it is desirable to make T as long as possible, while curtailing the interferometer phase contrast the least. These goals are the main reason for which it is advantageous to have the atoms in microgravity: in these conditions, the atom ensemble can expand for seconds without displacement of its CoM, as the atoms are in free fall together with the enveloping apparatus and the spacecraft. However, this compromises the spatial resolution of the measurements. In space, the interrogation time is mostly limited by the free expansion of the atomic cloud, whose initial spatial distribution can be neglected (Tino and Kasevich (2014)).

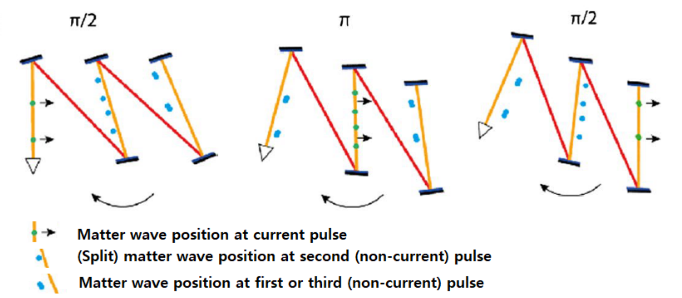

Fig. 4. Control mechanism to cancel Coriolis accelerations. Any additional small residual rotation errors are further compensated by an extra active tip-tilt actuation on the last retro-reflection mirror (Migliaccio et al. (2019)).

Additionally, as touched upon before with Equation 2, using the interferometer in a rotating frame implies the need to compensate for the effects of the Coriolis and centrifugal acceleration (Trimeche et al. (2019)). According to the aforementioned equation, the non-zero angular velocity should be multiplied by the random linear velocity of the atoms which would add to the measurement noise, hence the necessity to measure and compensate for rotation. This can be achieved by using three spatially-separated interaction regions for each Raman pulse, with dedicated retro-reflection mirrors that counter-rotate the single-laser wave vector accordingly, as shown in Figure 4. As a matter of fact, the mirrors are tilted to form an angle $\pm\theta_M = \pm\Omega_{orb}T$ (Ω_{orb} is the spacecraft orbital angular velocity) between Raman wave vectors at successive pulses to statically compensate for the rotation of the satellite (Trimeche et al. (2019); Migliaccio et al. (2019)), in order to to keep the wavefront vector $\boldsymbol{k}_{\text{eff}}$ fixed in inertial space. This obviously implies that accurate information about Ω_{orb} is provided by another subsystem.

2.2. Quantum measurement of gravity gradients

Thus far, a single-arm one-axis cold-atom interferometer has been discussed: it fulfils the role of an accelerometer, unable to sense gravity gradients. To this end, a differential approach must be adopted that engages two experiments separated by a baseline D, such that the gravity gradient results from the difference between the two gravity measurements divided by D. In reality, although a CAI gradiometer can be comprised of two physically-distinct CAI accelerometers, the differential approach can be engineered in the frame of a single interferometer, e.g. with multiple proof masses (clouds of atom), as long as these are separated by a baseline. This allows the great advantage of common-mode rejection of noise. In this regard, two major solutions are feasible. Firstly, in Figure 5 (a), two MOTs generate two different atom clouds, which both undergo a two-photon diffraction scheme (Figure 2). A common alternative is the use of an additional initial pulse to separate the starting cloud by a baseline: the two ensembles experience the same diffraction in two parallel interferometer arms, distanced by the baseline. This differential approach entails two decorrelated measurements, such that the overall instrument sensitivity becomes proportional to a factor of $\sqrt{2}/D$ (thus, gradiometric sensitivity). On top of this, it is possible to apply the double-diffraction scheme -or k-reversal approach Figure 5 (b)-. The diffracted atoms are all in the same state, different from the initial one, but vary in momenta (opposite). The difference in momenta is hereby doubled. Hence, this implies that the inertial sensitivity can be enhanced by a factor of 2 if compared to the initially described approach based on two-photon diffraction (Carraz et al. (2014),Malossi et al. (2009)).

In Figure 4, tilt mirrors have been suggested as a control mechanism for $\boldsymbol{\Omega}_M$[6], nonetheless, there are no current technologies that can ensure no mismatch at all, especially in an interleaved mode, namely when several interferometers are working concurrently (Douch et al. (2017)). Consequently, two main operational modes are conceivable: nadir pointing, which implies that z-axis is radially oriented, y- and x-axes are perpendicular and tangential to the orbital plane and that $\Omega_y = \Omega_{orb}(=\Omega_{M,y})$ and $\Omega_{x,z} \approx 0$; or (quasi-)inertial pointing for which $\boldsymbol{\Omega} \approx \boldsymbol{0}$ $(= \boldsymbol{\Omega}_M)$ with the x-axis and y-axis being orthogonal and tangential, respectively, to the equator at the reference meridian, whilst the z-axis is parallel to the planetary rotation axis. Nadir mode requires the knowledge of the spacecraft rotation rate in order to discern θ_M needed to counter-rotate the mirrors for rotation compensation, provided the availability of adequate technology. On the other hand, (quasi-) inertial pointing necessitates an approximately-constant satellite attitude, resulting in very strict pointing stability requirements [Migliaccio et al. (2019)]. Engineering mechanisms to maintain the apparatus stable are very challenging. Thus, nadir pointing is assumed in this work.

2.3. Instrument sensitivity

To ensure the desired sensitivity of the measurements, noise sources must be identified and with these, the Signal-to-Noise ratio (SNR). The fundamental contribution to the SNR is given by a limit proper to any quantum inertial sensor: the Quantum Projection Noise (QPN), or specifically atomic shot noise, which represents a minimum phase noise per cycle of

$$(\text{SNR})^{-1} \approx \sigma_{\Phi,\text{QPN}} = \frac{1}{C\sqrt{N_{\text{atoms}}}}, \tag{4}$$

given the impossibility to measure the exact populations of the final hyperfine levels of each atom cloud.

The QPN constrains the sensitivity to the phase shift, inherent to the measurement process, provided the possibility to discern nearby phase values dictated by the contrast C. QPN limits the gravity gradient survey such that the error per measurement is:

$$\sigma_{\text{GG}} = \sigma_{\Phi,\text{QPN}} \frac{\sqrt{2}}{k_{\text{eff}} T^2 D}. \tag{5}$$

[6] The subscript M denotes the apparatus' mirror.

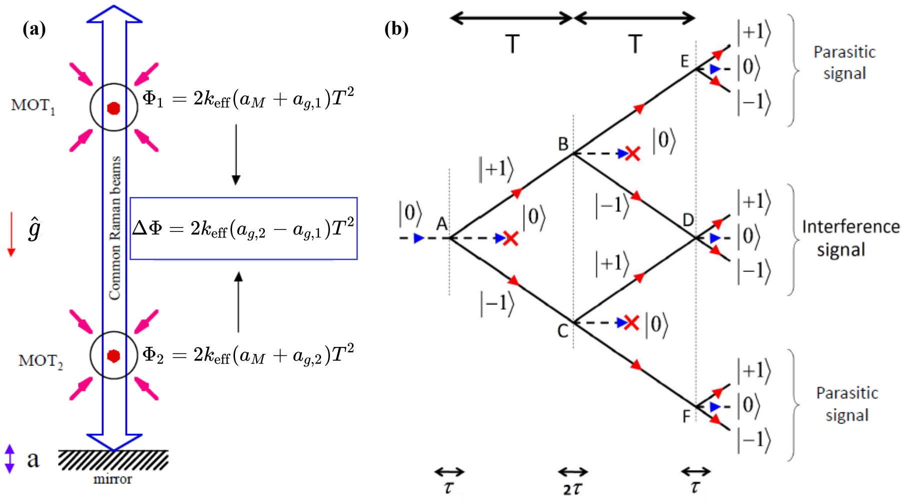

Fig. 5. (a): Illustration of differential approach: two MOTs generate an atomic cloud each; these share the same laser beams for high common-mode noise rejection (Yu et al. (2002)). (b): Scheme of atomic trajectories in double diffraction; the crosses indicate where blow-away beams are applied to get rid of the left-over population in the lower state $|0\rangle$ (Trimeche et al. (2019)).

Multiplying σ_{GG} by $\sqrt{T_{\text{cycle}}}$[7] gives the respective interferometer sensitivity to the gravity gradient and centrifugal acceleration ($\Delta\gamma$), provided that the signal frequency $f < (\frac{1}{2T})$. This is an operational restraint, dictated by the fact that naturally the frequency of the measurements must be smaller than the inverse of the interrogation time (Xu et al. (2007a)). In light of the assumption that the satellite rotation is perfectly known by a gyroscope (or that CAI is also engineered as such), the reduction of the centrifugal acceleration becomes negligible. The use of BEC allows to partially overcome the QPN and detection noise limitations on sensitivity, by offering a perspective towards the squeezing of spin states (refer to Gross (2012)), a particular strategy to surmount the standard quantum limit in metrology. As a matter of fact, squeezed BEC can help stretch the interferometer sensitivity out to the unavoidable Heisenberg limit (Abend (2017)), such that the sensitivity becomes dependent on N_{atoms} (instead of $\sqrt{N_{\text{atoms}}}$) (Xu et al. (2007b)).

The most optimistic estimate of a CAI gradiometer performance from literature is $\Delta\gamma$ = 3.5 mE/$\sqrt{Hz}$ (Carraz et al. (2015)), with 2T=10 s, D = 0.5 m, $N_{\text{atoms}} = 10^9$ atoms and T_{cycle} = 11 s. k_{eff} is equal to $4n\pi/\lambda$, where the impulse transferred to the atoms usually has n=2 (number of photon recoils) and $\lambda = 780nm$.

Observations errors based on pointing or position uncertainties were found to be lower even than the sensitivity of CAI 4, meaning that the gradiometer would not be able to discern them. Thus, these are not deemed an issue in this gravity field model recovery process.

As hitherto discussed, the observable with whom the quantity of interests can be retrieved is the interferometer phase: as such, it is subjected to possible phase ambiguities (if it is larger than 2π). To avoid any jumps in phase between cycles, all measurements must have a limit scale between each interferometer sequence. In Carraz et al. (2015), the limit scales for gravity gradient measurements were computed to be in the order of 10 E. This implies that the knowledge of these quantities should be better than the associated limit scale within T_{cycle}. The latter, together with the cross-talk time between interleaved measurements (Migliaccio et al. (2019)), imposes a limit to the continuity of the measurements (Xu et al. (2007b)).

2.4. Instrument selection

Currently, there are no commercially available cold-atom inertial sensors constructed for space applications, but many models have been conceived, some of which were successfully tested in microgravity, in a drop tower and in a parabolic flight (Carraz et al. (2015)). In Müller et al. (2020), two mission concepts are suggested as promising for gravity missions to Venus and Mars. The first is a GOCE-like gravity gradiometer concept, where the pairs of EGG are substituted by CAI gradiometers. The state-of-the-art CAI gradiometers are expensive and heavy (about 260 kg), yet a weight reduction to 50 kg and curtailed costs are expected in the next decade (Müller et al. (2020)). The second concept comprises a hybrid CAI accelerometer, with a targeted mass of 10 kg, which would help correct the drift errors of its complementary EGGs.

For this work, four different CAI configurations have been individuated (CAI 1 to 4), with increasing sensitivity (Equation 5). The sensitivity to accelerations (Δa) and gravity gradient ($\Delta\gamma$) are shown in Table 1, whilst the respective physics package properties are listed in Table 2. An estimate of SWaP budgets is reported in Table 3. These numbers are an average for a general CAI configuration, hence CAI 1 to 4 are hereby not differentiated.

Table 1. Gradiometers used for mission concept evaluation. The interferometer contrast is C > 0.6, which changes depending on the satellite attitude and rotation compensation system if any (Schuldt et al. (2015)).

Gradiometers	$\Delta\gamma$ $[mE/\sqrt{Hz}]$	Δa $[m/s^2/\sqrt{Hz}]$	Sampling Interval [s]
CAI 1	308	1.1E-10	1.6
CAI 2	104	3.7E-11	1.66
CAI 3	50	1.8E-11	3
CAI 4	3.5	1.2E-12	11

Finally, CAI technology and the subsidiary systems do not have any (space-)flight heritage. The cutting-edge interferome-

[7] T_{cycle}=2T+1s, whereby 1s is required for cooling.

Table 2. CAI 1 - 4 physics package properties (Müller et al. (2020); Trimeche et al. (2019)). The number of photon recoils is n = 2, meaning that the atoms undergo two-photon recoils. The spacecraft accommodating the payload is considered in nadir-pointing configuration.

Physics Package System	**CAI 1**	**CAI 2**	**CAI 3**	**CAI 4**
Atom Cooling Temperature [K]	10^{-6}	10^{-6}	10^{-6}	10^{-9}
Cooling Technique	MOT + Optical Molasses	MOT + Optical Molasses	MOT + Optical Molasses	BEC
Number of Atoms [-]	10^7	$6 \cdot 10^7$	10^8	10^6
Interferometry Time [s]	0.3	0.33	0.5	5
Duty Cycle (reloading) Time [s]	1	1	2	1
Baseline [m]	0.5	0.5	0.5	0.5
Number of Photon Recoils [-]	2	2	2	2
Rotation Compensation System	-	Coarse ($\approx$ 0.1mrad/s)	Fine ($\approx$ 1μrad/s)	Fine ($\approx$ 1μrad/s)

Table 3. SWaP budget for a general one-axis CAI, together with the target values for future space applications (CAI-TN4 2019). *Volume estimate in liters from (Schuldt et al. 2015).

Unit	**Dimensions**	**Mass**	**Power**
	Length x Height x Width [mm x mm x mm]	+ 20 % margin [kg]	+ 20 % margin [W]
Physics Package Unit	1050 x 440 x 810 (700 x 400 x 150)	160.4 (50)	128.4 (50)
Laser System	400 x 300 x 300 (150 x 20 x 150)	51.1 (5)	104.2 (50)
Electronic System	1000 x 300 x 300 (250 x 250 x 250)	52.4 (15)	601.5 (TBD)
Total	$\approx 470L*$	316.8	1000.9

ters have a rather low Technology Readiness Level (below 6[8]), which is the main reason for their delay in autonomous space operations. Experiments are being undertaken to improve its technology readiness for space applications (Abend (2017); Tino and Kasevich (2014)).

3. Orbit selection

In light of the fact that this work is not a mission design project, instead of conceiving a gravity reconnaissance mission from scratch, this section comprises the selection of an existing mission which can be exploited as a realistic case study, a.k.a. baseline, to retrieve the Spherical Harmonics (SH) error spectra with the methodology outlined in section 4. Afterwards, orbits deviating from the baseline by spacecraft altitude, inclination and eccentricity are contemplated to understand how alternative orbital geometries relate to the mission's scientific return. Finally, some aspects of mission design, relevant for this study, are touched upon.

3.1. Baseline Mission

To avoid steering the present work towards a mission design project, which would incur countless hours of undesired systems design, the first goal is to identify a suitable existing mission that can be exploited as a realistic baseline for the present study.

A gravity reconnaissance mission requires low-altitude and polar orbits to ensure strong and uniform signal sampling for homogeneous and consistent surface coverage. To respond to these requirements, a near-circular orbit may be an asset, albeit not necessary (as demonstrated in subsubsection 3.2.2). By looking

[8] Personal correspondence with Dr O. Carraz.

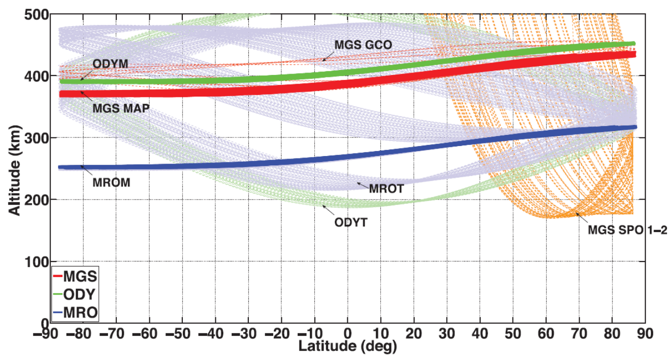

Fig. 6. MGS, ODY, and MRO altitude coverage versus geodetic latitude during mapping phases at Mars (Genova et al. (2016)). M or MAP stand for Mapping orbit, whilst T for Transition orbit; GCO and SPO are, respectively, Gravity Calibration Orbit and Science Phasing Orbit.

at Figure 6, amongst the Mars exploration campaign orbiters involved in the retrieval of MRO120F, the one providing the most suitable orbit is Mars Reconnaissance Orbiter (MRO) - as the label of the model hints - in its Mapping orbit, or Primary Science Orbit (PSO).

Launched in 2005 as part of the Mars Exploration Program (MEP), MRO was a multipurpose spacecraft, aimed to remotely conduct science observations to ameliorate the knowledge of the gravity field of Mars, amongst other scientific objectives (outlined in Greeley (2001); Zurek and Smrekar (2007)). MRO entered its Mars orbit on the 10^{th} of March 2006 and inserted into the PSO, the orbit of interest for this work, after aerobraking. It lasted from November 2006 until December 2008 (Menon et al. (2017)). The MRO's PSO was a frozen low-altitude and near-circular (250 x 315 km) orbit (112 minutes), with an inclination of 92.65° (Johnston et al. (2003)). The periapsis was fixed over the South Pole (with an argument of periapsis of 270°) and the spacecraft flew at approximately the same altitude whilst crossing each latitude circle. A lower orbit had not been chosen because of the larger atmospheric drag with descending altitude, which would have required frequent orbit trim manoeuvers. This not only would have demanded more fuel consumption, but also hindered the quality of measurements, that largely suffer from spurious accelerations[9]. The orbit geometry yielded a ground track repeat cycle of 17 days, ensuring the view of any surface point within a Martian season (Zurek and Smrekar (2007)).

3.2. Impact of orbit geometry

To explore the impact of mission orbit geometry on the solution achievable via CAI technology, other orbits were tested: the ideal orbit for gradiometry is very low, polar and circular (albeit not necessary), for a global uniform sampling of the Martian surface. Firstly, the dynamical model exploited to propagate these orbits is described below.

3.2.1. Dynamical model

Hereby, the main goal is to explore how different orbital geometries impact the mission scientific return in terms of SH error spectra. To this end, ideally, in order to study alternative orbits, the dynamical model of the baseline mission should be exploited by just tuning the spacecraft altitude, inclination and eccentricity, according to the needs. Nevertheless, NASA's Navigation and Ancillary Information Facility (NAIF) only provides MRO states and not the models employed in the orbit determination process, such as the atmospheric one. Thence, to explore the mission return of different geometry options, a dynamical model must be defined to propagate the orbits via Tudat[10]. This dynamical model encompasses:

- The gravity model for Mars was based on the spherical harmonic expansion with the coefficients from MRO120F, the latest gravity field model up to degree and order 120, available on Ward and Paul Byrne (2022).
- The DE430 planetary ephemerides (Folkner et al. (2014)), as part of the SPICE kernels, were exploited which include range data from the Mars orbiters (Konopliv et al. (2016)), as well as the rotation and body shape of major Solar System bodies. It is provided in Semenov and Baalke (2022).
- Tabulated atmospheres for Mars (average atmospheric density per altitude) was taken from the NASA's software Mars Global Reference Atmospheric Model 2010 (Mars GRAM 2010), downloaded from Lockney (2010). To retrieve the drag acceleration, the spacecraft mass was assumed to be 1000 kg, whilst the reference area and drag coefficient were 15.0 m^2(Mazarico et al. (2009)) and 2 (Genova et al. (2015)), respectively.
- Point mass gravity models for the Earth and the Sun, despite being very small, were included with the default settings in Tudat.
- For solar radiation pressure, the default Tudat model was used: the latter is modelled as a cannonball radiation pressure, whereby the effective force is collinear with the vector from the source, the Sun, to the target, namely the spacecraft. The reference area and radiation pressure force coefficient were 35.0 m^2(Mazarico et al. (2009)) and 1 (Genova et al. (2015)), respectively. Orbital perturbations caused by planetary radiation are rather small, on the order of 10% of those associated with direct solar radiation pressure (Borderies and Longaretti (1990)). For these reasons, planetary thermal and IR radiations were neglected.
- To simulate the system's dynamics, a Cowell propagator and a variable-step-size integrator, with the coefficients from the Runge-Kutta Fehlberg 7(8) method, were adopted. The propagation was performed in the global, pseudo-intertial central-body fixed reference frame. For simplicity, a single-arc dynamics simulator was exploited. The use of single arc was considered acceptable due to the nature of the exercise: only the state was required as input to the complementary code, the script from GOCE's 1b-level data processing (Siemes et al. (2014),Siemes (2018), Siemes (2008)), to obtain the gravity gradients (more on this in section 4).

3.2.2. Alternative orbits

The orbital elements of alternative orbits are selected according to the requirements of a gravity gradiometry mission, namely continuous, uniform and global observations. To this end, three sets of orbits have been individuated. The first encompasses three circular and polar orbits with an altitude as low as a spacecraft can fly for 1 Earth year without a propulsion system to compensate for orbital decay due to atmospheric drag. According to the simulations carried out on Tudat, with the dynamical models described above, the lowest altitude for which orbit maintenance is not required is 232 km. To study the impact of the orbital altitude on the gravity solution, also orbits with mean altitudes of 240 and 250 km have been considered.

A second sets of orbits comprises circular and polar orbits with very low altitudes such that a Drag-Free Control System (DFCS) is needed to maintain the orbit, to avoid decaying into the Martian atmosphere. The average altitudes considered were 150 and 100 km, as suggested in Zheng and Li (2018). To sustain these orbits, different maintenance strategies are discussed in subsection 3.3.

Finally, another type of orbit is also interrogated: low-perigee (100 km) elliptical orbit, with apogee and eccentricity of 1000 km and 0.12, respectively. Albeit elliptical, the orbit presents a rather uniform coverage of the surface in correspondence of the periapsis. Its distribution over the Martian surface is deemed rather uniform, as shown in Figure 7. Thus, the orbit is considered suitable for a gravity gradiometry mission. The spacecraft should be equipped with thrusters to be fired at the periapsis to trim the orbit, as addressed in subsection 3.3.

[9] This would not be the case with gradiometry given the intrinsic common-mode noise rejection.
[10] `docs.tudat.space`, last accessed on 13/10/2022.

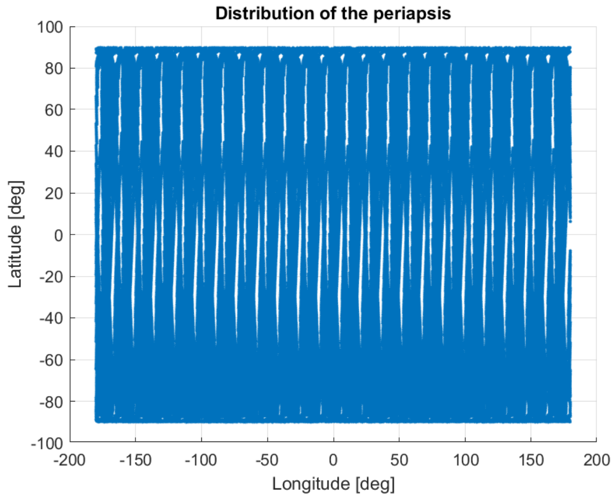

Fig. 7. Periapsis distribution of elliptical orbit over the surface of Mars.

3.3. Orbit maintenance strategies

The orbits with very-low altitudes require propulsion to delay the orbit decay into the Martian atmosphere. In the Tudat simulations, a tabulated averaged atmospheric-density profile has been exploited, as mentioned in subsubsection 3.2.1.

Exploiting this model, Figure 8 has been derived, which furnishes an idea of how the drag relates to the orbital altitude. The horizontal lines represent the maximum allowable thrust of two types of state-of-the-art ion engines, T5 (Randall et al. (2019)) and T6 (Snyder et al. (2012)). At 150 km the drag level is in the order of 10s of mNs, whilst at 100 km is 10s of Ns.

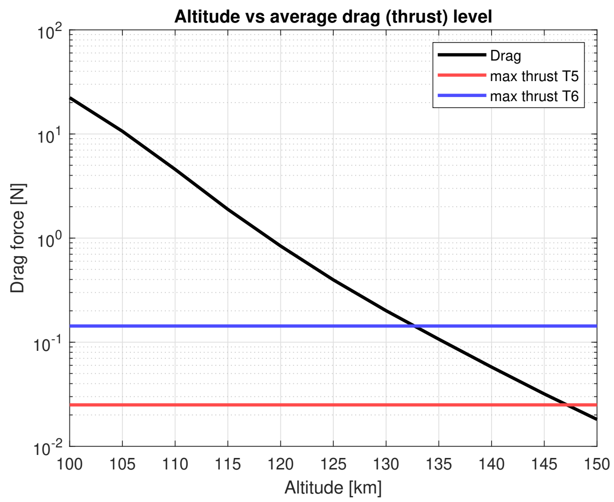

Fig. 8. Average drag (required thrust) level with orbital altitude. The T5 and T6 ion engines' maximum allowable thrust are taken from Randall et al. (2019) and Snyder et al. (2012).

To counteract the drag, equal continuous thrust must be provided by an onboard propulsion system. According to the image above, the lowest altitude for which ion thrusters (T6) are sufficient is 133 km, thus also this orbit was briefly explored. Mind that, in order to retrieve the drag, a model of average atmospheric density was employed. Hence, periods of higher density may occur, during which ion thrusters may not suffice to counteract the drag. Thus, for this mission concept alternative propulsion technologies may be required, for instance in case of a dust storm.

Clearly, the type of required engine depends on the thrust level. According to (Badami (2019)), at 150 km, ion thrusters are ideal. COTS options are T5 or T6 'Kaufman'-type electron bombardment ion motors running on Xenon gas. GOCE DFCS was based on two 700-W T5 Ion Propulsion Assembly (IPA), each of which has a maximum thrust level of 21 mN (Steiger et al. (2014)). T6, instead, was baselined for the BepiColombo mission to Mercury (Snyder et al. (2012)). At its full power (4.5 kW), the T6 throttles 143 mN of thrust with a specific impulse of 4120 s.

For the very-low orbit with the initial altitude (h_0) of 100 km, the ion thrusters - as considered before - cannot provide the required thrust level, hence the mission is possible only if more powerful solutions are found to be available, such as electromagnetic or chemical propulsion (Badami (2019)).

The principle of electromagnetic propulsion is based on ionized propellant accelerated through electromagnetic fields. This propulsion system displays high specific impulse, light weight, instant on/off capability and low noise (Badami (2019)). The main drawback in space applications is the insufficient flight heritage. The opposite can be said for chemical propulsion, such as liquid mono-propellant thrusters. For instance, hydrazine thrusters have a strong flight heritage and can deliver about 1 N of thrust when easily installed on board microsatellites. Nonetheless, because of the propellant's high toxicity and flammability, strict safety measures have to be taken during the entire process from design to launch. This yields substantial shipping costs as well as costly filling operations to be added to the already high price of the liquid (Leomanni et al. (2017)). Finally, an important limit to chemical propulsion is represented by the poor specific impulse I_{sp}, requiring higher propellant mass for the same delivered ΔV. A significant improvement (>30%) in Isp can be obtained by using cryogenic propellants, such as liquid oxygen and liquid hydrogen. Yet, historically, these propellants have not been applied beyond the upper stages of rockets (Badami (2019); Leomanni et al. (2017)) also because there are no technologies to store these propellants for years[11].

As far as the elliptical orbit is concerned, an analysis of the orbital altitude and the correspondent atmospheric drag was performed. The drag is substantial (>10 N) at its periapsis, thus a thrusting system is required to delay orbit decay, as without any orbit maintainence, the spacecraft would enter tha Martian atmosphere within 9 orbits. T5 or T6 engines are recommended.

To quantify part of the costs of these missions, the ΔV was computed, via Equation 6,

$$\Delta V = I_{sp} g_0 \ln \frac{m_0}{m_f} \tag{6}$$

where g_0 is 9.80665 m/s^2 whilst m_0 and m_f are the initial and final spacecraft masses. The I_{sp} for the T5 engine is retrieved from Randall et al. (2019), whilst for the T6 is read in Snyder et al. (2012).

At 133 km the thrust level is about 15 mN, thus the GOCE T5's I_{sp} is 2500 s and the T6's one is 4120 s. A proper derivation of the required ΔV is beyond the scope of this work: hereby, we just present a preliminary estimation. For a first-order approximation, to apply Equation 6, the propellant mass must be estimated. It is assumed to be the same that GOCE used during its last year of mission, namely 12 kg of Xenon (Steiger et al. (2014)). We decided to look at a similar gravity gradiometry

[11] Personal correspondence with Dr. ir. D. Dirkx.

mission (GOCE) that used the same ion engines assumed for this work. On top of this, in its last year of mission, GOCE flew very low in the terrestrial atmosphere, thus in similar conditions to the Martian orbits considered in this paper. The resulting ΔV with GOCE's engines is 296 m/s. If using the advanced T6, for the same ΔV, the propellant mass required is 7.3 kg. Similar values are found for the other two very-low orbits.

As a first level approximation, for the elliptical orbit, the drag is larger than 1 N for about 20% of the orbit, so the estimated ΔV is in the order of 55 m/s and the Xenon mass can be reduced to about 1.5 kg. Given the nature of the orbit, the spacecraft dives into the Martian atmosphere experiencing different orders of magnitude of drag in a short time lapse. Thus, more accurate analyses of the required ΔV and propellant mass are quintessential, yet these are beyond the scope of this work and are left for further studies.

Finally, the orbit and attitude control thruster may cause significant vibrations: an unstable work environment can significantly lower the observation accuracy [Zheng and Li (2018)]. Nevertheless, in contrast to other sensors, CAI devices are insensitive to such vibrations, given the common-mode noise rejection due to the differential nature of gradiometric measurements.

To conclude, the selected orbits are feasible for a sufficient mission duration (1 year), using existing technology.

4. Methodology

In this section, the methodology employed for the simulated gravity field reconstruction is outlined. Firstly, the basics of the theory of gravity field are reviewed, followed by a description of the covariance analysis, which represents the core method of the present work. In this regard, to start off, an analytical approach was sported as a fast first-order analysis of the gravitational error spectra, with reasonable accuracy, which is helpful in early mission planning activities (Bills and Ermakov (2019)). For the sake of completeness, as a more accurate, punctual and realistic study, numerical covariance analyses were also approached in detail. Finally, a strategy to account for the polar gap in the observations is outlined.

4.1. Theory of Gravity Field

According to Newton's fundamental law of gravitation (1687), the gravitational acceleration of a planet can be described as a three-dimensional vector field, determined from the gradient of the gravitational potential U which can be expressed in SH as (Torge (2001)):

$$U(r,\phi,\lambda) = \frac{GM}{r} + \frac{GM}{r}\sum_{l=1}^{\infty}\sum_{m=0}^{l}\left(\frac{R}{r}\right)^{l}\bar{P}_{lm}(\sin\phi)\cdot\left[\bar{C}_{lm}\cos(m\lambda)+\bar{S}_{lm}\sin(m\lambda)\right]. \tag{7}$$

where (r, ϕ, λ) are the spherical coordinates (radius, latitude and planetocentric longitude) of the computation point in the body-fixed frame; R denotes the main body's equatorial radius, whilst $(\frac{R}{r})^{l+1}$ indicates the field attenuation with altitude ($h = r - R$), implying the need for low orbital heights to sample a strong gravity signal; $\bar{P}_{lm}$ represents the fully normalized Legendre function (Torge (2001)).

Finally, $\bar{C}_{lm}$ and $\bar{S}_{lm}$ are the normalized SH coefficients with l^{th} degree and m^{th} order (Kaula (2013); Heiskanen and Moritz (1967)), whereby SH denote orthonormal basis functions exploited to sample the global structure, as well as the local irregularities, of a planet's mass distribution (Kaula (2013)).

The higher the SH degree is, the finer is the spatial resolution of the corresponding terms of the potential. The influence of the coefficients on the total gravitational potential can be approximated by the commonly-known-as Kaula's rule of thumb (Torge (2001)). As a matter of fact, in the expansion of the gravity potential, it is possible to define degree variances $V_l = \sigma_l^2$, such that

$$\sigma_l^2 = \sum_{m=0}^{l}\left[\bar{C}_{lm}^2 + \bar{S}_{lm}^2\right] \tag{8}$$

and whose square root can be converted in the Root-Mean-Square (RMS) amplitude, conventionally approximated by Kaula's rule of thumb (Kaula (2013)):

$$RMS_l = \frac{\sigma_l}{\sqrt{2l+1}} \approx \frac{k_p}{l^2}. \tag{9}$$

In Equation 9 k_p denotes the planetary Kaula scale factor: for Mars it is $13\cdot 10^{-5}$ (Marty et al. (2009)). The latter is a priori estimated based on self-similar fractals of planetary surfaces, compared to the Earth's; once measurements are obtained, k_p is updated by confronting planetary gravity power spectra (Mazarico et al. (2014b)). The maximum degree that can be resolved for a gravity field harmonic expansion, namely the model resolution, depends on the level of global coverage of the body's surface (Visser (1992)). Furthermore, Equation 9 is also used to estimate an upper bound for the SH coefficients at high degrees, as explained shortly hereafter. This limit is a measure of the uncertainty in gravity or geoid anomaly (Council (1997)).

Finally, a cumulative amplitude of the signal/error power spectrum can be defined, as a function extending over the entire spectral band from the minimum to the maximum degree (Liu (2008)):

$$\sigma_{l_{\min},l_{\max}} = \sqrt{\sum_{l=l_{\min}}^{l_{\max}}\sigma_l^2}. \tag{10}$$

Furthermore, the second-order gradients of U are relevant for gravity gradiometry, hence these are hereby introduced and expressed in the compact form of a gravitational gradient tensor, or Eötvös tensor T (Pail (2015)):

$$\left[U_{ij}\right] = \text{grad}(\text{grad}\,U) = \begin{pmatrix} U_{xx} & U_{xy} & U_{xz} \\ U_{yx} & U_{yy} & U_{yz} \\ U_{zx} & U_{zy} & U_{zz} \end{pmatrix}, \tag{11}$$

which includes the gravity gradient

$$\text{grad}(U) = \begin{pmatrix} U_x \\ U_y \\ U_z \end{pmatrix}. \tag{12}$$

In Equation 12, the local frame is such that the x- and y-coordinate are in along- and cross-track direction, whilst z is in radial direction (RSW frame). According to this, U_x and U_y form the horizontal gradient: these, by definition, point in the direction of the maximum gravity increase within the respective plane; the vertical component or vertical gradient, U_z, is a measure of the gravity variation with height.

4.2. Covariance Analysis

In the process of future planetary mission design, the potential accuracy of gravity field models can be anticipated through simulations with complex software tools (Bills and Ermakov (2019)). The gravity field model recovery from quantum measurements is a closed-loop iterative process. Routinely, due to the large amount of data, as well as the number of unknowns, the comparison and, finally, the convergence step is performed through a weighted Least-Squares Adjustment (LSA). In fact, the process of gravity field model recovery mainly consists of the inversion of satellite measurements to retrieve dynamical parameters and, especially, spherical harmonic coefficients. Nevertheless, these processes can require a long time and high computational effort, thus simpler, but still reasonably accurate studies were hereby performed. Mainly the gravitational signal error spectra were investigated. To this end, the core of this work is the covariance analysis of the estimatable parameters, here the SH coefficients.

In general, covariance matrices from the LSA provide a measure of the achievable parameters' precision, especially by retrieving the Formal Errors (FE), namely the square root of diagonal elements of the parameter covariance. The FE would be true errors if the dynamical model exploited in the covariance analysis were error-free, and if the measurement noise is uncorrelated with a Gaussian distribution, and that the weight diagonal values are a good representation of those that will occur in reality. Hence, these may be too optimistic if systematic forces and measurement model errors were not taken into account; this is why a detailed dynamical model was adopted (subsubsection 3.2.1). Furthermore, once a complete spatial sampling is achieved, assuming uncorrelated observations, the computed covariance matrix is inversely proportional to the square root of the number of measurements within a given epoch, provided that the change in the number of measurements does not influence the parameters' correlation.

To reduce the considerable computational effort, in this work only the zz component of the gravity tensor was considered, which contributes the most to the overall gravity solution[12]. To this end, it is assumed that the gradiometer is oriented such that the z-axis is pointing toward Mars, the x-axis into flight direction, and the y-axis completes the right-hand system. This decision also stems from the fact that a single-axis gravity gradiometer is largely less complex, thus cheaper, than multi-axis ones, still achieving very satisfying results, as shown in section 5.

When recovering the spherical harmonic coefficients vector, $\mathbf{x}$, from any observation vector $\mathbf{z}$, the respective error in the j-th parameter, σ_j, is the square-root of the covariance-matrix diagonal element ($\sqrt{C_{j,j}}$, where $\mathbf{C} = \left(\mathbf{A}^{\mathrm{T}}\mathbf{W}\mathbf{A}\right)^{-1}$), given the linearised least-square solution (Bills and Ermakov (2019))

$$\Delta \boldsymbol{x} = \left(\mathbf{A}^{\mathrm{T}}\mathbf{W}\mathbf{A}\right)^{-1}\left(\mathbf{A}^{\mathrm{T}}\mathbf{W}\cdot\Delta \boldsymbol{z}\right). \tag{13}$$

$\mathbf{A}$ and $\mathbf{W}$ represent, respectively, the information or design and weight (or observation covariance) matrices:

$$A_{i,j} = \frac{\partial z_i}{\partial x_j}; \quad W_{i,i} = 1/\varepsilon_i^2. \tag{14}$$

ε_i denotes the i-th measurement error. As formulated above, the weight matrix is a diagonal matrix, which holds in case of uncorrelated errors, compliant with the expected noise characteristics from a CAI gradiometer. $\left(\mathbf{A}^{\mathrm{T}}\mathbf{W}\mathbf{A}\right)$ denotes the normal matrix $\mathbf{N}$, inverse of the covariance matrix.

The design matrix for the SH coefficients can be written as follows:

$$A = \left[\frac{\partial z}{\partial \bar{C}_{lm}}, \frac{\partial z}{\partial \bar{S}_{lm}}\right] \rightarrow \frac{\partial z}{\partial \bar{C}_{lm}} = \frac{\partial z}{\partial \bar{C}^s_{lm}} + \frac{\partial z}{\partial \Delta\bar{C}_{lm}}, \tag{15}$$

whereby, the SH cosine coefficients (the exact same can be drawn for the sine coefficients) can be written as the sum of a static and a dynamic term (Genova et al. 2016):

$$\left(\bar{C}_{lm}\right) = \bar{C}^s_{lm} + \Delta\bar{C}_{lm}. \tag{16}$$

A can be rewritten as follows

$$A = \left[A, A\cdot A^k_{\bar{C}_{lm}}\cos\left(\frac{2k\pi}{T}\Delta t\right), A\cdot B^k_{\bar{C}_{lm}}\sin\left(\frac{2k\pi}{T}\Delta t\right)\right] \tag{17}$$

k indicates the fraction of martian year, T the martian orbital period (686.98 days) and Δt the elapsed time with respect to a reference epoch (Genova et al. 2016).

The covariance analysis as introduced in this section can be performed by following either analytical or numerical approaches. Both are discussed below.

4.2.1. Analytical Covariance Analysis

The analytical covariance analysis for this work was performed according to Bills and Ermakov (2019), a study focused on the retrieval of gravitational error spectra. The main underlying assumptions must be mentioned. Primarily, the geometry of the spacecraft orbit is restricted to two dimensions only, as the target body, the vehicle and the ground stations are assumed to be co-planar. Additionally, the mission observables are considered uniform in time (constant and continuous sampling, with no obscuration of radio signals when the spacecraft is not "visible" from the ground stations). To this end, the orbits are assumed to be circular and with polar inclinations. The mission duration is considered to start from a domain of already global coverage of the planetary gravitational field: in fact, at the beginning of a mission, information about the gravitational field increases linearly with time, as the planetary surface is for the first time slowly being fully covered. Only after a while, the spacecraft revisits regions of the surface; at this point, the retrieved gravity error decreases inversely with the square root of the number of independent measurements. The major limitation of this method is how to assess the impact of orbital geometry and measurement type (Bills and Ermakov (2019)).

Given the aforementioned assumptions, the gravitational error spectra are computed for radial measurements only; at spherical harmonic degree l, these are estimated according to the following expressions[13]: for gradiometry σ_l^G is

$$\sigma_l^G = \left(\frac{\varepsilon_G}{\sqrt{N}}\right)\left(\frac{1}{n^2}\right)\left(\frac{r}{R}\right)^l \frac{1}{(l+1)(l+2)}. \tag{18}$$

In this expression, r represents the spacecraft distance from the centre of the planet, n denotes the mean motion of the vehicle, N indicates the number of measurements and, finally, ε_G is the root sum square (RSS) of the measurement errors expected in a specific mission concept. In this paper, ε $[E/\sqrt{Hz}]$ comprises gradiometer errors as listed in Table 1.

[12] In Yi et al. (2013), an analysis based on GOCE's gradiometers showed that the contribution of U_{zz} is the highest, with an average value of 32.74% of the total solution.

[13] for the verified analytical derivation, the reader is re-addressed to Bills and Ermakov (2019).

4.2.2. Numerical Covariance Analysis

The numerical covariance analysis was performed by adapting the C. Siemes' code for GOCE gravity field model retrieval (Siemes et al. (2014)[14]), whereby the inputs are the satellite states and outputs the coefficients' standard deviations. In this context, we remind that we assume measuring the vertical gravity gradient and nadir pointing, which eliminates the need to apply rotations to account for the satellite attitude. The code was simplified such that the normal matrix, given its sparse nature, was approximated by a block-diagonal matrix as described by Schuh (1996). This is feasible under the assumptions discussed shortly hereafter. The inversion of the block-diagonal approximation of the normal matrix readily provided an approximation of the coefficients' covariance matrix, which contains the information on the observational geometry (Baur et al. (2008)).

Equation 13 can be rewritten as follows (Baur et al. (2008))

$$\hat{\mathbf{x}} = \mathbf{N}^{-1}\mathbf{b} = \mathbf{C}\mathbf{b}. \tag{19}$$

whereby, $\mathbf{N}$ and $\mathbf{C}$ are, respectively, the normal and covariance matrices.

A block-diagonal approximation of the normal matrix, $\mathbf{N}_{bd}$, can be used as a preconditioner of $\mathbf{N}$.

The computation of the block-diagonal matrix is much more efficient and quicker than the calculation of the full normal matrix, as only a small fraction of the matrix elements must be computed. At the same time, the inversion of the matrix is also much faster, since the numerical complexity of a matrix inversion is $O(n^3)$ where n is the number of rows. In this work, the square root of the diagonal elements of the covariance matrix (inverse of preconditioner) was used as the FE of the parameters (SH coefficients).

In order to approximate the normal matrix with a preconditioner whose peculiarity is the block-diagonal structure (Figure 9, right figure), an assumption must be made: the observations are distributed uniformly along a line of constant latitude, which is deemed realistic given the (circular) polar nature of the orbits considered in this work. In detail, for each parallel crossed, the observations must be of the same kind, must have homogeneous weights, must lie on an equi-angular grid and must not present any gap (Schuh (1996)), as visible in Figure 9 (left figure).

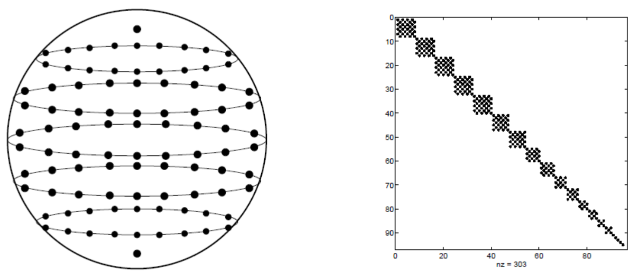

Fig. 9. Data distribution on the left and structure of the normal equations on the right for five parallels and data at the poles, symmetric with respect to the equator. Spherical Harmonics up to degree and order 9 (Schuh (1996)).

On top of this, the approximation is feasible if the SH coefficients are ordered according to a specific scheme. The latter is organized per order (Figure 10).

[14] Other correlated references to the theory behind this work are Siemes (2018) and Siemes (2008).

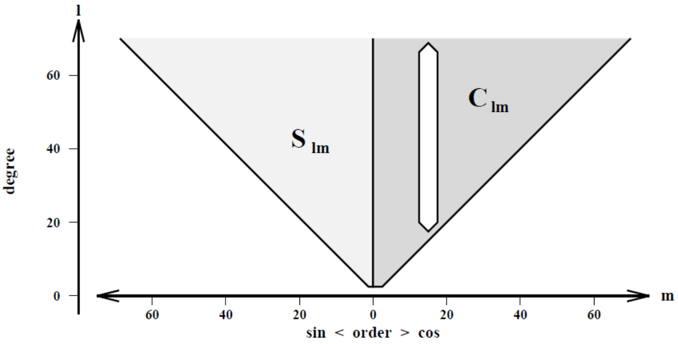

Fig. 10. Numbering scheme organized per order. The vertical sequence means that the inner loop of the coefficients gathering scheme corresponds to the degree, thus all coefficients with the same order are collected first (Schuh (1996)).

To this end, Schuh (1996) suggests that the optimal numbering scheme of the coefficients is $\mathcal{NUM}\{m(\ell C + \ell S)\}$:

$$\sum_{\ell=2}^{\ell_{max}} \bar{C}_{\ell 0} + \sum_{m=1}^{\ell_{max}} \left(\sum_{\ell=\max(2,m)}^{\ell_{max}} \bar{C}_{\ell m} + \sum_{\ell=\max(2,m)}^{\ell_{max}} \bar{S}_{\ell m} \right), \tag{20}$$

meaning that within each order first all cosine coefficients are collected and then all sine coefficients.

This numbering scheme provides that the normal equations are built in an optimal way with respect to the vanishing (zero) elements, given the orthogonality conditions of the discretized sine and cosine series.

In this way, the block-diagonal nature of the normal equations allows an easy numerical treatment of large systems. As a matter of fact, the computation can be independently performed order per order (Schuh (1996)).

4.3. van Gelderen and Koop strategy

MRO's PSO was selected as a baseline orbit for the covariance analysis. The spacecraft flew with an inclination of 92.6°, yielding a slight polar gap in the observations. As a matter of fact, a certain spherical cap around the poles was not covered by observations, thus a part of the spherical harmonic coefficients shows a high variance for low orders (due to a high condition number of normal equation matrix). Which coefficients are affected can be predicted with the rule-of-thumb by van Gelderen and Koop (vGK) (van Gelderen and Koop 1997). With a polar gap, the solution is accurate where observations are available, otherwise noisy. Calculating a global RMS is then averaging low-noise areas and high-noise polar gaps. To leave out the area around the poles in the calculation of the RMS, certain degree variances must be excluded. For a given degree l and inclination I, the maximum order m affected by the polar gaps and to be excluded from the solution is

$$m_{max} \approx \left| \frac{\pi}{2} - I \right| \cdot l. \tag{21}$$

5. Results and Discussion

This section reviews the main results of this work, mostly degree-RMS plots for gravity fields, and provides a discussion thereof. To start off, the outcome of the baseline mission's analysis is presented and then the other orbits are discussed. Finally, a description of the mission scientific return follows.

5.1. MRO's Primary Science Orbit

To simulate the gravitational RMS amplitude spectra from MRO's PSO, both the analytical and the numerical covariance analyses were performed. The solution was studied for 1 Terrestrial year (January 1^{st} 2007 to January 1^{st} 2008) and about 1 Martian year (January 1^{st} 2007 to October 1^{st} 2008).

The analytical approach discussed in subsubsection 4.2.1 was used to retrieve the FE for the four different CAI configurations, as shown in Figure 11.

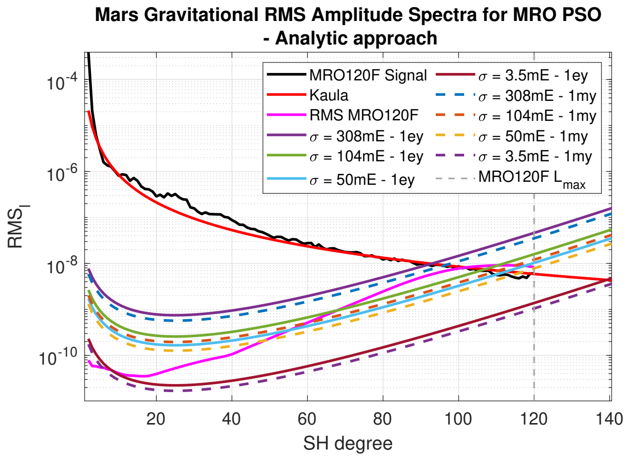

Fig. 11. Degree-RMS plot for MRO's PSO following the analytical approach. 1ey and 1my refer, respectively, to 1 terrestrial and Martian year.

The point of intersection of the line of Kaula's rule of thumb (signal) and the RMS curves (noise) represents the maximum SH degree that can be resolved for which the Signal to Noise Ratio (SNR) is 1. This is named the degree strength.

According to the pink curve in Figure 11, even though the maximum degree of MRO120F is 120, the degree strength is 100, meaning that degrees between 101 and 120 contain more noise than signal. It is worth noticing that the pink curve bends down at degrees higher than the degree strength (100), signifying that the coefficients with high degrees were "regularized", namely forced toward zero.

By looking at the figure, to obtain a degree strength superior to degree 120 and an improved SNR w.r.t. the model, the CAI 4 instrument must be employed, hence the most sensitive, complex and expensive instrument.

The difference between the 1ey and 1my solutions is not relevant. This is because, as clear from Equation 18, the RMS depends only on the inverse of the square root of the number of measurements. This entails that one year of uniform and global observations is sufficient to obtain satisfying results.

Furthermore, as expected, at very low degrees the FE of the gradiometry-derived solutions are larger than the current Doppler-based ones. As a matter of fact, the latter was achieved by processing over 15 years of radiometric tracking by MRO, ODY and MGS missions, whilst our results only account for 1 year of observational data. Yet, most importantly, Radio Science (RS) features higher sensitivity to large-scale variations in the gravity field. Gravity gradients, on the other hand, are less sensitive because the large scale signals are less prominent in higher-order spatial derivatives. On top of this, compared to gradiometry, Doppler tracking yields higher cumulative errors and steeper curves. A higher slope indicates that a decrease or increase of mission performance would yield little effect on its spatial resolution, but a large impact on its ability to resolve time-varying signals (Rummel et al. (2002)). On the other hand, higher low-degree FE and, most importantly, the flat slope for gradiometry, imply the theoretical inadequacy to sense gravity temporal variation, rather than spatial resolution ('extended spectral window effect' Rummel et al. (2002)).

The numerical approach, introduced in subsubsection 4.2.2, was used to produce the results shown in Figure 12. To attain the FE, the real satellite states from the NASA kernels were used as inputs in the preconditioning script (subsubsection 4.2.2). In Figure 12 only CAI 4 was contemplated because from Figure 11 it was the only one for which the current model could be outperformed in terms of maximum degree and SNR. Given the polar gap (I ≈ 92.6°), the strategy outlined in subsection 4.3 was hereby adopted, as visible in Figure 12. The RMS per degree was found by combining the first part of Equation 8 and Equation 10.

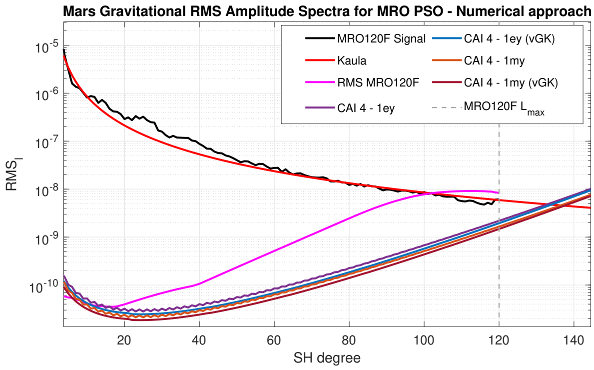

Fig. 12. Degree RMS plot for MRO's PSO following the numerical approach. 1ey and 1my refer, respectively, to 1 Terrestrial and Martian year. vGK stands for van Gelderen and Koop approach.

At degree 100, where the SNR for MRO120F is 1, these solutions display a SNR of about 28. This substantial improvement is due to the flat behaviour (see Figure 12) of the error curves for gradiometry w.r.t. the model's error line.

Furthermore, Table 4 summarizes the degree strengths from the graphs presented thus far.

Table 4. Degree strength of different approaches for MRO Primary Science Orbit.

	CAI	1ey	1my
analytical approach	1	92	97
	2	106	111
	3	112	116
	4	139	143
Numerical approach	4	133 (vGK 134)	137 (vGK 138)

From the table above, it is evident that only CAI 4 is suitable to ameliorate the MRO120F solution. The discrepancy between the analytical and numerical approach for CAI 4 is dictated by the assumptions of the former (strictly circular and perfectly polar orbit). Leveraging these results, the analytical solution is deemed a good first-order approximation. At the same time, though, given the close-to-polar inclination, the vGK's method does not bring substantial improvements to the solution.

The degree strength distribution over the globe is visible in the following degree strength map (Figure 13) with a 5-degree step in longitude and latitude.

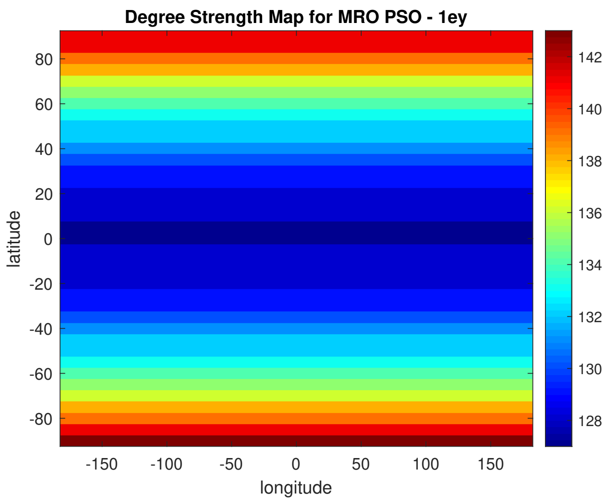

Fig. 13. Degree strength map for a gradiometry mission with MRO's PSO .

The highest degree strengths are located at the south pole in correspondence to MRO's periapsis. An improvement is clear if compared to the latest map available in literature (Figure 14), whereby the same asymmetry is present but the degree strengths are lower. In both maps, there is a homogeneity of results with respect to latitude: this is attributed to the quasi-circular and near-polar orbit, yielding rather homogeneous global surface coverage.

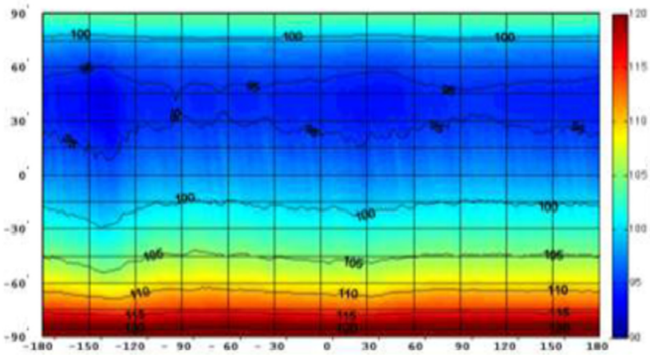

Fig. 14. The resolution of the Mars gravity field MRO120D from the covariance matrix of the solution. The minimum resolution is a harmonic degree of 90 and improves over the south pole (120) due to the lower altitude of the MRO's orbit ((Konopliv et al. 2016)). Mind that the resolution of this figure is the same as available in literature.

As a matter of fact, even though the MRO120D[15] gravity field has been constrained up to harmonic degree 120, the actual global resolution is lower - about degree 95. The average uncertainty in the coefficients nearly equals the coefficient magnitude (Konopliv et al. (2016)). On the other hand, our model's resolution ranges between 127 and 143.

Thus far, the numerically computed error spectra were explored. The respective coefficients FE are hereby confronted with the standard deviations from the MRO120F model. The ratio of the former to the latter is shown in Figure 15 for 1 terrestrial year. For the sake of brevity, the respective plot for 1 Martian year has been omitted. The pattern of the ratios is the same in the two figures, yet the maximum in the left-out image is slightly lower (5.17) given the longer mission lifetime.

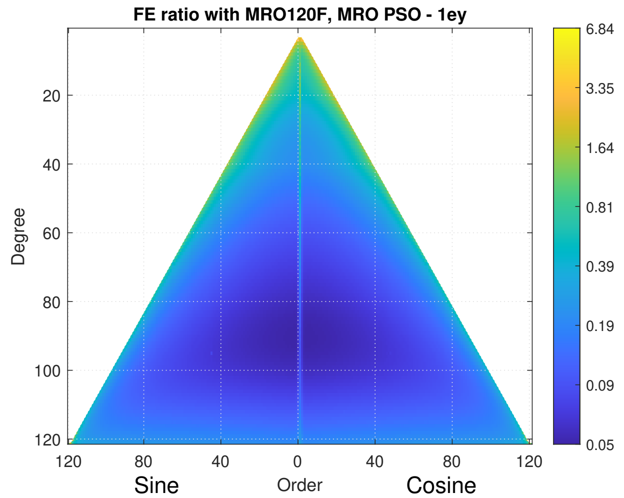

Fig. 15. Ratio of the computed FE and the model for 1 Earth year.

The pyramidal plot reveals a visible improvement: most of the computed formal errors are smaller than 30% with respect to the model ones. An exception is represented by the sectorial and the very-low degree terms, due to the nature of the orbit (non-perfectly circular nor especially polar, yielding a polar gap).

Finally, from this pyramidal figure, the higher precision of the simulated solution with respect to the MRO120F model can be appreciated.

5.2. Time-Varying Gravity

On Mars, seasonal variations of the gravity field are evident due to the change in atmospheric pressure and the size of polar caps, whereby condensation, sublimation and precipitation of CO_2 happen seasonally. Theoretically, geodetic signatures of the CO_2 cycle can be extrapolated from the study of time-varying zonal gravity parameters, $C_{n,0}$ (Karatekin et al. (2005)). The lower the degree the longer the wavelength of the gravity signal, fundamental to constrain the global-scale changes in terms of density or mass(Smith et al. 2009). In particular, the zonal terms (zero order) best describe the change in distribution along the lines of longitude.

To this end, according to the definition of the time-varying design matrix in Equation 17, the FE of the correspondent sine and cosine constants (As and Bs) have been retrieved for low degrees. These were compared to the values found in Genova et al. (2016), as visible in Figure 16. The latter were retrieved via radiometric tracking data from MRO, ODY and MGS orbiters.

In these plots, the computed FE (A_k and B_k) are higher than the ones found in literature (the black curve). These plots indicate that the signal (solid coloured lines) can be estimated via gradiometry but RS (with over 15 years of measurements) is better at constraining the time variations at the low degrees. Nevertheless, Sorrentino et al. (2014) has proven that CAI-based gradiometers display a flat noise power spectral density for all frequencies, thus preventing the spectrally coloured noise of the EGG in the lower frequencies spectra. Together with this, the

[15] This model was derived prior to MRO120F, for which additional 4 years of data were included to retrieve the SH coefficients (Konopliv et al. (2020)).

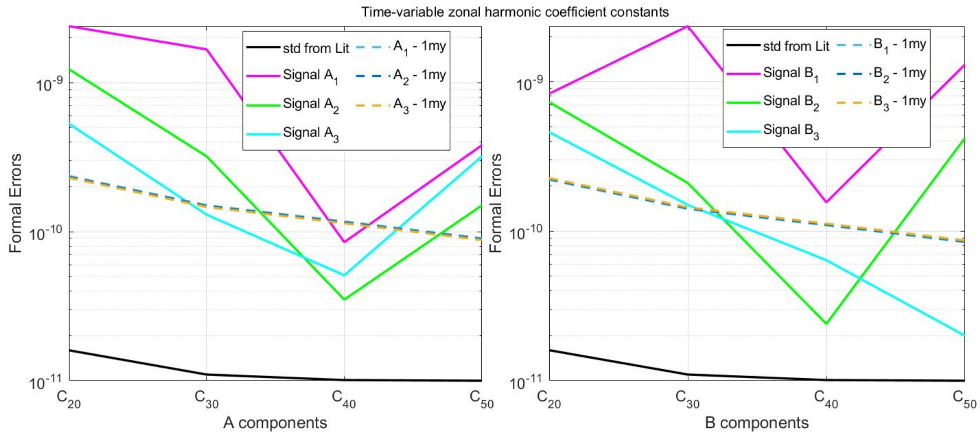

Fig. 16. Time-variable-coefficient constants signal (Signal A_k and B_k) and FE ("A_k and B_k") compared to values from literature retrieved via Radio Science (RS). Simulation for 1 Martian year (1my). k=1,2,3 mean that the signal frequencies considered were 1, 1/2 and 1/3 of the year. Mind that the (dashed) noise curves overlap.

high sensitivity of the measurements entails that the use of CAI-based devices would permits to address the requirements of a mission aiming at both the static and time-varying gravity field recovery (Douch et al. (2017)), yet provided that a longer mission lifetime is ensured (Migliaccio et al. (2019)).

Additionally, as the simulation period was 1 martian year, the parameters' correlations do not generate any problems because the signal is analysed as made up of orthogonal base functions. Thus, for a period equal to k-multiples of the martian period there are no correlation issues, complying with the assumption of uncorrelated measurements of this work.

5.3. Other orbits

The same preconditioning algorithm used for MRO's PSO was hereby exploited for several orbit geometries. For the lowest orbit without a DFCS (h_0=232 km), the degree-RMS plot was built for the four CAI instruments. The results are shown in Figure 17.

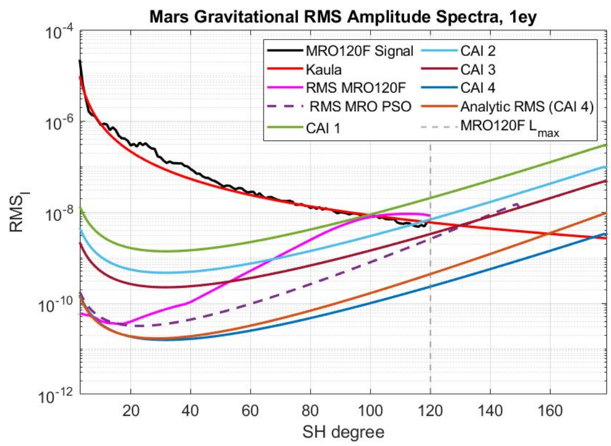

Fig. 17. Comparison of different gravity field error spectra from the 4 interferometers for the orbit with h_0=232 km. The purple dashed curve refers is taken from Figure 12 (with CAI 4).

In the figure above, for comparison purposes, the purple dashed line corresponds to the analysis done in the previous section about MRO's PSO with CAI 4. For that case, the achieved degree strength is the same as the one obtained with CAI 3 and the 232-km-altitude orbit, yet the latter displays higher cumulative RMS (the respective curve has a higher initial value).

The greatest improvement is given by the CAI 4 curve: not only in degree strength, which is 174, but also in terms of the RMS for low degrees, yielding an enhancement in terms of the cumulative error spectra and especially SNR. For longer simulations, the curves shift by a factor inversely proportional to the square root of the number of measurements. 5 years of mission with CAI 4 would yield a degree strength of 186. In this case, though, in the long term, altitude control thrusters would be required (Zheng and Li (2018)) to avoid orbit decay into the Martian atmosphere. Given the relatively little increase in degree strength, as a consequence, one-year mission is recommended.

As done for MRO's PSO, the degree strength map was built as shown in Figure 18.

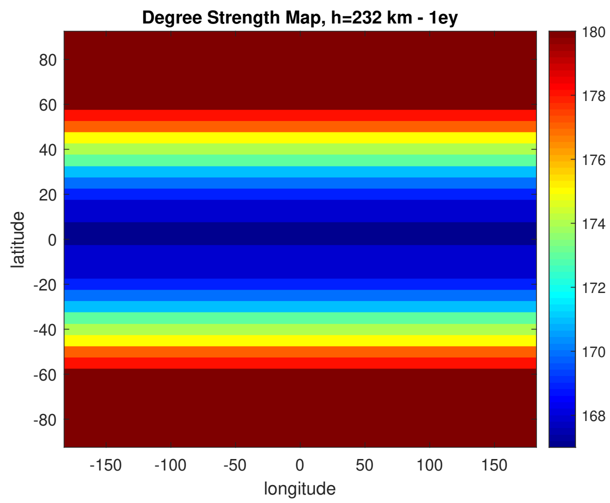

Fig. 18. Degree strength map for the lowest-altitude orbit without DFCS (h_0 = 232 km).

With respect to Figure 13, here the map is symmetrical given the circular polar nature of the orbit and has higher achievable degree strengths (up to 180). Thence, this instrument/orbit combination holds the promise to enable a large enhancement of the spatial resolution of the Martian gravity field models. The other consideration done for the previous map (Figure 13) about the homogeneity of the solution w.r.t. latitude holds here, too.

To obtain the greatest performance, CAI 4 was selected to investigate the result of gradiometry for the other orbital altitudes, individuated in subsubsection 3.2.2. The analytical approach is also used for each case, as shown below in Figure 19.

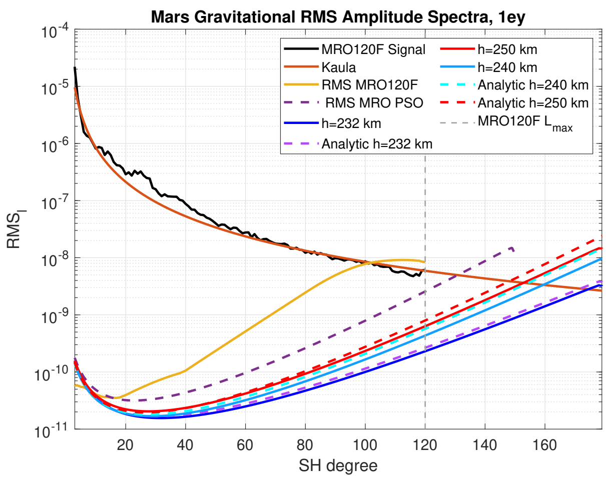

Fig. 19. Juxtaposition of the performance of missions with h_0 equal to 232, 240 and 250 km with CAI 4; both numerical and analytical approaches were applied. For comparison purposes, also the MRO's PSO results were shown (dashed purple curve).

For each altitude without a DFCS (h_0 = 232, 240 and 250 km) both the analytical and numerical approaches were exploited to retrieve the correspondent degree-RMS plot. In the image above, the dashed curves (analytical approach) are slightly higher than the solid ones (numerical analysis). The deviation of the analytical and numerical approaches is dictated by the orbital decay not accounted for in the former approach (the spacecraft gets closer to the surface with time). Moreover, at degree 100, compared to a SNR of 1 for MRO120F, the best SNR attainable with these missions at this degree is obtained with h_0= 232 and equals 83. A significant improvement is visible in Figure 19 as the curves slightly shifted down with respect to the previous analysis of MRO's PSO and, above all, are flatter. Furthermore, the degree strengths are shown in Table 5.

Table 5. Degree strength for different orbital altitudes (without a DFCS) and approaches with CAI 4.

Initial Altitude	analytical	Numerical
232 km	160	174
240 km	154	172
250 km	148	153

These numbers testify the large potential of CAI technology: with only one year of mission, a single orbiter accommodating a CAI 4 would significantly outperform the current model, which embodies the product of processing data from many spacecraft and lots of years of mission.

Much higher performance would be achieved by flying the spacecraft at even lower altitudes. As a consequence, degree-RMS plots were developed for the very-low-altitude orbits (selected in subsubsection 3.2.2) equipped with orbit maintenance subsystem (h_0=150 and 100 km). The errors have been propagated for degrees up to 300. This process requires high computational effort (more than 24 hours) thus the propagation was not done for higher degrees, nor the degree strength map was built. The plots are shown respectively in Figure 20 and 21.

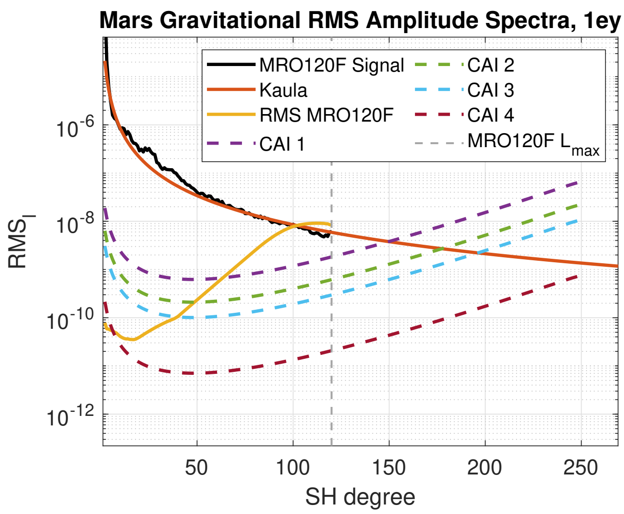

Fig. 20. Degree-RMS plot for the orbit with h_0=150 km with a DFCS.

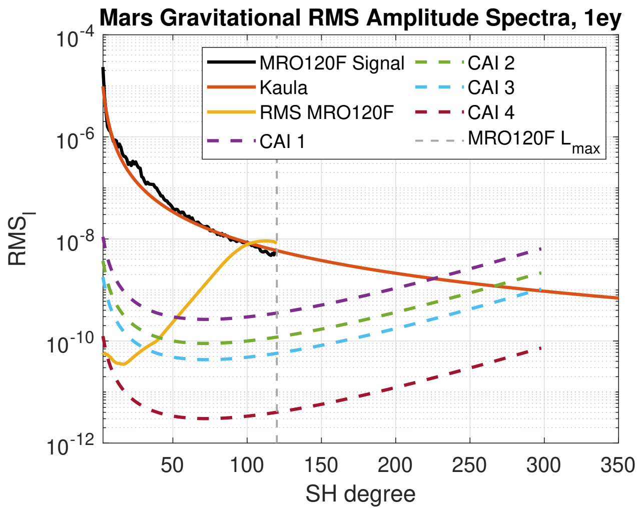

Fig. 21. Degree-RMS plot for the orbit with h_0=100 km with a DFCS.

At degree 100, where MRO120F displays a SNR of 1, the highest SNR that can be achieved is $6{\cdot}10^2$ for the 150-km altitude mission and $2.4{\cdot}10^3$ for 100-km one, both with CAI 4. These great enhancements in SNR are attributed to the fact that, as visible in the two plots above, the error curves, in addition to being rather flat, are largely shifted down with respect to the previous missions (Figure 19). Furthermore, the respective degree strengths are summarized in Table 6. The degree strength for CAI 4 (h_0=100 km) was found by extrapolating the correspondent dashed curve with a 4^{th} degree polynomial and corresponded to 390.

Furthermore, the orbit with the lowest altitude for which ion thrusters are sufficient (h_0 = 133 km, as discussed in subsection 5.3) was also briefly analysed. Thus, a degree-RMS study has been conducted, resulting in the degree strength listed in Table 6.

Table 6. Degree strength for very-low (150, 100 and 133 km) circular polar orbit with different CAI configurations.

CAI	Degree strength		
	h_0=150 km	h_0=100 km	h_0=133 km
1	151	227	165
2	178	266	194
3	196	294	209
4	265	≈390	295

These results are very promising, especially because the less complex and costly instruments can still provide satisfying solutions, despite the requirement of thrusting systems to compensate for the drag.

As far as the elliptical orbit is concerned, the degree-RMS plot is shown in Figure 22, whilst the degree strengths are listed in Table 7.

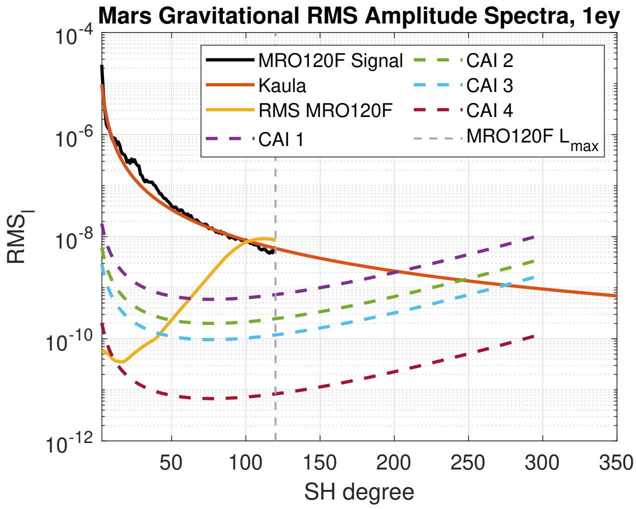

Fig. 22. Degree RMS plot for the elliptical orbit with periapsis and apoapsis equal to 100 and 1000 km, respectively.

The degree strength for CAI 4 was found by extrapolating the respective dashed curve with a 4^{th} degree polynomial and corresponded to 372.

Table 7. Degree strength for elliptical orbit with different CAI configurations.

CAI	Degree Strength
1	199
2	243
3	273
4	372

At degree 100, whereby MRO120F has a SNR of 1, the SNR is as high as 10^3 for CAI 4, given the flat and low error curves in Figure 22.

Furthermore, due to the very low periapsis, the spacecraft should be equipped with thrusters to be fired only during a small portion of the orbit, as discussed in subsection 3.3.

The study of the temporal variation of the gravity field led to the same conclusions drawn for MRO's PSO (see subsection 5.2): one-year of CAI-based gradiometry mission is not suitable to resolve time-varying gravity signatures.

For the very low and elliptical orbits, the degree strength map could not be retrieved due to the high computational effort required to study the degree strengths up to about 400.

To conclude, any of the considered missions with the opportune CAI configuration would entail moderate to great improvements of the gravity field model MRO120F, with only one year of observations.

5.4. Spatial Resolution

A summary of the missions whose degree strengths exceed 120 (MRO120F's maximum degree and order) is furnished in Table 8. In this table, also the achievable spatial resolution is listed. Approximately, an indication for the spatial resolution (on ground) is represented by the wavelength λ. For a given spherical harmonic degree l, it can be approximated as

$$\lambda = \frac{2\pi R}{l + 1/2}, \tag{22}$$

where R is the planetary radius.

Table 8. Combination of orbital altitudes and CAI configurations which would lead to a mission return outperforming the current models.

Orbit	CAI	Degree Strength	Spatial Resolution
MRO PSO	4	139	153 km
h_0=232 km	3	130	163 km
	4	173	123 km
h_0=240 km	4	172	123 km
h_0=250 km	4	153	139 km
h_0=150 km with DFCS	1	151	141 km
	2	178	119 km
	3	196	108 km
	4	265	80 km
h_0=133 km with DFCS	1	165	129 km
	2	194	109 km
	3	209	113 km
	4	295	72 km
h_0=100 km with DFCS	1	227	94 km
	2	266	80 km
	3	294	72 km
	4	390	55 km
Elliptical Orbit (100x1000 km)	1	199	107 km
	2	243	87 km
	3	273	78 km
	4	373	57 km

As predicted by the degree strengths, these spatial resolutions are exceptional and can lead to the exploration of different-scale phenomena, as it will be extensively explained in subsection 5.5.

Furthermore, the CAI measurements represent an average along the orbit over the integration time. Thus, instrument-limited spatial resolution is calculated with the integration time multiplied by the orbital velocity. For CAI 4 the experiment time is 11 seconds, thus for the very-low circular orbits and the elliptical orbit at its perigee, the binding spatial resolution is down to about 38 km. Given that the resolutions from Table 8 are coarser than this value, the latter is not limiting, yet.

Additionally, in all of the degree-RMS plots, it is worth noticing that the gradiometry curves are relatively flat, implying that the errors grow rather slowly with increasing spatial resolution.

The development of space-borne platforms is nearly recent and still needs more advancements. Nevertheless, this work has unquestionably demonstrated their viability for space-based scientific and technological endeavours (Belenchia et al. (2022)), as discussed hereafter.

5.5. Scientific Return

The results that were discussed in all of the section 5 yield a significant improvement on the current state-of-the-art gravity field models and would be sufficient to answer the scientific questions presented in the introduction.

According to the spatial resolution, three groups of geological features to be explored are discussed, associated with the respectively fruitful missions analysed in this work.

- At a global and regional scale (λ > 1000 km - degree of 20 or lower) the crust and the lithosphere, together with the thermal evolution of Mars can be studied with all of the missions listed in Table 8. These features have been already studied by processing the data of the Mars Exploration Program orbiters, yet gradiometry would improve the uncertainty of the current models. As a matter of fact, gravity gradients are extremely useful in investigating the crust of a planet: the latter mirrors information on the differentiation processes and magmatic evolution of the planetary surface, linked to the planet's formation, evolution and thermal nature. The current geophysical models of Mars are based on the spherical thin elastic shell approximation (Goossens et al. (2017)). Low long-wavelength uncertainties facilitated by a CAI mission would improve the observational constraints for such a mission and help evaluate the validity of this assumption.
- At local scales (100 km< λ < 1000 km - degrees up to 200), all of these missions can help explore several geological features, visible in the topography map of Mars (Figure 23).

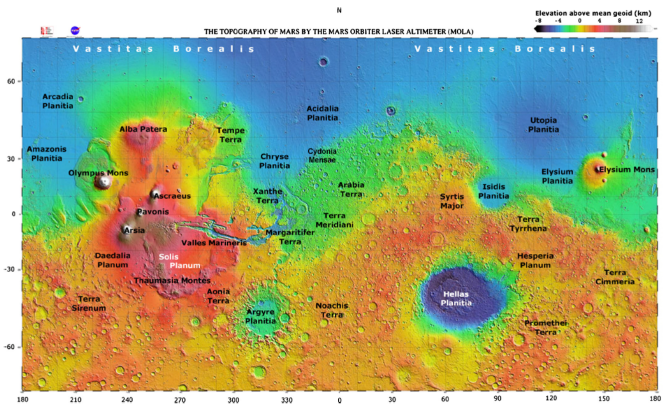

Fig. 23. Geographical description of major topographic features on Mars (Rodrigue (2007)).

First and foremost, the Martian hemispheric dichotomy is of great interest: northern and southern hemispheres differ in elevation, geology, macro-scale roughness and cratering age. There are ancient, high-standing cratered terrains in the south whilst smooth, thinner, sparsely cratered, young lowlands in the north, where impact basins have a thin deposits veneer on top (Genova (2020),Frey et al. (2002),Smith et al. (2001)). This dichotomy only partially coincides with a crustal thickness variation between the northern and southern hemispheres (Goossens et al. (2017)). In fact, two crustal thickness zones can be individuated: a region of thicker crust that thins progressively from the south toward the north comprising much of the southern highlands and Tharsis; a uniform thinner thickness in northern lowlands and Arabia Terra (Smith et al. (2001)).

Furthermore, the crustal density generally increases with depth, but higher precision models, which could be constrained better by a CAI mission, are required to resolve the density and density gradients. In fact, there are lower crustal density zones allegedly due to porosity obtained through impact cratering (Goossens et al. (2017)).

As demonstrated in Tenzer et al. (2015), also the sub-crustal stress field can be extrapolated by gravity data, but the current model (Figure 24) has a degree strength of 85.

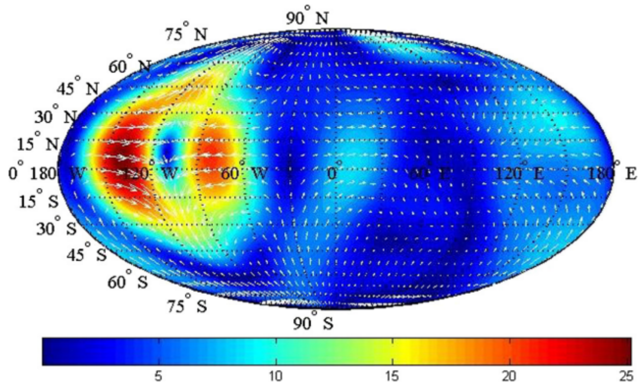

Fig. 24. Long-wavelength part of the Martian sub-crustal stress field: The horizontal stress vectors and their intensity (in MPa) (Tenzer et al. (2015)).

These gradiometry missions would undoubtedly help outperform the current model. In this, as visible in the figure above, most of the stress is in the Tharsis region, in correspondence to the Olympus Mount. The latter's origin is hypothetically of volcanic construction or historical uplift with further modelling. There is a negative gravity ring around the Tharsis that indicates large horizontal spatial gravity variations that require further studies. Elsewhere, the stress intensity is smaller or absent. There are slightly enhanced contours of the 4 major impact basins (Isidis, Hellas, Argyre and Utopia): this may be due to the crustal extrusion after impact and subsequent Moho uplift, yielding a maximum horizontal stress around the impact craters. This gives a clue that the aforementioned geological features are not full isostatically compensated. Additionally, gradiometry may help constrain the nature of Valles Marineris by studying the local stress distribution which can be explained by regional tectonism related to the crustal load of the Tharsis bulge. Finally, in that region there are no signatures of hemispheric dichotomy or crustal load due to polar ice, making the Valles interesting to study (Tenzer et al. (2015)).

Furthermore, northern lowlands are equipotential surfaces and putative sites of an early ocean. As a matter of fact, they show enhanced topographic smoothness and distinctive, simple crater properties. On top of this, the volume is consistent with the estimate of the amount of water thought to be once available on Mars. The controversies that gravity gradients may help resolve are the absence of paleoshorelines, the lack of tectonic ridge-like morphology of the potential shorelines and the unavailability of superficial carbonates (Smith et al. (2001)).

- Only the very-low and the elliptical orbits, like no other gravity measurements done in space, can also be used to investigate geological features and phenomena at even smaller scales ($\lambda < 100$ km - degrees larger than 200), such as smaller impact craters, near-surface magmatism, deformation, polar volatiles and so on. These missions may help investigate the nature of the four impact drainage basins:
  - Hellas structure is the deepest of the solar system with a relief of 9 km. It has ejecta of 2 km and is asymmetric because its origin was an oblique impact with further localized surface modification;
  - Utopia is buried beneath the northern plains and it is only 2.5 km deep;
  - Argyre was a large drainage basin in the highlands;
  - Isidis basin has no counterpart in images and displays a complex floor structure, lying at the dichotomy boundary.

  Furtermore, there are regional slopes deemed to be early water channels as the result of water flow rate and discharge. The buried channels, with depths varying with latitude, were proposed to be filling the early ocean (Smith et al. (2001)).
  CAI-based gradiometry can also enhance the study of polar caps.
  - North cap. It stands 3 km above the surroundings that are in a 5 km depression (northern lowlands). It has a complex structure comprising chasms and sinks for wind-blown dust. According to the current models, gravity anomalies do not correlate well with the northern polar deposits, meaning that the cap is either nearly isostatically compensated or there is a complex subsurface structure.
  - South cap. It is much smaller than the northern and it has a well-defined gravity anomaly correlated with the southern layered terrains. Thus, these are uncompensated(Smith et al. (2001)).

Other features that can be studied with ths very-low and elliptical missions are the Quasi-Circular Depressions (QCD): these are roughly circular and bowl-like-shaped buried impact basins with a widespread distribution in both lowlands and highlands. The softened profiles testify an intense early bombardment and subsequent active resurfacing (Frey et al. (2002)). Most of the QCD were detected by altimetry elevation data by the Mars Orbiter Laser Altimeter (MOLA) and not by imagery, thus enhanced gravity models may be an asset. These are thought to have been low and stable for most of the history, indicating that highland-lowland crustal dichotomy is primordial and was established soon after planetary accretions.

5.6. Bouguer Anomaly

Another study that can be conducted with gradiometry (and topography) data is the Bouguer analysis. To this end, the static gravitational potential can be conceived as the sum of different contributions:

$$U = U_{\mathrm{crust}} + U_{\mathrm{local}} + U_{\mathrm{core}} + U_{\mathrm{mantle}} \tag{23}$$

where U_{local} represents the isolated crustal density anomalies in an otherwise homogeneous crust. Thus, the Bouguer potential is defined as $U - U_{\mathrm{crust}}$ and the Bouguer anomaly is the difference between the expected and actual gravity at a certain location. Depressed basins such as Utopia, Hellas and Isidis have strong positive circular anomalies. Thus, there are uncompensated Bouguer mass excesses that arose from Moho uplift following an early impact and subsequent volcanic and sedimentary resurfacing. There are other smaller positive anomalies such as at Ares Vallis and Amazonis. This probably resulted from early impacts but the features do not have a circular shape. There are other enigmatic positive anomalies not associated with topographic or geological features in the northern circumpolar lowlands. Leveraging the high sensitivity to medium-to-short wavelengths, CAI-based gradiometry may help study these features with unprecedented accuracy. For instance, Kasei Valles, Coprates and Eos Chasma show substantial positive anomalies, suggesting a shallower mantle or crustal intrusions; Ius and Capri Chasma do not have positive anomalies although expected. This is probably due to the limited spatial resolution of the gravity models, thus gradiometry missions are needed. Finally, mounts such as Tharsis and Elysium have strong negative anomalies, meaning that the geological features are isostatically compensated (Goossens et al. (2017)).

6. Conclusions and Outlook

Insufficient knowledge of the global gravity field of Mars represents, nowadays, the weak link in the development of a global integrated geodetic/geodynamic observing system, which comprises three components (Rummel et al. (2002); Cesare et al. (2016)):

- geometry and surface deformation;
- the planetary rotation;
- the planet's gravity field.

Hence, dedicated satellite gravity field missions would be well timed and justified in the context of the current scientific scenario, considering the potential advances that they could provide (Rummel et al. (2002)).

During this work, we devised innovative mission designs, leveraging cutting-edge CAI-based gradiometers as the scientific payload of spacecraft orbiting Mars. The aim of these missions is to acquire observations of the Martian gravity field with accuracy and spatial resolution surpassing those already attained via previously successful missions, which led to the development of the latest and most accurate gravity model, MRO120F. We demonstrated that CAI-based gradiometry holds the promise to be enabling the retrieval of high-resolution gravity field models which can be exploited to investigate diverse geophysical phenomena.

First of all, we explored conceptual and instrumental facets of cold atom interferometers for dedicated gravity gradiometry missions. We selected four different instrument configurations, with increasing sensitivity (CAI 1 to CAI 4) to study the impact on the mission's scientific return. The missions taken into account were divided into four different groups: (1) MRO's Primary Science Orbit, (2) low circular and polar orbits without a DFCS (orbital altitude 232, 240 and 250 km), (3) very-low circular and polar orbits with a DFCS (orbital altitude 100, 133 and 150 km) and (4) an elliptical polar orbit with the periapsis at 100 km and the apoapsis at 1000 km. We envisaged a spacecraft lifetime of 1 Earth year or 1 Martian year (only for the MRO's PSO case).

According to a covariance-based analysis, as far as the first two orbit concepts are concerned, CAI 4, the most sensitive -

thus the most complex and expensive -, must be used to achieve a degree strength superior to the latest model's one (120). Albeit the promising results, we think that the requirement of the most costly CAI together with a maximum degree below 173 are not such to promote these dedicated gravity gradiometry missions. On the other hand, we would recommend installing a CAI-based gradiometer as a secondary payload to a potential (gravity reconnaissance) spacecraft with similar orbit geometries, as an added asset.

About the other two orbit groups, the spacecraft fly closer to the planetary surface. As the gravitational field signals exponentially decrease by a factor $R/(R+h)^l$ with increasing altitude h and and SH degree l (Zheng and Li (2018)), the lower the orbital altitude is, the better the potential scientific return of the mission. Therefore, for mission groups 3 and 4, the gravity signal is stronger and any of the CAI configurations, also the least sensitive, can be exploited to retrieve very high-resolution models. We envisage that these are the most promising results, as less complex instruments can be employed and still obtain very high degree strengths, larger than 150. Yet, the best solution is attainable at 100 km, whereby, after 1 year of mission, a degree strength of 390 can be achieved with CAI 4. Nevertheless, this mission concept requires demanding propulsion system to maintain the orbit. Simpler thruster solutions (ion engines) can be employed for the other two very-low orbits (h_0 = 133 and 150 km). A mission with the CAI 4 instrument at an altitude of 133 km (150 km) would be disruptive since it would triple (more than double) the spatial resolution compared to current models. Hence, we advise to further the development of such missions to largely advance the field of gravity model recovery, provided the availability of thrusting systems for orbit maintenance.

The communion of such a short mission lifetime with these exceptional results would revolutionize the field of gravity reconnaissance and lead to a great improvement of the study of the surface and subsurface of Mars. As a matter of fact, we noticed that all of these selected missions (orbit groups 1 and 2 with CAI 4 and orbit concepts 3 and 4 with all CAI configurations) are suitable to study global- and regional/local-scale geophysical features. In detail, the crustal density and thickness of Mars may be investigated, together with the correlation between the crustal structure and the hemispheric dichotomy. The crustal porosity might also be interrogated as a parameter that may play a role in the determination of crustal properties. Similarly, how the elastic thickness flexes under the loads might be retrieved. Additionally, the data provided by these missions may be post-processed to explore the sub-crustal stress and to fetch models more accurate and with higher spatial resolution than the current one, which displays a maximum degree of only 85. Other features that may be studied are QCD, which were only detected via altimetry and not by imagery. In this regard, we recommend considering an altimeter onboard the orbiter to pair topography observations to gravity gradient data, although Mars Orbiter Laser Altimeter (MOLA) had already provided a lot of useful data. Furthermore, we found that mission groups 3 and 4 can provide spatial resolutions much higher (below 100 km), making it feasible to study small impact craters, near-surface magmatism, deformation, polar volatiles, polar caps and so on.

It is worth reminding that in this work single-axis gradiometers were considered, yet multi-axis configurations may be contemplated in further studies to extrapolate information on all of the gravity-gradient tensor components and enhance the gravity field resolution even more.

On top of this, we concluded that 1-year gradiometry missions would only bring benefits to the static gravity field survey, whilst radio science or ll-SST would still be better to constrain the time-varying gravity signatures. Notwithstanding, we expect CAI-based gradiometry to hold the promise to also help interrogate time-varying SH coefficients with longer missions, but this is beyond the scope of this work and we leave these aspects for future studies.

Finally, we think the time is ripe for the communion between cold atom interferometry and space science, as also testified by the calls for new proposals at the American, European and Chinese space agencies, where there is an increasing interest in space-borne quantum sensing. In the coming decades, we envisage the miniaturization of the devices and an improvement of their TRL to make missions like the ones introduced in this work feasible.

With these disrupting results, the methodology described in this work was intended to mark the foothold to contemplate the potential of CAI-based gradiometry in furthering the geodesic review of future dedicated gravity missions to the solar system's planets.

References

Abend, S. (2017). *Atom-chip gravimeter with Bose-Einstein Condensates*. PhD thesis, Leibniz University, Hannover.

Abrykosov, P., Pail, R., Gruber, T., Zahzam, N., Bresson, A., Hardy, E., Christophe, B., Bidel, Y., Carraz, O., and Siemes, C. (2019). Impact of a novel hybrid accelerometer on satellite gravimetry performance. *Advances in Space Research*, 63(10):3235 – 3248.

Almeida, N., Werlang, T., and Valente, D. (2019). Mach–Zehnder interferometer with quantum beamsplitters. *Journal of the Optical Society of America B*, 36(12):3357–3363.

Anderson, M. H., Ensher, J. R., Matthews, M. R., Wieman, C. E., and Cornell, E. A. (1995). Observation of Bose-Einstein Condensation in a Dilute Atomic Vapor. *Science*, 269(5221):198–201.

Asmar, S. W., Konopliv, A. S., Watkins, M. M., Williams, J. G., Park, R. S., Kruizinga, G. L., Paik, M., Yuan, D., Fahnestock, E. G., Strekalov, D., Harvey, N., Lu, W., Kahan, D. S., Oudrhiri, K., Smith, D. E., and Zuber, M. T. (2013). The Scientific Measurement System of the Gravity Recovery and Interior Laboratory (GRAIL) Mission. *Space Science Reviews*, 178:25–55.

Aveline, D. C. et al. (2020). Observation of Bose–Einstein condensates in an Earth-orbiting research lab. *Nature*, 582(7811):193–197.

Badami, M. A. (2019). *Design of a FEEP Thruster for Micro-/Nano-Satellites*. PhD thesis, Luleå University of Technology Department of Computer Science, Electrical and Space Engineering.

Baur, O., Austen, G., and Keller, W. (2007). *Efficient Satellite Based Geopotential Recovery*, pages 499–514.

Baur, O., Austen, G., and Kusche, J. (2008). Efficient GOCE satellite gravity field recovery based on least-squares using QR decomposition. *Journal of Geodesy*, 82:207–221.

Becker, D., Lachmann, M. D., Seidel, S. T., Ahlers, H., Dinkelaker, A. N., Grosse, J., Hellmig, O., Müntinga, H., Schkolnik, V., Wendrich, T., Wenzlawski, A., Weps, B., Corgier, R., Franz, T., Gaaloul, N., Herr, W., Lüdtke, D., Popp, M., Amri, S., Duncker, H., Erbe, M., Kohfeldt, A., Kubelka-Lange, A., Braxmaier, C., Charron, E., Ertmer, W., Krutzik, M., Lämmerzahl, C., Peters, A., Schleich, W. P., Sengstock, K., Walser, R., Wicht, A., Windpassinger, P., and Rasel, E. M. (2018). Space-borne Bose–Einstein condensation for precision interferometry. *Nature*, 562(7727):391–395.

Belenchia, A., Carlesso, M., Ömer Bayraktar, Dequal, D., Derkach, I., Gasbarri, G., Herr, W., Li, Y. L., Rademacher, M., Sidhu, J., Oi, D. K., Seidel, S. T., Kaltenbaek, R., Marquardt, C., Ulbricht, H., Usenko, V. C., Wörner, L., Xuereb, A., Paternostro, M., and Bassi, A. (2022). Quantum physics in space. *Physics Reports*, 951:1–70.

Belleguic, V., Lognonné, P., and Wieczorek, M. (2005). Constraints on the martian lithosphere from gravity and topography data. *Journal of Geophysical Research*, 110:E11005.

Bills, B. G. and Ermakov, A. I. (2019). Simple models of error spectra for planetary gravitational potentials as obtained from a variety of measurement configurations. *Planetary and Space Science*, 179:104744.

Borderies, N. and Longaretti, P.-Y. (1990). A New Treatment of the Albedo Radiation Pressure in the Case of a Uniform Albedo and of a Spherical Satellite. *Celestial Mechanics and Dynamical Astronomy*, 49(1):69–98.

Branigan, T. L. (1965). Mariner 4: Mission to Mars. *The Physics Teacher*, 3(7):303–307.

Cadoret, M., Mirandes, E., Cladé, P., Guellati-Khelifa, S., Schwob, C., Nez, F., Julien, L., and Biraben, F. (2009). Combination of Bloch Oscillations with a Ramsey-Borde Interferometer: New Determination of the Fine Structure Constant. *Physical review letters*, 101:230801.

CAI-TN4 (2019). Study of a CAI Gravity Gradiometer Sensor and Mission Concepts, Roadmap and alternative mission scenarios. ESA Contract No. 4000112677/14/NL/MP.

Carraz, O., Siemes, C., Massotti, L., Haagmans, R., and Silvestrin, P. (2014). A Spaceborne Gravity Gradiometer Concept Based on Cold Atom Interferometers for Measuring Earth's Gravity Field. *Microgravity Science and Technology*, 26.

Carraz, O., Siemes, C., Massotti, L., Haagmans, R., and Silvestrin, P. (2015). Measuring the Earth's gravity field with cold atom interferometers. *Atomic Physics*, (arXiv:1506.03989 [physics.atom-ph]).

Cesare, S., Allasio, A., Anselmi, A., Dionisio, S., Mottini, S., Parisch, M., Massotti, L., and Silvestrin, P. (2016). The european way to gravimetry: From goce to nggm. *Advances in Space Research*, 57(4):1047–1064.

Council, N. R. (1997). *Satellite Gravity and the Geosphere: Contributions to the Study of the Solid Earth and Its Fluid Envelopes*. The National Academies Press, Washington, DC.

Dickerson, S. M., Hogan, J. M., Sugarbaker, A., Johnson, D. M. S., and Kasevich, M. A. (2013). Multiaxis inertial sensing with long-time point source atom interferometry. *Physical Review Letters*, 111:083001.

Douch, K., Hu, W., Schubert, C., Müller, J., and Pereira dos Santos, F. (2017). Simulation-based evaluation of a cold atom interferometry gradiometer concept for gravity field recovery. *Advances in Space Research*, 61.

Eshagh, M. and Tenzer, R. (2015). Sub-crustal stress determined using gravity and crust structure models. *Computational Geosciences*, 19:115–125.

Floberghagen, R., Fehringer, M., Lamarre, D., Muzi, D., Frommknecht, B., Steiger, C., Piñeiro, J., and da Costa, A. (2011). Mission design, operation and exploitation of the gravity field and steady-state ocean circulation explorer mission. *Journal of Geodesy*, 85(11):749–758.

Folkner, W. M., Williams, J. G., Boggs, D. H., Park, R. S., and Kuchynka, P. (2014). The Planetary and Lunar Ephemerides DE430 and DE431. *Interplanetary Network Progress Report*, 42-196:1–81.

Frey, H. V., Roark, J. H., Shockey, K. M., Frey, E. L., and Sakimoto, S. E. H. (2002). Ancient lowlands on Mars. *Geophysical Research Letters*, 29(10):22–1–22–4.

Gauguet, A., Mehlstäubler, T. E., Lévèque, T., Le Gouët, J., Chaibi, W., Canuel, B., Clairon, A., Dos Santos, F. P., and Landragin, A. (2008). Off-resonant raman transition impact in an atom interferometer. *Physical Review A*, 78(4).

Geiger, R., Landragin, A., Merlet, S., and Pereira Dos Santos, F. (2020). High-accuracy inertial measurements with cold-atom sensors. *AVS Quantum Science*, 2(2):024702.

Genova, A. (2020). ORACLE: A mission concept to study Mars' climate, surface and interior. *Acta Astronautica*, 166:317–329.

Genova, A., Goossens, S., Lemoine, F. G., Mazarico, E., Fricke, S. K., Smith, D. E., and Zuber, M. T. (2015). Long-term variability of CO2 and O in the Mars upper atmosphere from MRO radio science data. *Journal of Geophysical Research: Planets*, 120(5):849–868.

Genova, A., Goossens, S., Lemoine, F. G., Mazarico, E., Neumann, G. A., Smith, D. E., and Zuber, M. T. (2016). Seasonal and static gravity field of Mars from MGS, Mars Odyssey and MRO radio science. *Icarus*, 272:228 – 245.

Goossens, S., Sabaka, T. J., Genova, A., Mazarico, E., Nicholas, J. B., and Neumann, G. A. (2017). Evidence for a low bulk crustal density for mars from gravity and topography. *Geophysical Research Letters*, 44(15):7686–7694.

Greeley, R. (2001). Science Planning for Exploring Mars, Part 2, Scientific Goals, Objectives, Investigations, and Priorities. *Jet Propulsion Laboratory Publications*, 01(7). JPL, California Institute of Technology, Pasadena, California.

Gross, C. (2012). Spin squeezing, entanglement and quantum metrology with Bose–Einstein condensates. *Journal of Physics B*, 45:103001.

Heiskanen, W. A. and Moritz, H. (1967). *Physical geodesy*. W. H. Freeman and Company, San Francisco.

Johnston, D., Graf, J., Zurek, R., Eisen, H., and Jai, B. (2003). The Mars Reconnaissance Orbiter Mission.

Karatekin, , Duron, J., Rosenblatt, P., Van Hoolst, T., Dehant, V., and Barriot, J.-P. (2005). Mars' time-variable gravity and its determination: Simulated geodesy experiments. *Journal of Geophysical Research*, 110, E6.

Kaula, W. (2013). *Theory of Satellite Geodesy: Applications of Satellites to Geodesy*. Dover Earth Science. Dover Publications.

Konopliv, A. S., Asmar, S. W., Folkner, W. M., Özgür Karatekin, Nunes, D. C., Smrekar, S. E., Yoder, C. F., and Zuber, M. T. (2011). Mars high resolution gravity fields from mro, mars seasonal gravity, and other dynamical parameters. *Icarus*, 211(1):401–428.

Konopliv, A. S., Park, R. S., and Folkner, W. M. (2016). An improved JPL Mars gravity field and orientation from Mars orbiter and lander tracking data. *Icarus*, 274:253–260.

Konopliv, A. S., Park, R. S., Rivoldini, A., Baland, R.-M., Le Maistre, S., Van Hoolst, T., Yseboodt, M., and Dehant, V. (2020). Detection of the Chandler Wobble of Mars From Orbiting Spacecraft. *Geophysical Research Letters*, 47(21):e2020GL090568.

Lemoine, F., Goossens, S., Sabaka, T., Nicholas, J., Mazarico, E., Rowlands, D., Loomis, B., Chinn, D., Neumann, G., Smith, D., and Zuber, M. (2014). Grgm900c: A degree-900 lunar gravity model from grail primary and extended mission data. *Geophysical Research Letters*, 41.

Lemoine, F. G., Smith, D. E., Rowlands, D. D., Zuber, M. T., Neumann, G. A., Chinn, D. S., and Pavlis, D. E. (2001). An improved solution of the gravity field of Mars (GMM-2B) from Mars Global Surveyor. *Journal of Geophysical Research: Planets*, 106(E10):23359–23376.

Leomanni, M., Garulli, A., Giannitrapani, A., and Scortecci, F. (2017). Propulsion options for very low Earth orbit microsatellites. *Acta Astronautica*, 133:444–454.

Li, X., LeMoine, F., Paik, H. J., Zagarola, M. V., Shirron, P., Griggs, C. E., Moody, M. V., and Han, S. (2016). Design of superconducting gravity gradiometer cryogenic system for mars mission. International Cryocooler Conference, Inc., Boulder, Colorado.

Liu, X. (2008). Global gravity field recovery from satellite-to-satellite tracking data with the acceleration approach. 68. Dissertation, Delft University of Technology.

Lockney, D. (2010). Mars Global Reference Atmospheric Model 2010 (Mars GRAM 2010). https://software.nasa.gov/software/MFS-33158-1. License obtained on 04/02/2021.

Malossi, N., Bodart, Q., Merlet, S., Landragin, A., and Pereira dos Santos, F. (2009). Double diffraction in an atomic gravimeter. *Physical Review A*, 81.

Marty, J., Balmino, G., Duron, J., Rosenblatt, P., Le Maistre, S., Rivoldini, A., Dehant, V., and Van Hoolst, T. (2009). Martian gravity field model and its time variations from MGS and Odyssey data. *Planetary and Space Science*, 57(3):350–363.

Mazarico, E., Genova, A., Goossens, S., Lemoine, F. G., Neumann, G. A., Zuber, M. T., Smith, D. E., and Solomon, S. C. (2014a). The gravity field, orientation, and ephemeris of Mercury from MESSENGER observations after three years in orbit. *Journal of Geophysical Research: Planets*, 119(12):2417–2436.

Mazarico, E., Genova, A., Goossens, S., Lemoine, F. G., Neumann, G. A., Zuber, M. T., Smith, D. E., and Solomon, S. C. (2014b). The gravity field, orientation, and ephemeris of Mercury from MESSENGER observations after three years in orbit. *Journal of Geophysical Research: Planets*, 119(12):2417–2436.

Mazarico, E., Zuber, M. T., Lemoine, F. G., and Smith, D. E. (2009). Effects of Self-Shadowing on Nonconservative Force Modeling for Mars-Orbiting Spacecraft. *Journal of Spacecraft and Rockets*, 46(3):662–669.

Menon, P., Wagner, S., and Demcak, S. (2017). 50,000 Laps Around Mars: Navigating the Mars Reconnaissance Orbiter Through the Extended Missions (January 2009 - March 2017). *International Symposium on Space Flight Dynamics, Matsuyama, Japan*.

Migliaccio, F., Reguzzoni, M., Batsukh, K., Tino, G., Rosi, G., Sorrentino, F., Braitenberg, C., Pivetta, T., Barbolla, D., and Zoffoli, S. (2019). MOCASS: A Satellite Mission Concept Using Cold Atom Interferometry for Measuring the Earth Gravity Field. *Surveys in Geophysics*, 40:1029–1053.

Müller, F., Carraz, O., Visser, P., and Witasse, O. (2020). Cold atom gravimetry for planetary missions. *Planetary and Space Science*, 194:105110.

Neumann, G., Zuber, M., Wieczorek, M., Mcgovern, P., Lemoine, F., and Smith, D. (2004). Crustal structure of mars from gravity and topography. *J. Geophys. Res*, 5714.

Pail, R. (2015). *It's All About Statistics: Global Gravity Field Modeling from GOCE and Complementary Data*, pages 2345–2372. Springer Berlin Heidelberg, Berlin, Heidelberg.

Peters, A., Chung, K., and Chu, S. (2003). High-precision gravity measurements using atom-interferometry. *Metrologia*, 38:25.

Randall, P., Lewis, R., Clark, S., and Hall, K. (2019). T5 performance, industrialisation and future applications. Presented at the 36th International Electric Propulsion Conference, University of Vienna, Austria September 15-20.

Rodrigue, C. M. (2007). The topography map of Mars, Geography. California State University Long Beach. `http://www.csulb.edu/~rodrigue/mars/MOLAmercatorlabel.jpg`. Last accessed: on 20/10/2022.

Rummel, R., Balmino, G., Johannessen, J., Visser, P., and Woodworth, P. (2002). Dedicated gravity field missions—principles and aims. *Journal of Geodynamics*, 33(1):3 – 20. Earth's Gravity and Magnetic Fields from Space.

Sansò, F. and Migliaccio, F. (2020). *Quantum Measurement of Gravity for Geodesists and Geophysicists*. Springer Cham.

Schuh, W. (1996). *Tailored Numerical Solution Strategies for the Global Determination of the Earth's Gravity Field: Study of the Complementary Use of the Gradiometry and Global Positioning System (GPS) for the Determination of the Earth's Gravity Field ; Technical Report*. Mitteilungen der Geodätischen Institute der Technischen Universität Graz. Technischen Universität Graz, Institute für Theoret. Geodäsie.

Schuldt, T., Schubert, C., Krutzik, M., Bote, L. G., Gaaloul, N., Hartwig, J., Ahlers, H., Herr, W., Posso-Trujillo, K., Rudolph, J., and et al. (2015). Design of a dual species atom interferometer for space. *Experimental Astronomy*, 39(2):167–206.

Semenov, B. and Baalke, R. (2022). NASA's Navigation and Ancillary Information Facility (NAIF). `https://naif.jpl.nasa.gov/naif/documentation.html`. Last accessed: on 15/07/2022.

Siemes, C. (2008). *Digital Filtering Algorithms for Decorrelation Within Large Least Squares Problems*. PhD thesis, University of Bonn, Germany.

Siemes, C. (2018). GOCE Level 1B Gravity Gradient Processing Algorithms. Technical report ESA-EOPSM-GOCE-TN-3397, Issue 1.0.

Siemes, C. et al. (2014). Evolution of GOCE gravity gradient performance during mission lifetime. Poster presented at the 5^{th} international GOCE user workshop for the European Space Agency, in Paris, France.

Smith, D., Zuber, M., Frey, H., Garvin, J., Head, J., Muhleman, D., Pettengill, G., Phillips, R., Solomon, S., Zwally, H., Banerdt, W., and Duxbury, T. (2001). Mars orbiter laser altimeter: Experiment summary after the first year of global mapping of mars. *Journal of Geophysical Research*, 106:23689–23722.

Smith, D. E., Zuber, M. T., Torrence, M. H., Dunn, P. J., Neumann, G. A., Lemoine, F. G., and Fricke, S. K. (2009). Time variations of Mars' gravitational field and seasonal changes in the masses of the polar ice caps. *Journal of Geophysical Research: Planets*, 114(E5).

Snyder, J., Goebel, D. M., Hofer, R. R., Polk, J. E., Wallace, N. C., and Simpson, H. (2012). Performance Evaluation of the T6 Ion Engine. *Journal of Propulsion and Power*, 28(2):371–379.

Sorrentino, F., Bodart, Q., Cacciapuoti, L., Lien, Y.-H., Prevedelli, M., Rosi, G., Salvi, L., and Tino, G. M. (2014). Sensitivity limits of a Raman atom interferometer as a gravity gradiometer. *Phys. Rev. A*, 89:023607.

Steiger, C., Mardle, N., and Emanuelli, P. P. (2014). Goce end-of-mission operations report. *European Space Agency*. GO-RP-ESC-FS-6268 (1), revision (0).

Stern, G., Battelier, B., Geiger, R., Varoquaux, G., Villing, A., Moron, F., Carraz, O., Zahzam, N., Bidel, Y., Chaibi, W., and et al. (2009). Light-pulse atom interferometry in microgravity. *The European Physical Journal D*, 53(3):353–357.

Tapley, B. D., Bettadpur, S., Ries, J. C., Thompson, P. F., and Watkins, M. M. (2004). GRACE Measurements of Mass Variability in the Earth System. *Science*, 305(5683):503–505.

Tenzer, R., Eshagh, M., and Jin, S. (2015). Martian sub-crustal stress from gravity and topographic models. *Earth and Planetary Science Letters*, 425:84–92.

Tino, G. and Kasevich, M. (2014). *Atom Interferometry: Proceedings of the International School of Physics "Enrico Fermi", Course 188, Varenna on Lake Como, Villa Monastero, 15-20 July 2013*. International School of Physics Enrico Fermi Series. IOS Press.

Tino, G., Sorrentino, F., Aguilera, D., et al. (2013). Precision gravity tests with atom interferometry in space. *Nuclear Physics B - Proceedings Supplements*, 243-244:203 – 217. Proceedings of the IV International Conference on Particle and Fundamental Physics in Space.

Torge, W. (2001). *Gravity Field of the Earth*, chapter 3, pages 45–90. Walter de Gruyter, Berlin.

Touboul, P. (2003). Microscope Instrument Development, Lessons for GOCE. *Space Science Reviews*, 108:393–408.

Trimeche, A., Battelier, B., Becker, D., and others. (2019). Concept study and preliminary design of a cold atom interferometer for space gravity gradiometry. *Classical and Quantum Gravity*, 36(21):215004.

van Gelderen, M. and Koop, R. (1997). The use of degree variances in satellite gradiometry. *Journal of Geodesy*, 71:337–343.

Visser, P. (1992). The use of satellites in gravity field determination and model adjustment. Phd dissertation, Delft University of Technology.

Ward, J. and Paul Byrne, P. (2022). The Geosciences Node of NASA's Planetary Data System (PDS). `https://pds-geosciences.wustl.edu/mro/mro-m-rss-5-sdp-v1/mrors_1xxx/data/shadr/`. Last accessed: on 15/07/2022.

Xu, C., Weigelt, M., Sideris, M., and Sneeuw, N. (2007a). Spaceborne gravimetry and gravity field recovery. *Canadian Aeronautics and Space Journal*, 53.

Xu, C., Weigelt, M., Sideris, M., and Sneeuw, N. (2007b). Spaceborne gravimetry and gravity field recovery. *Canadian Aeronautics and Space Journal*, 53.

Yi, W., Rummel, R., and Gruber, T. (2013). Gravity field contribution analysis of GOCE gravitational gradient components. *Studia Geophysica et Geodaetica*, 57.

Yu, N. N., Kohel, J. M., Romans, L. J., and Maleki, L. (2002). Quantum gravity gradiometer sensor for earth science applications. Earth Science Technology Conference Pasadena, California, USA.

Zheng, W. and Li, Z. (2018). Preferred design and error analysis for the future dedicated deep-space Mars-SST satellite gravity mission. *Astrophysics and Space Science*, 363(172).

Zuber, M. T., Smith, D. E., Lehman, D. H., Hoffman, T. L., Asmar, S. W., and Watkins, M. M. (2014). *Gravity Recovery and Interior Laboratory (GRAIL): Mapping the Lunar Interior from Crust to Core*, pages 3–24. Springer New York, New York, NY. In: Zuber, M.T., Russell, C.T. (eds) GRAIL: Mapping the Moon's Interior.

Zurek, R. W. and Smrekar, S. E. (2007). An overview of the Mars Reconnaissance Orbiter (MRO) science mission. *Journal of Geophysical Research: Planets*, 112(E5).

3

Conclusions and Recommendations

The present chapter draws upon the journal paper's findings to explicitly address the research sub-questions outlined in section 1.1 and to formulate recommendations for further works.

3.1. Conclusions

The answers to the research sub-questions hereby follow.

- **What are the best CAI gradiometer configurations that can be realistically selected as potential payload candidates?**

  Currently, there are no commercially available cold-atom inertial sensors constructed for space applications, but many prototypes have been conceived, some of which were successfully tested in microgravity, in a drop tower, and in a parabolic flight (Carraz et al. [4]). For this work, four different CAI configurations - CAI 1 to 4 - have been individuated, with increasing sensitivity, as delineated in Table 3.1.

Table 3.1: CAI 1 to 4 sensitivities to accelerations (Δa) and gravity gradients ($\Delta\gamma$) used for mission concept evaluation. The interferometer contrast is C > 0.6, which varies according to the satellite attitude and rotation compensation system, if any (Schuldt et al. [26]).

Gradiometer	$\Delta\gamma$ $[mE/\sqrt{Hz}]$	Δa $[m/s^2/\sqrt{Hz}]$	Sampling Interval [s]
CAI 1	308	1.1E-10	1.6
CAI 2	104	3.7E-11	1.66
CAI 3	50	1.8E-11	3
CAI 4	3.5	1.2E-12	11

These concepts were chosen amongst a list of feasible CAI configurations provided by Dr. O. Carraz in a personal correspondence. For comparison purposes, 4 different instruments were selected to understand the impact of the system's complexity (and, thus, costs) on the gravity field model resolution. As a matter of fact, higher sensitivity entails a more demanding physics package, one of the three units which a CAI-based sensor comprise (together with a laser system and an electronics unit). For each instrument configuration, the respective physics package's properties are collected in Table 3.2.

The differences between these configurations lie especially in the required atom temperature (and consequently cooling techniques) and the rotation compensation system. The former goes from μK to pK, requiring more and more advanced laser cooling strategies. Lower temperatures allow for reduced expansion rates, longer interrogation times, better control of atoms trajectory and less systematic effects due to the in-homogeneity of the beam splitter spatial profile, limited wave-front distortions and Coriolis accelerations (Trimeche et al. [34]). In light of the finite temperature of the atoms, these present a dispersion velocity, of the order of cm/s if the atoms are at μK

Table 3.2: CAI 1 - 4 physics package's properties (Müller et al. [23], Trimeche et al. [34]). The spacecraft accommodating the payload is considered in nadir-pointing configuration.

Physics Package System	CAI 1	CAI 2	CAI 3	CAI 4
Atom Cooling Temperature [K]	10^{-6}	10^{-6}	10^{-6}	10^{-9}
Cooling Technique	MOT + Optical Molasses	MOT + Optical Molasses	MOT + Optical Molasses	BEC
Number of Atoms [-]	10^{7}	$6{\cdot}10^{7}$	10^{8}	10^{6}
Interferometry Time [s]	0.3	0.33	0.5	5
Duty Cycle (reloading) Time [s]	1	1	2	1
Baseline [m]	0.5	0.5	0.5	0.5
Number of Photon Recoils [-]	2	2	2	2
Rotation Compensation System	-	Coarse (≈ 0.1mrad/s)	Fine ($\approx 1\mu$rad/s)	Fine ($\approx 1\mu$rad/s)

(MOT/molasses) and mm/s if atoms are at νK to pK (BEC). Due to this non-zero velocity, there is a Coriolis effect that involves rotation along the other-than-radial (measurements) axes. This entails loss of contrast, hence rotation compensation systems are required.

Due to the large computational effort of the simulations performed in this work, only single-axis gradiometers were exploited, as a scientific payload on board a nadir-pointing spacecraft, oriented such that it can sense only the zz component of the gravity tensor. In the assumed local frame, the z-component is in radial direction, whilst the x- and y- are in along- and cross-track directions, respectively. Another reason to use a single-axis gradiometer in radial direction is that the zz component has the highest contribution to the overall gravity field model solution (Yi et al. [37]).

- **Amongst the existing missions to Mars, which one is the most suitable as a baseline for a potential gradiometry mission to Mars?**

  In favour of other tasks, mission design is hereby avoided to bypass countless hours of undesired systems design. Therefore, the primary goal of this work was to identify a realistic baseline mission amongst the existing ones. A gravity reconnaissance mission requires strong and uniform signal sampling for homogeneous and global surface coverage of the observation data. In this regard, by looking at the missions of the Mars Exploration Program, the one providing the most suitable orbit is MRO in its Mapping orbit, or Primary Science Orbit (PSO), given its low-altitude, near-circular and quasi-polar orbit. The PSO lasted from November 2006 until December 2008 (Menon [21]). It was a frozen 250 x 315 km orbit, with duration of 112 minutes and an inclination of 92.65°, such that the spacecraft flew at approximately the same altitude whilst crossing each latitude circle. MRO had a daylight equatorial crossing, given an ascending node at 3:00 PM local mean solar time (Johnston et al. [14]). The periapsis was in correspondence of the South Pole, with an argument of periapsis of 270°. They did not choose a lower altitude because of the larger and larger atmospheric drag with descending altitude, which would have demanded frequent orbit maintenance manoeuvres. This would have required more fuel consumption but also hindered the quality of measurements (for instance, due to induced vibrations), which largely suffer from spurious accelerations. Finally, the orbit geometry envisaged a ground track repeat cycle of 17 days, guaranteeing the view of any surface point within a Martian season (Zurek and Smrekar [41]).

- **What are the possible orbit geometry modifications that would maximize the CAI mission scientific return?**

  The mission scientific return, in terms of accuracy of the recovered gravity field model, can be enhanced by adopting appropriate orbit geometries to satisfy the requirements of dedicated gravity reconnaissance missions. The latter are strong signal, as well as global, continuous and uniform coverage of the measurements. To achieve this, (very-)low and polar orbits are required. To this end, in addition to the MRO's PSO, other three groups of missions were explored: (1) low circular and polar orbits without the need for orbit maintenance, (2) very-low circular and polar orbits with a Drag-Free Control System (DFCS) and (3) an elliptical polar orbit.

About this first group, simulations on Tudat have revealed that 232 km is the lowest altitude which would sustain 1 Earth year of mission without thrusters for orbit maintenance. For comparison purposes, also 240- and 250-km orbits were explored. For the very-low orbits, average altitudes considered were 100 and 150 km. On top of this, an orbit at 133 km was also included, whose altitude represents the lowest for which ion thrusters are sufficient to trim the orbit. Finally, for completeness, a very elliptic polar orbit was also considered, with periapsis and apoapsis respectively at 100 and 1000 km, for which a DFCS is required when the spacecraft is closest to the surface of Mars. A spacecraft lifetime of 1 Earth year was envisaged.

- **What are the spherical harmonic degree and order, as well as the spatial resolution of the static and time-varying gravity field model of Mars, achievable by exploiting the selected instruments and missions?**

  In the framework of this study, the figure of merit to assess gravity field model precision is the so-called degree strength. This is the degree for which the Signal-to-Noise Ratio (SNR) reaches the unity. The latest and most accurate gravity field model, MRO120F, has maxima degree and order of 120 and a degree strength of 100. The degree strengths higher than this are achieved by the selected missions and instruments combinations summarised in Table 3.3. In this table, also the respective achievable spatial resolutions are listed.

Table 3.3: Combination of orbital altitudes and CAI configurations which would lead to a mission return outperforming the current models.

Orbit	CAI	Degree Strength	Spatial Resolution
MRO PSO	4	139	153 km
h_0=232 km	3	130	163 km
	4	173	123 km
h_0=240 km	4	172	123 km
h_0=250 km	4	153	139 km
h_0=150 km with DFCS	1	151	141 km
	2	178	119 km
	3	196	108 km
	4	265	80 km
h_0=133 km with DFCS	1	165	129 km
	2	194	109 km
	3	209	113 km
	4	295	72 km
h_0=100 km with DFCS	1	227	94 km
	2	266	80 km
	3	294	72 km
	4	390	55 km
Elliptical Orbit	1	199	107 km
(100x1000 km)	2	243	87 km
with DFCS	3	273	78 km
	4	373	57 km

For the missions with h_0 equals to 232, 240 and 250 km, only the CAI 4 would lead to improved solutions with respect to the current models. Notwithstanding, the enhancement is not such to endorse these missions. On the contrary, at very-low altitudes, albeit the requirement of a thrusting system, substantial improvements are attained also with less complex, hence cheaper, instruments. With simply an annual mission, very fine spatial resolutions can be achieved, disrupting the world of gravity field recovery of Mars.

Finally, according to the present study, 1-Earth-year gradiometry missions would only bring benefits to the static gravity field survey, whilst radio science or ll-SST would still be better to constrain the time-varying gravity signatures. These other methods' measurements are more sensitive to large-scale variations in the gravity field than gravity gradients because the large scale signals are less prominent in higher-order spatial derivatives. As a matter of fact, albeit the flat noise for almost the entire frequency spectrum, gradiometry is not very sensitive at long wavelengths since it observes the second derivative of the gravity potential. Notwithstanding, CAI-based gradiometry may putatively also contribute to interrogate time-varying SH coefficients with longer missions, but this is beyond the scope of this work and is left for future studies.

- **What are the scientific objectives that can be potentially addressed by these results?**

  Gravity gradients are extremely useful in studying the crust of a planet: the latter mirrors information on the differentiation processes and magmatic evolution of the planetary surface, linked to the planet's formation, evolution and thermal nature. Geophysical models of Mars are based on the spherical thin elastic shell approximation (Goossens et al. [10]).

  The geological features that can be studied are several. First and foremost, there is the Martian hemispheric dichotomy. According to this, northern and southern hemispheres differ in elevation, geology, macro-scale roughness and cratering age. We can find ancient, high-standing cratered terrains in the south whilst smooth, thinner, sparsely cratered, young lowlands in the north, where impact basins have thin deposits layer on top (Genova [9], Frey et al. [7], Smith et al. [31]). Notwithstanding, the dichotomy does not fully coincide with a crustal thickness variation between the northern and southern hemispheres (Goossens et al. [10]). In fact, two zones can be individuated: a region of thicker crust thickness that thins progressively from the south toward the north comprising much of the southern highlands and Tharsis; a uniform thinner thickness in northern lowlands and Arabia Terra (Smith et al. [31]).

  Furthermore, the crustal density generally increases with depth, but higher precision models are required to constrain density and density gradients. In fact, there are lower crustal density zones allegedly due to porosity obtained through impact cratering (Goossens et al. [10]).

  As demonstrated in Tenzer et al. [32], also the sub-crustal stress field can be extrapolated by gravity data, but the current models have a maximum SH resolution of degree 85. With the gradiometry missions individuated in this study, the current models could be largely enhanced.

  Leveraging these considerations, gradiometry in combination with altimetry data can be exploited to answer the following scientific questions:

  - what are the crustal density and thickness of Mars on a regional scale?
  - How does the crustal structure correlate with the hemispheric dichotomy (southern highlands, northern lowlands)?
  - What is the local sub-crustal stress of Mars? What are the major stress field features? What is the geological origin of these?
  - What is the crustal porosity? Does it play a role in the determination of the crustal density?
  - What are the mass excesses layered in proximity of the major basins and in the polar caps?
  - How does the elastic thickness flex under the studied loads?

3.2. Recommendations

Due to the substantial computational effort of the numerical strategies employed in the present thesis work, some analyses were left for future works. These points are outlined below.

- The core of the methodology exploited in this work is the covariance analysis. The latter has allowed surveying the formal errors of the SH coefficients. In future works, it is recommended to use the spacecraft states to build a design matrix and finally extrapolate the magnitude of the coefficients themselves, namely making a full estimated simulation. As the process requires high computational effort, tailored strategies, such as the preconditioned conjugate gradient algorithm, are endorsed. The solution can be paired with gravity-from-topography datasets to obtain information about the subsurface structure of Mars and address the scientific questions discussed in section 3.1. Alternatively, current models for the crustal density, the lithosphere thickness, the subcrustal stress and the like can furnish determining complementary data to study the correlation between gravity and topography. This would allow to explore geodesic features and infer whether they are isostatically compensated. Attention should be conveyed to current geophysical models, in order to understand whether the presently used spherical thin elastic shell approximation is valid. In this way, the tectonic differences between planets can be studied and information on the thermal nature of a body can follow, yielding clues of its formation and evolution.

- Once the least-square algorithm to retrieve the SH coefficients is set up, other parameters may be inserted into the list of unknowns. There are several parameters of interest. Amongst these, the tidal Love number k_2, the GM of Phobos and Deimos, and the orientation parameters, namely the Mars orientation epoch pole longitude, the obliquity, the Mars rotation rate, the seasonal corrections to spin, and the specular and diffuse corrections for spacecraft solar arrays (Konopliv et al. [15]). As gradiometry is less sensitive than RS at low SH degrees, other tracking measurements as well as data from landers may be combined to study these parameters. The latest estimates are presented in Konopliv et al. [16], as part of the MRO120F model. The aforementioned parameters constrain information on the rheology of the Martian mantle (Konopliv et al. [16]).

- In the present work, the formal errors of low-degree time-varying SH zonal coefficients have been investigated. A conclusion was drawn that 1 Earth year of gradiometry data could not outperform the solutions achieved based on 15 years of radio-science tracking. Confidently enough, longer missions could provide satisfying results in terms of temporal gravity field survey, exploring seasonal and secular changes. In particular, CAI-based gradiometry can furnish isotropic measurements of time-variable gravity, yielding an increase in the accuracy of the time-varying low-degree Stokes coefficients. This would allow mapping the intricate rotation function of the planet, such as modifications in length-of-the-day for modelling variations in Mars' inertia. Attention can be drawn to the seasonal and regional changes in snow deposits in polar areas; high-resolution mapping of polar scarps can enable to study the dynamics of ice sheets, identifying rock falls and avalanche events (Hussmann et al. [11]). As a consequence, it is recommended to investigate this potential in further studies.

- In this work, the selected instruments were single-axis gradiometers able to sense the radial component of the gravity gradient (U_{zz}). Nevertheless, the payload onboard GOCE had a diamond configuration of 3 sets of electrostatic accelerometers' pairs. Its purpose was to sense all the components of the gravity tensor. As a consequence, it is worth investigating the added value of using 3-axes CAI-based gradiometers. With specific configurations, CAI sensors can also measure the spacecraft rotation rate along the measurement axis. This is achievable by engineering two pairs of atom clouds in free-fall launched with opposite velocities (Carraz et al. [3]). The two pairs of clouds are spatially separated along a direction orthogonal to their velocities (Migliaccio et al. [22]).

- The very-low orbits considered in the present work, together with the elliptical orbit, must be equipped with a DFCS for maintaining the orbit and delaying the decay into the Martian atmosphere. A fast and approximate estimate of the ΔV has been provided; yet, more punctual and extensive studies are necessary to understand the manoeuvres required for orbit maintenance. Hence, the mission requirements in terms of thruster's type, number, configuration and power needed, as well as propellant mass must be outlined. In this fashion, an estimate of the mission costs can be performed.

A

Validation Strategies

A.1. Analytic covariance analysis

The methodology approached in this study comprises both an analytic and a numeric covariance analysis (Section 4.2.1 and 4.2.2, respectively). The former is adapted from the peer-reviewed paper by Bills and Ermakov [1]. Thus, the procedure is verified. The implementation of the analytic method in this work encompasses the transcription of equation 19, reported here:

$$\sigma_l^G = \left(\frac{\varepsilon_G}{\sqrt{N}}\right)\left(\frac{1}{n^2}\right)\left(\frac{r}{R}\right)^l \frac{1}{(l+1)(l+2)}. \tag{A.1}$$

into a MATLAB script, developed to retrieve the error spectra of the SH coefficients per degree. The formula required ε_G, the root sum square (RSS) of the measurement errors expected in a specific mission concept: in place of this, the different instrument sensitivities to gravity gradients (Table 3.1) have been manually inserted. The number of measurements N and the mean motion n were coded as, respectively, the mission period over the instrument integration time (T/T_{cycle}), and the square root of the Martian gravitational parameter over the cube of the spacecraft radius (planet's radius plus altitude, under the assumption of a circular orbit), namely $\sqrt{GM/(R+h)^3}$. The transcription of these equations has been verified by manual inspection and by running unit tests. Finally, integration tests followed by visual inspection. All of these were successful.

On top of this, in this work, a validation was performed. The validation strategy for the numerical approach follows in section A.3. The formal errors from the analytic approach and the latest gravity field model (MRO120F) are compared in Figure A.1: the majority of the ratios tends to the unity, yielding a successful validation of the analytic approach. The higher errors at low orders are attributed to the presence of the polar gap, ignored in the analytic method. As a matter of fact, MRO's PSO has an inclination of 92.6°, yielding a slight polar gap in the observations. As a consequence, measurements were not performed in a certain spherical cap around the poles, thus a part of the spherical harmonic coefficients shows a high variance for low orders. This is not traceable in the analytic formal errors as this approach assumes circular and polar orbits, hence no polar gap. This explains the vertical stripe with higher errors.

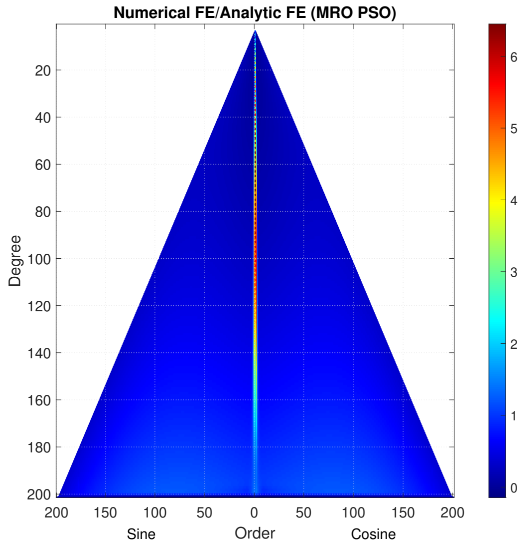

Figure A.1: Validation of the Bills and Ermakov [1]'s analytic covariance analysis approach.

A.2. Orbit design

To study orbits different from MRO's Primary Science Orbit, Tudat, whose scripts are already verified, was used to propagate new orbits, such that the orbit geometry can be related to the accuracy of the gravity solution. To this end, a single arc dynamic simulator is exploited with a Runge-Kutta-Fehlberg 7(8) integrator and a Cowell translational propagator. In this section, the analysis of the integrator errors is presented, followed by the validation of the state generator script.

A.2.1. Analysis of integrator errors

Most of the times, there are no closed-form analytical solutions that include complex dynamical models to determine the orbit of a spacecraft. Thus, it is necessary to settle for numerical integration. On Tudat, there are several integrators which differ in precision and computational effort. For this work, as mentioned before, a multi-stage variable-step-size integrator was selected: Runge Kutta Fehlberg 7(8). This is deemed a good choice as it presents reasonably high precision, albeit at the cost of relatively high integration time. Nevertheless, given the rather simple orbit geometry contemplated, i.e. mostly circular orbits for maximum 1 Martian year, the computational effort in terms of number of function evaluations and time do not constitute an issue.

Numerical integration intrinsically entails two types of error: truncation errors, related to the mathematical formulation of the integrator, and rounding errors, due to the finite floating point number representation (typically 16 digits) at each mathematical operation. When using RKF7(8) as a variable-step-size integrator, the step size control mechanism works on the principle that, firstly, the Local Truncation Error (LTE) of a single step for the 7^{th}-order method is estimated by comparing 7^{th} and 8^{th}-order integrators' results. Successively, the low-order method is exploited to adjust the subsequent time step to bring the LTE to the required level, provided that we are operating in the truncation error regime and that the truncation error model holds true. The required LTE (ε_{req}) is specified by the user by defining relative (ε_r) and absolute (ε_a) tolerances:

$$\varepsilon_{req} = \varepsilon_r y + \varepsilon_a \tag{A.2}$$

where y is the current state. By selecting low tolerances, small required errors are defined, which yield short time steps and, consequently, a high computational load. By tuning these tolerances, the behaviour of the integrator can be studied. For this work, tolerances of 10^{-10} were deemed a good compromise between numerical accuracy and computational effort. To assess whether this was a proper choice, the integration results must be compared to a "true solution". As there is not a truth model, a benchmark must be set which is considered an ideal approximation of a true solution with a high degree of confidence. This entails the selection of very strict tolerances. In this case, Runge-Kutta Dormand-Prince 8(7) integrator was selected with 10^{-14} absolute and relative tolerances. The retrieved Cartesian positions (x, y and z in body-centered reference frame) were compared to the solutions obtained with RKF7(8) for three different tolerances. To compare the results with the nominal and more accurate integration, it was necessary to interpolate the solutions to have a common set of epochs. This was performed by exploiting an 8^{th} order Lagrange interpolation and 10 s time step. The respective differences between the benchmark and the numerically integrated solutions are shown in Figure A.2.

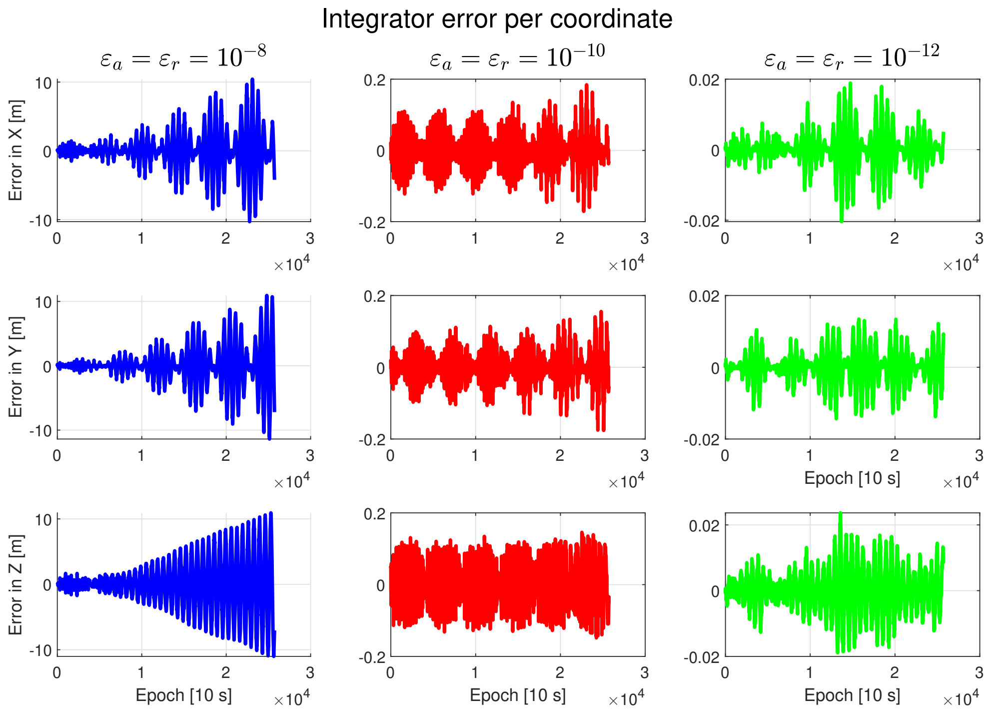

Figure A.2: Difference between benchmark solutions and RKF7(8) ones, for three values of absolute (ε_a) and relative (ε_r) tolerances.

For comparison purposes, also tolerances equal to 10^{-8} and 10^{-12} were examined. As visible in the plots above, the errors for the selected integrator settings ($\varepsilon_a = \varepsilon_r = 10^{-10}$) are between $\pm$20 cm. In Appendix B, a conclusion is drawn that positioning errors in radial, along- and cross-track directions (RSW frame) of, respectively, 1.5, 100 and 40 m do not give rise to substantial observation errors that would compromise the gravity solution. Thence, the aforementioned range, smaller than these values, is deemed low enough such that the integrator's settings choice is considered right. Lower tolerances (10^{-8}) result in higher errors, up to 10 m. In Figure A.2, the correspondent errors build up with time more evidently than in the other two cases due to the accumulation of LTE with time. On the other hand, even smaller tolerances (10^{-12}) are not recommended as the improvement in terms of position errors is minimal.

A.2.2. State generator script validation

In order to validate the code used to generate the states of other orbits, MRO's Primary Science Orbit was propagated in Tudat and compared to the real orbit downloaded from the NASA Spice-Kernels in the Planetary Data System Navigation Node of the NASA's Navigation and Ancillary Information Facility (NAIF) [1].

To propagate the PSO, its initial Keplerian elements are needed. Nevertheless, different values are encountered in literature, such as in Menon et al. [20], Johnston et al. [14] and Bowes et al. [2]. This is attributed to the fact that the spacecraft varied slightly its orbit with time. Thus, for a fair juxtaposition, as this validation entailed the comparison between the simulated orbit and the one from the Spice-Kernels, the initial state for this propagation was taken from the Spice-Kernels pool itself. The respective values are listed in Table A.1. For this simulation, the dynamical model exploited was the same described in Section 3.2.1 of the journal paper.

[1] `https://naif.jpl.nasa.gov/pub/naif/pds/data/mro-m-spice-6-v1.0/mrosp_1000/data/spk/`, accessed on 10/07/22.

Table A.1: Keplerian orbital elements from the Spice-Kernels for the 8^{th} of November 2006.

Orbital element	Symbol	Value	Unit
Semi-major axis	a	3662.61	km
Eccentricity	e	0.0089	-
Inclination	i	113.20	degree
Argument of periapsis	ω	286.01	degree
Right ascension of node	Ω	125.07	degree
True anomaly	θ	65.44	degree

The results are shown in Figure A.3 for a period of time of about 15 hours from the 8^{th} of November 2006.

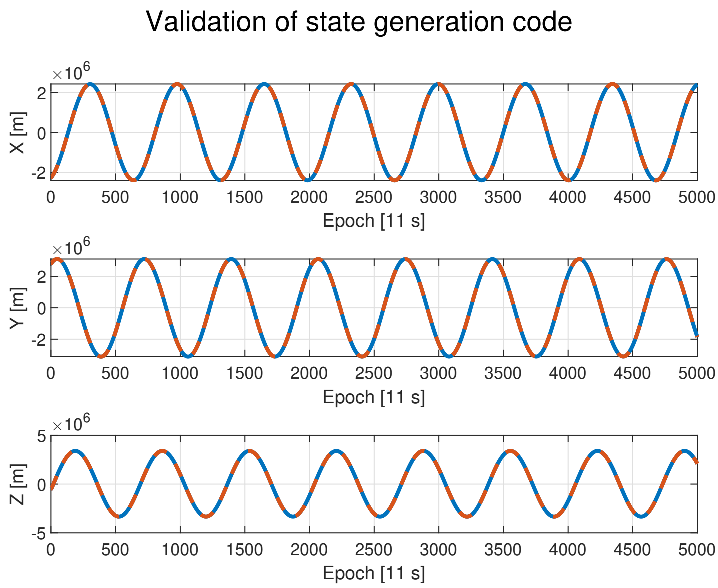

Figure A.3: Validation of state generator script. The coordinates are expressed in the global frame orientation (ECLIPJ2000[2]).

From a visual inspection, the Tudat script furnishes a good estimation of the spacecraft position. For a more punctual study, the difference between the real and the simulated orbits is shown in Figure A.4.

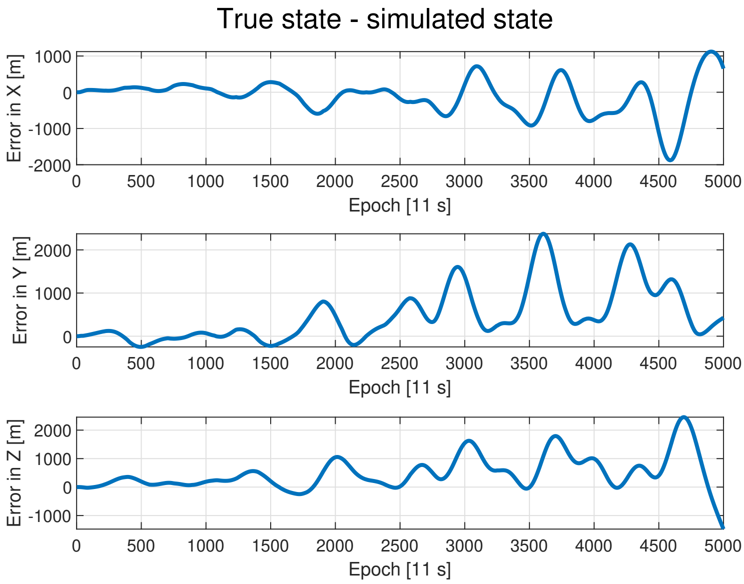

Figure A.4: Position errors between the real orbit and the simulated one.

As visible in the plots above, there is a discrepancy, which was envisaged. First of all, as analysed in subsection A.2.1, there is a certain integration error of 10s of cm. Nevertheless, the largest cause of errors stems from the exploited dynamical model which, albeit realistic, is a limited representation of the reality. For instance, the gravitational pull exerted by Phobos or the radiation pressure from the planet were neglected. But, most importantly, the atmospheric drag is considered the leading error source. To generate these states, the NASA's Mars GRAM 2010 atmospheric model[3] was exploited. The tabulated atmospheric model employed for the orbit propagation gives an average density per altitude. In reality, the density profile varies according to different factors: the time (for instance, if there is a dust storm) and the latitude and longitude (e.g., at the poles it is different from the equator). In light of these consideration, errors in the order of few kilometers are to be expected and are deemed acceptable. Hence, the validation is hereby successful.

Moreover, with these results, also the script used to load the atmospheric model is considered validated. Finally, with this, given the limited difference between the true and simulated solutions, the dynamical model from Section 3.2.1 of the journal paper is also deemed valid.

[3]requested from `https://software.nasa.gov/software/MFS-33158-1` (last accessed on 06/12/2021)

A.3. Gradiometry

To derive the spherical-harmonics formal errors, the verified code by Dr.-Ing Christian Siemes has been adapted, which was exploited for GOCE gradiometer calibration and Level 1b data processing (Siemes et al. [28],Siemes [29], Siemes [27]). The script was verified, thus only the validation of the integration of this code in Tudat was performed.

The validation strategy consisted in retrieving the RMS for the spherical harmonics of the Earth up to degree 224, and comparing it with the variance of the TIM R1 solution[4] from GOCE (Pail et al. [24]), as well as with the geoid height formal errors retrieved in Siemes [29]. The parameters that apply to this model are: Earth radius equal to 6378136.46 m and GM = 3.986004415e14 $m^3/(kg\ s^2)$ (Siemes [29]).

To this end, firstly the GOCE's reduced-dynamic orbits from the 30^{th} of October 2009 until the 11^{th} of January 2010 have been downloaded from `https://directory.eoportal.org/web/eoportal/satellite-missions`[5] (GO_CONS_SST_PRD_2 files) and subsequently loaded in the code. The states upload has been manually inspected also because the coordinates were given in kilometres, whilst the code required meters. Secondarily, a fundamental assumption must be made: GOCE's gradiometers were oriented such that the z-axis pointed towards the Earth, the x-axis into flight direction, and the y-axis completed the right-hand system. It is deemed superfluous to use the actual satellite orientation, which deviated by about 5 degrees from the aforementioned configuration. Differently from what has been done in this work, to simulate the GOCE gradiometry solutions, all of the trace elements of the gravity gradient were contemplated (U_{xx},U_{yy},U_{zz}), as well as U_{xz}. It was assumed that the gravity gradients had a white noise of 10 mE/$\sqrt{Hz}$ for U_{xx},U_{yy}, and 20 mE/$\sqrt{Hz}$ for the rest. These are realistic noise levels for frequencies larger than 3 mHz (Siemes et al. [30]). The sampling along the orbit was realistically set to 10 s.

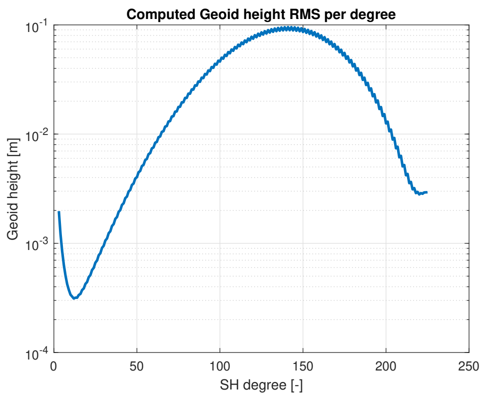

Figure A.5: Computed geoid height formal errors.

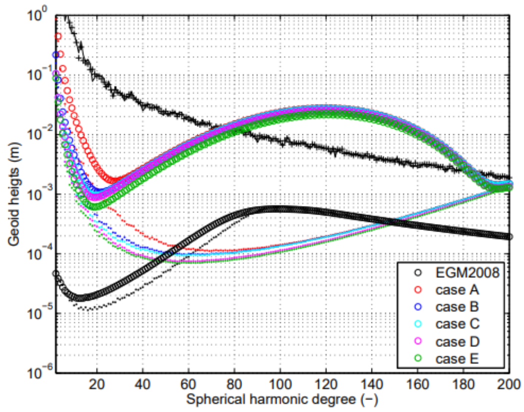

Figure A.6: Comparison of the gravity field models case A–E to the EGM2008 model (Siemes [29]). Dots and circles show the degree median and the degree standard deviation, respectively, of the formal errors in the correspondent models.

In Figure A.5, the computed formal errors for the Earth geoid height are shown and compared to the respective ones in Figure A.6, whereby the difference between the various cases depends on the processing technique (Siemes [29]) which is beyond the scope of this work. Additionally, from the charts it is visible a slight discrepancy of the two solutions at low degrees. This is attributed to the difference in noise assumption: CAI-based gradiometers display low flat noise over almost the entire frequency spectrum, whilst GOCE ones have correlated noise. Given the aforementioned assumptions, the computed solution was deemed close enough to the considered models.

Furthermore, the computed RMS of the SH coefficients was examined against the standard deviation of the model TIM R1 in Figure A.7. From the figure, the computed degree standard deviations

[4]"GO_CONS_GCF_2_TIM_R1" available in `http://icgem.gfz-potsdam.de/tom_longtime`. Last accessed on the 9^{th} of November 2022.
[5]last accessed on 15/07/2022.

are high because of the polar gap due to GOCE's sun-synchronous orbit. In van Gelderen and Koop [35], it was shown that there are some zonal and near-zonal coefficients affected by the polar gap in a sharply defined and wedge-shaped area. A rule of thumb was derived, according to which the maximum spherical harmonics order affected by polar gaps is:

$$m_{\max} \approx \left|\frac{\pi}{2} - I\right| \cdot l, \tag{A.3}$$

with I being the satellite inclination and l the SH degree.

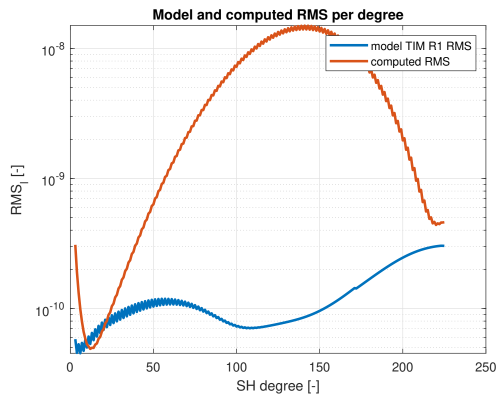

Figure A.7: TIM R1 model and computed RMS per SH degree.

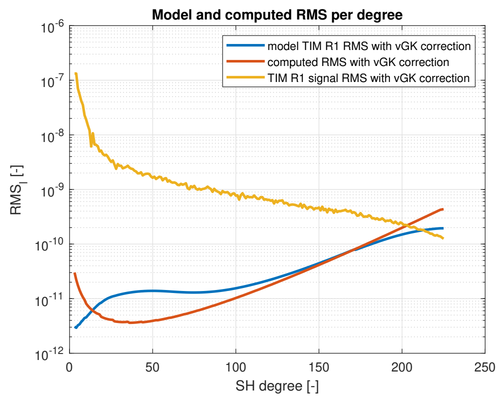

Figure A.8: TIM R1 model and computed RMS per SH degree with van Gelderen - Koop correction.

Leveraging this rule of thumb, named vGK correction, Figure A.8 was obtained. Below degree 20, the TIM R1 solution is better, as expected, because the model was attained by exploiting also GPS tracking data (high-low satellite-to-satellite tracking). On the other hand, above degree 170, the TIM solution is regularized, namely the spherical harmonic coefficients were forced towards zero. In between degrees 20 and 170, the computed solution is less than a factor of 2 away from the TIM solution, which is quite good considering that the actual satellite attitude was completely ignored. Therefore, the results led to the conclusion that the procedure was rightly validated.

B
Pointing and Positioning Errors

As concisely mentioned in section 2.3 of the journal paper, positioning and pointing errors could compromise the gravity solution. Thus, their influence is studied in this section. Reasonable pointing and positioning error values were taken from McEwen et al. [19] and Menon [21], respectively.

- The position errors were set to 1.5, 100 and 40 m in, respectively, radial (R), along track (S) and cross track (W) directions. On the other hand, the observation error was obtained by perturbing the initial position of the spacecraft by these quantities and propagating the orbit. The latter was exploited to subsequently retrieve the "perturbed" design matrix. Afterwards, the original design matrix was subtracted from the perturbed one to obtain the correspondent deviation. Finally, everything was multiplied by the spherical harmonics coefficients:

$$\varepsilon_{\text{obs}}^{\text{pos}} = (A_{\text{perturbed}} - A_{\text{nominal}}) \cdot [C_{lm}, S_{lm}]^{1}. \tag{B.1}$$

The retrieved errors are compared to the instrument sensitivity (3.5 mE for CAI 4) in Figure B.1.

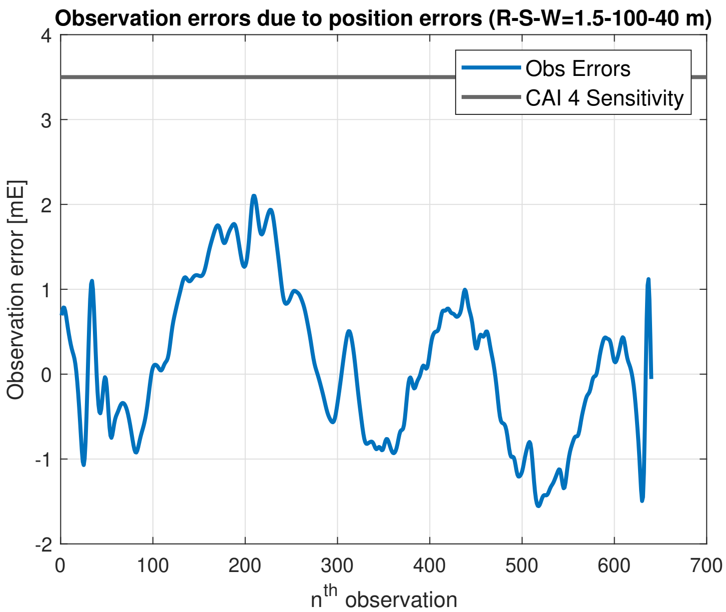

Figure B.1: Observation errors from positioning inaccuracies.

[1] Personal correspondence with Dr. ir. C. Siemes.

- On the other hand, the observation errors originated by the pointing uncertainty are obtained by introducing a perturbing rotation matrix:

$$\varepsilon_{\text{obs}}^{\text{point}} = R_{\text{noise}} U_{zz} R_{\text{noise}}^{T} - U_{zz}, \tag{B.2}$$

whereby, R_{noise} contains the angle errors in pitch, yaw and roll direction. These are assumed to be 2mrad in each direction (McEwen et al. [19]). Additionally, U_{zz} is the gravity-gradient tensor's radial component. The results are shown in Figure B.2.

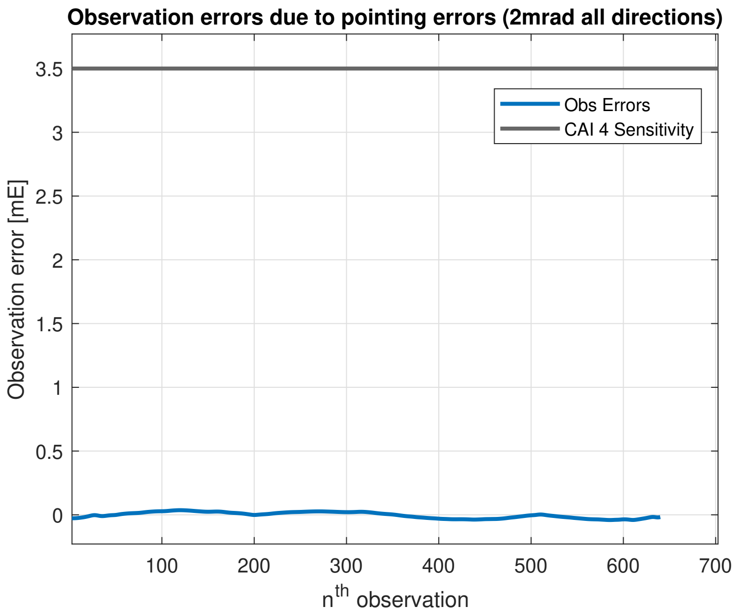

Figure B.2: Observation errors from pointing inaccuracies.

Given the nature of pointing- and positioning-induced errors, their influence is non-random. This breaks the assumption of random noise made in this work, coming along with the definition of diagonal covariance matrices (the measurement noise is considered Gaussian and uncorrelated). Therefore, a (time-varying) bias due to pointing/positioning errors would have an influence on the realism of the results. Nevertheless, as visible in both Figure B.1 and Figure B.2, pointing- and positioning-based observation errors are lower than the instrument sensitivity, even for the most sensitive sensor (CAI 4). Thus, it is safe to assume that, in the framework of this thesis, these errors are negligible as they would only slightly influence the validity of the solution.

C

Dynamical Range

Each CAI instrument has a dynamical range which limits the detectable signals, as anticipated in section 2.3 of the journal paper. In fact, the gradiometer can sense the signal only if its frequency is smaller than the inverse of the experiment time. This defines a frequency upper boundary, as shown in Figure C.1. Moreover, it is necessary to have a signal limit scale: namely, its magnitude must be such that the respective interferometer phase is smaller than 2π (inverting Equation 3 in the journal paper). This is to avoid phase jumps that lead to ambiguities. In the figure, this maximum is indicated by the horizontal red dashed line. The intersection of this and the amplitude density curve furnishes the lower bound for the instrument dynamical range.

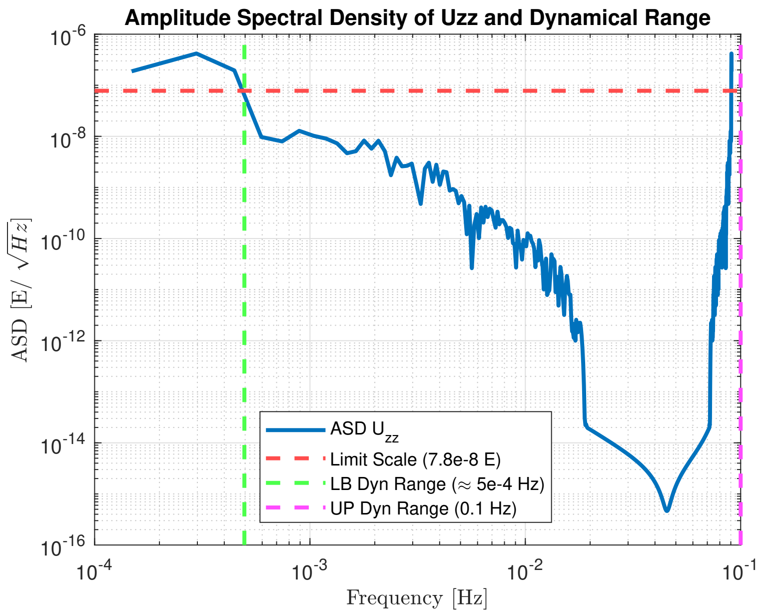

Figure C.1: Dynamical range of CAI 4 with frequency lower (LB) and upper (UP) bounds.

For signal with frequencies lower than $5{\cdot}10^{-4}$, phase ambiguities occur in the detection of the interferometer phase shift. This may be resolved by post processing: an estimated bias must be inserted to prevent phase jumps and correctly constrain the phase shift.

Bibliography

[1] Bruce G. Bills and Anton I. Ermakov. Simple models of error spectra for planetary gravitational potentials as obtained from a variety of measurement configurations. *Planetary and Space Science*, 179:104744, 2019. ISSN 0032-0633. doi: https://doi.org/10.1016/j.pss.2019.104744. URL http://www.sciencedirect.com/science/article/pii/S003206331830432X.

[2] Angela L. Bowes, C. Allen Halsell, Martin D. Johnston, Robert E. Lock, Peter Xaypraseuth, Daniel T. Lyons, Shyam Bhaskaran, and Dolan E. Highsmith. Primary science orbit design for the mars reconnaissance orbiter mission. 2003.

[3] Olivier Carraz, Christian Siemes, L. Massotti, Roger Haagmans, and Pierluigi Silvestrin. A Spaceborne Gravity Gradiometer Concept Based on Cold Atom Interferometers for Measuring Earth's Gravity Field. *Microgravity Science and Technology*, 26, 06 2014. doi: 10.1007/s12217-014-9385-x.

[4] Olivier Carraz, Christian Siemes, Luca Massotti, Roger Haagmans, and Pierluigi Silvestrin. Measuring the Earth's Gravity Field with Cold Atom Interferometers. In *5th International GOCE User Workshop*, volume 728 of *ESA Special Publication*, page 25, March 2015.

[5] B. Dubetsky and M. A. Kasevich. Atom interferometer as a selective sensor of rotation or gravity. *Physical Review A*, 74:023615, Aug 2006. doi: 10.1103/PhysRevA.74.023615. URL https://link.aps.org/doi/10.1103/PhysRevA.74.023615.

[6] Rune Floberghagen, Michael Fehringer, Daniel Lamarre, Danilo Muzi, Björn Frommknecht, Christoph Steiger, Juan Piñeiro, and Andrea da Costa. Mission design, operation and exploitation of the gravity field and steady-state ocean circulation explorer mission. *Journal of Geodesy*, 85 (11):749–758, November 2011. doi: 10.1007/s00190-011-0498-3.

[7] Herbert V. Frey, James H. Roark, Kelly M. Shockey, Erin L. Frey, and Susan E. H. Sakimoto. Ancient lowlands on Mars. *Geophysical Research Letters*, 29(10):22–1–22–4, 2002. doi: https://doi.org/10.1029/2001GL013832. URL https://agupubs.onlinelibrary.wiley.com/doi/abs/10.1029/2001GL013832.

[8] Remi Geiger, Arnaud Landragin, Sébastien Merlet, and Franck Pereira Dos Santos. High-accuracy inertial measurements with cold-atom sensors. *AVS Quantum Science*, 2(2):024702, Jun 2020. ISSN 2639-0213. doi: 10.1116/5.0009093. URL http://dx.doi.org/10.1116/5.0009093.

[9] Antonio Genova. ORACLE: A mission concept to study Mars' climate, surface and interior. *Acta Astronautica*, 166:317–329, 2020. ISSN 0094-5765. doi: https://doi.org/10.1016/j.actaastro.2019.10.006. URL https://www.sciencedirect.com/science/article/pii/S0094576519313128.

[10] Sander Goossens, Terence J. Sabaka, Antonio Genova, Erwan Mazarico, Joseph B. Nicholas, and Gregory A. Neumann. Evidence for a low bulk crustal density for Mars from gravity and topography. *Geophysical Research Letters*, 44(15):7686–7694, 2017. doi: https://doi.org/10.1002/2017GL074172. URL https://agupubs.onlinelibrary.wiley.com/doi/abs/10.1002/2017GL074172.

[11] H. Hussmann, D. Breuer, E. Hauber, J. Oberst, A Stark, and K. Wickhusen. Mars: Overview, scientific questions and concept for future orbiters, 06 2022. MAQUIS Workshop, Quantum Sensors in application to Mars.

[12] Andrea Iannone. Cold Atom Interferometry for planetary gravity field model recovery. Literature research report, TU Delft, 2020.

[13] Andrea Iannone. Cold Atom Interferometry for planetary gravity field model recovery and navigation. Internship report, ESA/ESTEC, 2021.

[14] D. Johnston, James Graf, Richard Zurek, Howard Eisen, and Benhan Jai. The Mars Reconnaissance Orbiter Mission. *Acta Astronautica*, 1:1 – 204 vol.1, 02 2003. doi: 10.1109/AERO.2003.1235052.

[15] Alex S. Konopliv, Ryan S. Park, and William M. Folkner. An improved JPL Mars gravity field and orientation from Mars orbiter and lander tracking data. *Icarus*, 274:253–260, 2016. ISSN 0019-1035. doi: https://doi.org/10.1016/j.icarus.2016.02.052. URL https://www.sciencedirect.com/science/article/pii/S0019103516001305.

[16] Alex S. Konopliv, Ryan S. Park, Attilio Rivoldini, Rose-Marie Baland, Sebastien Le Maistre, Tim Van Hoolst, Marie Yseboodt, and Veronique Dehant. Detection of the Chandler Wobble of Mars From Orbiting Spacecraft. *Geophysical Research Letters*, 47(21):e2020GL090568, 2020. doi: https://doi.org/10.1029/2020GL090568. URL https://agupubs.onlinelibrary.wiley.com/doi/abs/10.1029/2020GL090568. e2020GL090568 2020GL090568.

[17] Xiao D. Li, Frank G. Lemoine, Ho Jung Paik, Mark V. Zagarola, Peter J. Shirron, Cornelius E. Griggs, Martin Vol Moody, and Shin-Chan Han. Design of Superconducting Gravity Gradiometer Cryogenic System for Mars Mission. *International Cryocooler Conference, Boulder, CO (2016)*, 2016.

[18] Erwan Mazarico, Antonio Genova, Sander Goossens, Frank G. Lemoine, Gregory A. Neumann, Maria T. Zuber, David E. Smith, and Sean C. Solomon. The gravity field, orientation, and ephemeris of Mercury from MESSENGER observations after three years in orbit. *Journal of Geophysical Research: Planets*, 119(12):2417–2436, 2014. doi: 10.1002/2014JE004675. URL https://agupubs.onlinelibrary.wiley.com/doi/abs/10.1002/2014JE004675.

[19] Alfred S. McEwen, Eric M. Eliason, James W. Bergstrom, Nathan T. Bridges, Candice J. Hansen, W. Alan Delamere, John A. Grant, Virginia C. Gulick, Kenneth E. Herkenhoff, Laszlo Keszthelyi, Randolph L. Kirk, Michael T. Mellon, Steven W. Squyres, Nicolas Thomas, and Catherine M. Weitz. Mars Reconnaissance Orbiter's High Resolution Imaging Science Experiment (HiRISE). *Journal of Geophysical Research: Planets*, 112(E5), 2007. doi: https://doi.org/10.1029/2005JE002605. URL https://agupubs.onlinelibrary.wiley.com/doi/abs/10.1029/2005JE002605.

[20] P Menon, S Wagner, S Demcak, E Jefferson D, Graat, K Kee, and W Schulze. 50,000 Laps Around Mars: Navigating the Mars Reconnaissance Orbiter Through the Extended Missions (January 2009 – March 2017). *International Symposium on Space Flight Dynamics, Matsuyama, Japan, June 3-9. 2017*, 05 2017. URL http://hdl.handle.net/2014/47498.

[21] Sean; Demcak Stuart Menon, Premkumar; Wagner. 50,000 Laps Around Mars: Navigating the Mars Reconnaissance Orbiter Through the Extended Missions (January 2009 - March 2017). *International Symposium on Space Flight Dynamics, Matsuyama, Japan*, 2017. URL http://hdl.handle.net/2014/47498.

[22] Federica Migliaccio, Mirko Reguzzoni, Khulan Batsukh, Guglielmo Tino, Gabriele Rosi, Fiodor Sorrentino, Carla Braitenberg, Tommaso Pivetta, Dora Barbolla, and Simona Zoffoli. MOCASS: A Satellite Mission Concept Using Cold Atom Interferometry for Measuring the Earth Gravity Field. *Surveys in Geophysics*, 40:1029–1053, 08 2019. doi: 10.1007/s10712-019-09566-4.

[23] Fabian Müller, Olivier Carraz, Pieter Visser, and Olivier Witasse. Cold atom gravimetry for planetary missions. *Planetary and Space Science*, 194:105110, 2020. ISSN 0032-0633. doi: https://doi.org/10.1016/j.pss.2020.105110. URL https://www.sciencedirect.com/science/article/pii/S0032063320303238.

[24] Roland Pail, Helmut Goiginger, Reinhard Mayrhofer, Eduard Höck, Wolf-Dieter Schuh, and Jan Martin Brockmann. GOCE gravity field model derived from orbit and gradiometry data applying the time-wise method. pages 1–1, 2010. presented at the ESA Living Planet Symposium, Bergen, Norway (ESA SP-686, December 2010).

[25] G. Schubert. *Treatise on Geophysics*. Elsevier Science, 2015. ISBN 9780444538031. URL https://books.google.nl/books?id=Rg6dBAAAQBAJ.

[26] Thilo Schuldt, Christian Schubert, Markus Krutzik, Lluis Gesa Bote, Naceur Gaaloul, Jonas Hartwig, Holger Ahlers, Waldemar Herr, Katerine Posso-Trujillo, Jan Rudolph, and et al. Design of a dual species atom interferometer for space. *Experimental Astronomy*, 39(2):167–206, Mar 2015. ISSN 1572-9508. doi: 10.1007/s10686-014-9433-y. URL http://dx.doi.org/10.1007/s10686-014-9433-y.

[27] C. Siemes. *Digital Filtering Algorithms for Decorrelation Within Large Least Squares Problems*. PhD dissertation. Schriftenreihe. IGG. University of Bonn, Germany, 2012. URL https://books.google.it/books?id=XWjRngEACAAJ.

[28] C. Siemes et al. Evolution of GOCE gravity gradient performance during mission lifetime, 2014. Poster presented at the 5^{th} international GOCE user workshop for the European Space Agency, Paris, France.

[29] Christian Siemes. GOCE Level 1B Gravity Gradient Processing Algorithms . Aug 2018. URL https://earth.esa.int/eogateway/documents/20142/37627/GOCE-Level-1B-Gravity-Gradient-Processing-Algorithms.pdf. Technical report ESA-EOPSM-GOCE-TN-3397, Issue 1.0.

[30] Christian Siemes, Moritz Rexer, Anja Schlicht, and Roger Haagmans. GOCE gradiometer data calibration . *Journal of Geodesy*, 93, 06 2019. doi: 10.1007/s00190-019-01271-9. URL https://link.springer.com/content/pdf/10.1007/s00190-019-01271-9.pdf.

[31] David Smith, Maria Zuber, Herbert Frey, James Garvin, James Head, Duane Muhleman, Gordon Pettengill, Rogeer Phillips, Sean Solomon, H. Zwally, William Banerdt, and Thomas Duxbury. Mars orbiter laser altimeter: Experiment summary after the first year of global mapping of mars. *Journal of Geophysical Research*, 106:23689–23722, 10 2001. doi: 10.1029/2000JE001364.

[32] Robert Tenzer, Mehdi Eshagh, and Shuanggen Jin. Martian sub-crustal stress from gravity and topographic models. *Earth and Planetary Science Letters*, 425:84–92, 2015. ISSN 0012-821X. doi: https://doi.org/10.1016/j.epsl.2015.05.049. URL https://www.sciencedirect.com/science/article/pii/S0012821X15003477.

[33] G.M. Tino and M.A. Kasevich. *Atom Interferometry: Proceedings of the International School of Physics "Enrico Fermi", Course 188, Varenna on Lake Como, Villa Monastero, 15-20 July 2013*. International School of Physics Enrico Fermi Series. IOS Press, 2014. ISBN 9781614994473. URL https://books.google.nl/books?id=OV7IrQEACAAJ.

[34] A Trimeche, B Battelier, D Becker, A Bertoldi, P Bouyer, C Braxmaier, E Charron, R Corgier, M Cornelius, K Douch, N Gaaloul, S Herrmann, J Müller, E Rasel, C Schubert, H Wu, and F Pereira dos Santos. Concept study and preliminary design of a cold atom interferometer for space gravity gradiometry. *Classical and Quantum Gravity*, 36(21):215004, oct 2019. doi: 10.1088/1361-6382/ab4548. URL https://dx.doi.org/10.1088/1361-6382/ab4548.

[35] M. van Gelderen and Radboud Koop. The use of degree variances in satellite gradiometry. *Journal of Geodesy*, 71:337–343, 05 1997. doi: 10.1007/s001900050101.

[36] M.A. Wieczorek. *Gravity and Topography of the Terrestrial Planets*, pages 153–193. 01 2015. doi: 10.1016/B978-0-444-53802-4.00169-X.

[37] Weiyong Yi, R. Rummel, and Thomas Gruber. Gravity field contribution analysis of GOCE gravitational gradient components. *Studia Geophysica et Geodaetica*, 57, 03 2013. doi: 10.1007/s11200-011-1178-8.

[38] Nan Yu, James Kohel, J. Kellogg, and L. Maleki. Development of an atom-interferometer gravity gradiometer for gravity measurement from space. *Applied Physics B*, 84:647–652, 09 2006. doi: 10.1007/s00340-006-2376-x.

[39] Nan Nan Yu, James M. Kohel, L. J. Romans, and Lute Maleki. Quantum gravity gradiometer sensor for Earth science applications. 2002. Jet Propulsion Laboratory, California Institute of Technology.

[40] Wei Zheng, Houtse Hsu, Min Zhong, and Meijuan Yun. Future dedicated Venus-SGG flight mission: Accuracy assessment and performance analysis. *Advances in Space Research*, 57(1): 459–476, 2016. ISSN 0273-1177. doi: https://doi.org/10.1016/j.asr.2015.08.036. URL https://www.sciencedirect.com/science/article/pii/S0273117715006201.

[41] Richard W. Zurek and Suzanne E. Smrekar. An overview of the Mars Reconnaissance Orbiter (MRO) science mission. *Journal of Geophysical Research: Planets*, 112(E5), 2007. doi: https://doi.org/10.1029/2006JE002701. URL https://agupubs.onlinelibrary.wiley.com/doi/abs/10.1029/2006JE002701.